PERIDYNAMIC MODELLING OF INTERNAL FEATURES AND INTERFACES FOR MATERIAL TOUGHENING

by
MOHAMMAD NAQIB RAHIMI

Submitted to the Graduate School of Engineering and Natural Science
in partial fulfillment of
the requirements for the degree of
Master of Science

Sabanci University
December 2020

PERIDYNAMIC MODELLING OF INTERNAL FEATURES AND INTERFACES FOR MATERIAL TOUGHENING

Approved by

APPROVAL DATE: 25.Dec.2020

PERIDYNAMIC MODELLING OF INTERNAL FEATURES AND INTERFACES FOR MATERIAL TOUGHENING

Mohammad Naqib Rahimi

M.Sc. Thesis, Dec 2020

Supervisor: Asst. Prof. Dr. Adnan Kefal

Keywords: *Peridynamics, Functionally Graded Materials, Interface Modeling, Toughening Mechanisms*

Abstract

Metals and ceramics are the two widely used materials in naval, aerospace, and structural engineering due to their high stiffness/weight ratio and design flexibility. However, their vulnerability to the occurrence of micro/macro cracks limits their potential and usage for the critical engineering applications. One way to improve the capabilities of metals and ceramics against crack occurrences is the implantation of the local weak zones into the material. Nevertheless, numerical analysis of such domains become quite challenging due to the simultaneous interactions of multiple interfaces, discontinuities, and phase changes. This study aims to systematically analyze the effects of different local weak zones on the behavior of the crack and the global toughness of homogeneous and graded materials. The realms of this thesis are assessed in two articles with an improved peridynamic formulation for precise modeling of interfaces.

In the first paper, traditional peridynamic formulation is used to simulate the effects of the shape and locations of stop-holes on crack dynamics in homogeneous materials. Various combinations of stop-holes are analyzed under tensile and shear loadings while comparing their toughening effects. In the second paper, an improved formulation of peridynamic is proposed for graded composites by considering the interface and multi-scale effects, through introducing the *dominancy rate* parameter.

Overall, this study provides a unique contribution to the existing state of the art in terms of proposing a novel peridynamic methodology which can handle modelling of sharp transitions in material properties as well as suggesting numerically validated new toughening configurations for different materials.

Özet

Metaller ve seramikler, yüksek sertlik/ağırlık oranı ve tasarım esnekliği nedeniyle denizcilik, havacılık ve yapı mühendisliğinde yaygın olarak kullanılan iki malzeme çeşididir. Bununla birlikte, mikro/makro çatlakların oluşumuna karşı dirençsizlikleri, potansiyellerini ve kritik mühendislik uygulamaları için kullanımlarını sınırlar. Metallerin ve seramiğin çatlak oluşumuna karşı özelliklerinin geliştirmesinin bir yolu ise malzemeye yerel zayıf bölgelerinin yerleştirilmesidir. Buna ek olarak, bu tür komplike ortamların sayısal analizi, çoklu arayüzlerin, süreksizliklerin ve faz değişikliklerinin eşzamanlı etkileşimleri nedeniyle oldukça zor hale gelir. Bu nedenle, bu çalışma, farklı yerel zayıf bölgelerin çatlak davranışı ve malzemenin genel dayanıklılığı üzerindeki etkilerini sistematik olarak analiz etmeyi amaçlamaktadır. Bu çalışmanın içeriği, arayüzlerin hassas modellenmesi için geliştirilmiş bir peridinamik formülasyonu ile iki makalede değerlendirilmiştir.

İlk makalede, homojen malzemelerde durdurma deliklerinin çatlak dinamiği üzerindeki etkileri, geleneksel peridinamik kullanılarak analiz edilmiştir. Çeşitli durdurma deliği kombinasyonları, sertleştirme etkileri karşılaştırılarak çekme ve kesme yükleri altında analiz edilmiştir. İkinci makalede ise, baskınlık oranı parametresi tanıtılarak, çoklu malzemeli ortamlarda, yani fonksiyonel olarak kademelendirilmiş malzemelerdeki arayüz ve çoklu ölçekli etkiler dikkate alınarak geliştirilmiş bir peridinamik formülasyonu önerilmiştir.

Genel olarak, bu çalışma, malzeme özelliklerindeki keskin geçişlerin modellenmesinin yanı sıra farklı malzemeler için sayısal olarak doğrulanmış yeni sertleştirme mekanizmalarını öneren yeni bir peridinamik metodolojisini sunmak açısından mevcut literatür durumuna benzersiz bir katkı sağlamaktadır.

To anonymous people of Afghanistan and Turkey who funded my undergrad and master's scholarships with their taxes

Acknowledgment

I would like to express my deepest gratitude and thanks to my supervisor Asst. Prof. Dr. Adnan Kefal for his genuine encouragement and continues support throughout this research which gave me the opportunity to explore various fields of computational mechanics.

I would also like to forward my very sincerely thanks to Prof. Mehmet Yildiz for his excellence guidance and advises which immensely helped me in developing my research and computational skills.

Very special thanks go to Prof. Erkan Oterkus for his time and valuable guidance on the field of Peridynamics.

I would also like to thank my friend and colleague Aryan Kheyabani for his helpful support and scientific discussions.

I am grateful to my family whose encouragement and sacrifices gave me the opportunity to reach this stage of my life.

Many thanks to Sabanci University and SU-IMC family for the support and equipment needed to conduct this thesis in the past two years.

Finally, and most importantly, huge thank to Hilal for her patience and priceless companionship which motivated me throughout my studies.

The financial support provided by the Scientific and Technological Research Council of Turkey (TUBITAK) under the grant No: 217M207 is greatly acknowledged.

Contents

List of Figures

List of Tables

List of Algorithms

List of Symbols

The following list describes several symbols that will be used throughout this thesis:

$\bar{G}$	Critical energy release rate
$\ddot{\mathbf{u}}$	Acceleration
Δl	Change in the lenght of the bond
Δx	Material point distancing
δ	Peridynamic horizon
$\digamma$	Material gradient in FGMs
$\hat{\mathbf{e}}$	Unit vector in the direction of displaced bond
κ	Bulk's modulus
$\mathscr{H}_{\mathbf{x}}$	Set of points having equal elastic properties with point $\mathbf{x}$
$\mathscr{M}_{\mathbf{x}}$	Set of points having lower elastic properties than point $\mathbf{x}$
$\mathscr{N}_{\mathbf{x}}$	Family of material point $\mathbf{x}$
$\mathscr{X}_{\mathbf{x}}$	Set of points having higher elastic properties than point $\mathbf{x}$
μ	Shear modulus
ψ	*Dominancy rate* parameter
ρ	Density
σ	External stress
$\mathbf{b}_{(i)}$	Body force of point i
$\mathbf{t}$	Force density vector acting from point $\mathbf{x}$ on point $\mathbf{x}'$
$\mathbf{t}'$	Force density vector acting from point $\mathbf{x}'$ on point $\mathbf{x}$
$\mathbf{u}$	Displacement
$\mathbf{y}$	Displaced position of points
$\mathrm{v}(x)$	Displacement of point $\mathbf{x}$ in vertical direction
$\theta_{\mathbf{x}}$	Dilatation of point $\mathbf{x}$
$\theta_{\mathbf{x}'}$	Dilatation of point $\mathbf{x}'$
$\varphi_{(i)}$	Total damage of point i
a_{μ}	Amount of acceleration of the crack caused by a hole (μ-acceleration)

dt^c Optimum time-step size for dynamic solution of PD

E Elastic modulus

E_r Order of magnitude of the change in elastic modulus between FGM plate and sub-regions

E_{min} Minimum elastic modulus value in FGM plates

h Thickness

KIc Fracture toughness

L Lenght of plates

$N_{\mathbf{x}}^{\mathscr{H}}$ Number of neighbours of point $\mathbf{x}$ in domain $\mathscr{H}$

$N_{\mathbf{x}}^{\mathscr{M}}$ Number of neighbours of point $\mathbf{x}$ in domain $\mathscr{M}$

$N_{\mathbf{x}}^{\mathscr{X}}$ Number of neighbours of point $\mathbf{x}$ in domain $\mathscr{X}$

P_{eff} Effective material property in FGM

P_{phase1} Property of phase 1

S Bond stretch

S^c Critical stretch

t_μ Time of μ-acceleration

$u(x)$ Displacement of point $\mathbf{x}$ in horizontal direction

U_{ANS} Displacement solved by ANSYS

U_{ANS}^{max} Maximum displacement solved by ANSYS

U_{PD} Displacement solved by Peridynamic

V Incremental volume

v Poisson's ratio

V' Corrected incremental volume

W Width of plates

$W(\mathbf{x})$ Total strain energy density of point $\mathbf{x}$

$W_{\mathscr{H}_{\mathbf{x}}}(\mathbf{x})$ Strain energy density of point $\mathbf{x}$ contributed by set $\mathscr{H}_{\mathbf{x}}$ of $\mathscr{N}_{\mathbf{x}}$

$W_{\mathscr{M}_{\mathbf{x}}}(\mathbf{x})$ Strain energy density of point $\mathbf{x}$ contributed by set $\mathscr{M}_{\mathbf{x}}$ of $\mathscr{N}_{\mathbf{x}}$

$W_{\mathscr{X}_{\mathbf{x}}}(\mathbf{x})$ Strain energy density of point $\mathbf{x}$ contributed by set $\mathscr{X}_{\mathbf{x}}$ of $\mathscr{N}_{\mathbf{x}}$

X_c Position of crack-tip in prisitne (normal) plates

Part I

1 Introduction

As the demands for light-weight material has increased in various engineering fields, toughness enhancement has become quite critical in a wide range of materials that are either operating at room temperature or elevated thermal conditions. An engineering component is expected to have enough endurance against any kind of load during its operational life. Nonetheless, depending on the environmental/operational conditions of an engineering structure, load-bearing components of the structure may experience extreme loading circumstances, which can lead to the development of the so-called micro-cracks. The coalescence and growth of these micro-cracks form various macro-cracks, eventually causing the complete failure. A major concern for such kind of failure is their high growth speed, which bears a potential risk to human safety and may cause crucial financial losses [1–3]. Toughening models, such as micro-crack toughening [4–7], internal void features [8–10], and different material phases[11], are the cheapest and effective ways to reduce the risk of failure and increase the material toughness against crack propagations [12–14]. However, most of the numerical works on these methodologies are carried out using the conventional approaches, i.e., models based on classical continuum mechanics (CCM).

CCM formulations are constructed with the assumption of continuity, which concludes that the body remains continuous as it deforms. Despite its long success in terms of modeling certain physical phenomena, there well-known drawbacks of CCM exist in the problems involving damage occurrence(s), discontinuities, internal features and multi-scale effects. The formulations in CCM are governed by the derivatives of displacement, which remain unknown at the crack-tip and discontinuity regions, thereby resulting in crack-tip singularity problems [15]. Even though there are many suggested solutions to the particular problems of this nature [16–18], they still suffer from dependency to external variables and/or extra partial differential equations which cannot mitigate the requirement of additional treatments. In complex problems, such as toughening mechanisms with internal features and different phases, the dependency of the governing equation on external variables may be problematic and might generate non-physical results. Besides, a predefined crack is needed in CCM to model the damage propagations, which may not always be the case. These shortcomings of CCM can be readily addressed by utilizing the Peridynamic (PD), i.e., a robust non-local approach [19]. The equation of motion in PD is in the integral forms of displacements, thereby enabling PD to be applicable to the discontinuity regions with no further treatments. Due to its advantageous capabilities in modeling fracture and damage propagations, the PD theory has gained notable interest and dedication of researchers in a short period of time and was rapidly developed to model different kinds of problems, including; application of PD to various homogenous

and non-homogenous materials [20–25], Multiphysics [26, 27], optimizations [28–30], micro-crack toughening models [31] and so on [32, 33]. Despite its extensive usage in many disciplines and various problems, there no study exists regarding the application of PD in toughening mechanisms using internal features, such as holes and different material phases. In addition, no research has been found on the numerical toughening mechanisms of multi-material media, i.e., functionally graded materials (FGMs).

Numerical modelling of multi-material media and toughening mechanisms of functionally graded materials are quite challenging due to the presence of non-homogeneous property variation and multiple interfaces. Only recently, Chen et al. [34] proposed a bond-based peridynamic (BB-PD) model for FGMs to simulate dynamic crack propagations. The proposed model takes into account the properties of the bonds (elastic relations) between material points regardless of their decoupled distortional deformation states [19], thereby restricting its application to materials with Poisson's ratio of 1/3 only. This issue was later circumvented with the development of the Ordinary State-Based Peridynamic (OSB-PD) formulations for FGMs by Ozdemir et al. [35]. Perhaps one of the main issues of the above two models is the assumption by which the properties of the PD-bonds are driven. In both models it is assumed that the properties of a bond are equally affected by the properties of the constituent material points, which may not physically be accurate. Such an assumption also contradicts the multi-scale nature of PD: as the scale of the problem changes, expectedly the ratio of energy induced by the points on the bonds should change as well. Furthermore, in the traditional PD formulation for FGMs [34, 35], the properties of a bond is calculated by taking the arithmetic average of the properties of the constituent points. However, if a material point is set to represent near-void properties (with extremely low elastic modulus), the traditional approach would not warrant a zero strain-energy between the void and normal points. Although the existing models can capture certain behaviors of low gradient FGMs with an acceptable accuracy, they fail to handle internal void features, sharp transitions of the material properties or higher gradient FGMs. As the numerical toughening models in this study contain sharp material transitions, phase changes, and interfaces, we shall firstly develop a model which can simulate these effects accurately.

Therefore, in this thesis, the above gaps in the literature of toughening mechanisms and peridynamics for homogeneous and functionally graded materials are addressed as follows:

(i) In the first paper, the traditional OSB-PD formulation is used to introduce a numerical toughening mechanism for brittle homogenous materials under in-plane shear and tensile stresses. The mechanism is enriched with the linear and non-linear combinations of internal features, i.e., stop-holes. The proposed methodology is shown

to be highly effective in decreasing the cost and increasing the overall toughness, given that the presence of a perforation (i.e., stop-hole) can reduce the weight of the structure and material costs.

(ii) In the second paper, an improved OSB-PD formulation is proposed by considering the multi-scale effects, high material gradients, interfaces and the sudden changes in material properties. A *dominancy rate* parameter is introduced into PD literature to accurately model the aforementioned effects in FGMs. Moreover, as an application of the present formulation, a novel numerical toughening model is presented to enhance the properties of FGMs against crack propagations.

The related publications of this study are provided in Chapter 3 and 4 along with the shortened relevant literature reviews and conclusions. Moreover, the generalized form of the improved peridynamic formulation, used in Chapter 4, is given in the proceeding chapter with the necessary links to Chapter 3.

2 Peridynamic Formulations for Multi-material media

Peridynamics (PD) is a mesh-free approach originally introduced by Silling in 2000 [19]. The PD approach is referred to as the non-local form of classical continuum mechanics (CCM) or the shrunken form of molecular dynamics, which uses integro-differential equations rather than the classical spatial derivatives of stress components, thereby, making it ideal for fracture mechanics problems. A continuum in PD is modelled as a set of infinitesimal volumes (material points) interacting with each other in a non-local form. The range of the interactions is named as horizon, δ, and the interactions are called the PD bonds. Horizon is generally taken as $\delta = 3\Delta x$, in which Δx is the material point distancing. All the points located within horizon of a point, e. g., point $\mathbf{x}$, constitute its family, $\mathscr{N}_{\mathbf{x}}$. For a three-dimensional continuum, $\mathscr{N}_{\mathbf{x}}$ is a spherical domain of material points with a radius of δ, while it reduces to a circular set in a two-dimensional case which can be written as:

$$\mathscr{N}_{\mathbf{x}} = \mathscr{H}_{\mathbf{x}} + \mathscr{X}_{\mathbf{x}} + \mathscr{M}_{\mathbf{x}} \tag{2.1}$$

for a multi-material continuum, i.e., functionally graded materials (FGM). Here, $\mathscr{H}_{\mathbf{x}}$, $\mathscr{M}_{\mathbf{x}}$, and $\mathscr{X}_{\mathbf{x}}$ are, in turn, the domain of the points possessing equal, lower, and higher properties than that of point $\mathbf{x}$ in terms of elasticity, as depicted in Fig.2.1. All the bonds in PD apply pair-wise forces on their dual material points when subjected to a displacement gradient. In bond-based peridynamics (BB-PD) these pairwise forces are assumed to have opposite directions and equal magnitudes while in ordinary-state-based peridynamics (OSB-PD) their magnitudes are taken to be different. This of course enables OSB-PD to be applicable to more general cases such as problems undergoing volumetric and decoupled distortional deformations. The governing equation of motion for FGMs in OSB-PD can be written in the integral form of displacements as follows:

$$\rho(\mathbf{x})\ddot{\mathbf{u}}(\mathbf{x},t) = \int_{\mathscr{N}_{\mathbf{x}}} \left[\mathbf{t}_{\mathscr{P}}(\mathbf{u}'_{\mathscr{N}} - \mathbf{u}, \mathbf{x}'_{\mathscr{N}} - \mathbf{x}, t) - \mathbf{t}'_{\mathscr{P}}(\mathbf{u} - \mathbf{u}'_{\mathscr{N}}, \mathbf{x} - \mathbf{x}'_{\mathscr{N}}, t)\right] d\mathscr{N}_{\mathbf{x}} + \mathbf{b}(\mathbf{x},t) \tag{2.2}$$

in which, $\rho(\mathbf{x})$ is the density of the point initially located at $\mathbf{x}$ with the vectors $\mathbf{u}$, $\ddot{\mathbf{u}}(\mathbf{x},t)$, and $\mathbf{b}(\mathbf{x},t)$ being its displacement, acceleration, and external body force at the instant of time, t. The terms $\mathbf{t} \equiv \mathbf{t}(\mathbf{u}' - \mathbf{u}, \mathbf{x}' - \mathbf{x}, t)$ and $\mathbf{t}' \equiv \mathbf{t}'(\mathbf{u} - \mathbf{u}', \mathbf{x} - \mathbf{x}', t)$ are called the pairwise force density vectors acting from material point $\mathbf{x}'$ on material point $\mathbf{x}$ and from material point $\mathbf{x}$ on material point $\mathbf{x}'$, respectively. The index $\mathscr{P} \ni \{\mathscr{X}, \mathscr{H}, \mathscr{M}\}$ shows the category of the interacting pairwise forces. As the behavior of a bond between two material points in PD is similar to the ones of elastic springs, the following relations would

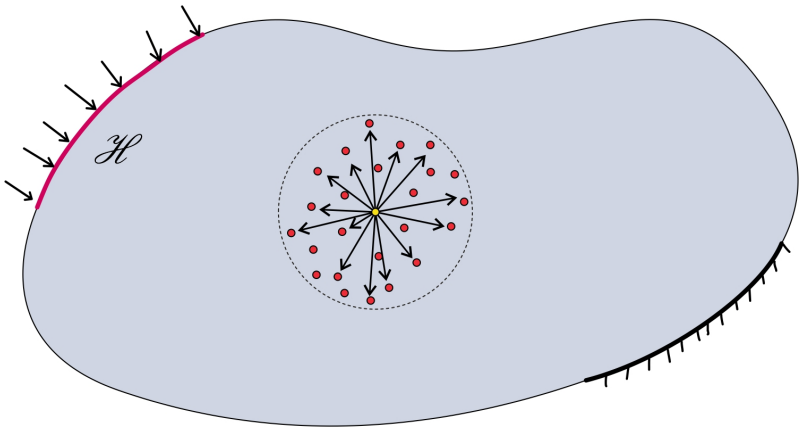

(a) Homogeneous materials

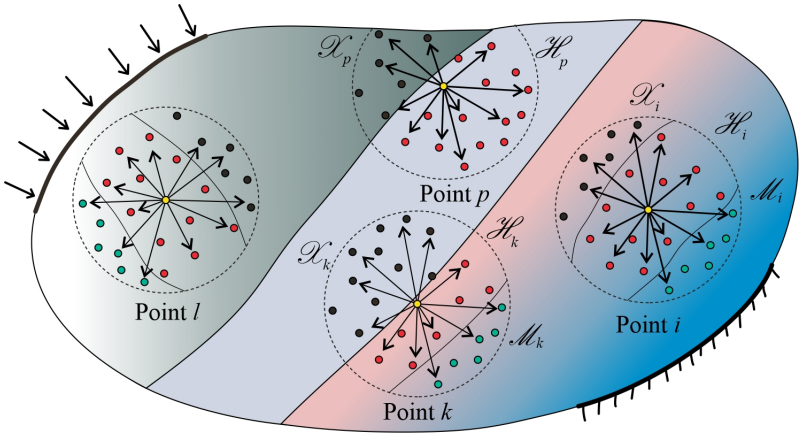

(b) Non-homogeneous materials (FGMs)

Figure 2.1: Undeformed state of PD continuum

be safe to write:

$$\begin{matrix}\mathbf{t}_{\mathscr{H}}-\mathbf{t}'_{\mathscr{H}}\\ \mathbf{t}_{\mathscr{X}}-\mathbf{t}'_{\mathscr{X}}\\ \mathbf{t}_{\mathscr{M}}-\mathbf{t}'_{\mathscr{M}}\end{matrix}=\begin{Bmatrix}\left[\dfrac{\partial W(\mathbf{x})}{\partial\left(\left|\mathbf{y}'_{\mathscr{H}}-\mathbf{y}\right|\right)}-\dfrac{\partial W(\mathbf{x}'_{\mathscr{H}})}{\partial\left(|\mathbf{y}-\mathbf{y}'_{\mathscr{H}}|\right)}\right]\hat{\mathbf{e}}\\ \left[\dfrac{\partial W(\mathbf{x})}{\partial\left(\left|\mathbf{y}'_{\mathscr{X}}-\mathbf{y}\right|\right)}-\dfrac{\partial W(\mathbf{x}'_{\mathscr{X}})}{\partial\left(|\mathbf{y}-\mathbf{y}'_{\mathscr{X}}|\right)}\right]\hat{\mathbf{e}}\\ \left[\dfrac{\partial W(\mathbf{x})}{\partial\left(\left|\mathbf{y}'_{\mathscr{M}}-\mathbf{y}\right|\right)}-\dfrac{\partial W(\mathbf{x}'_{\mathscr{M}})}{\partial\left(|\mathbf{y}-\mathbf{y}'_{\mathscr{M}}|\right)}\right]\hat{\mathbf{e}}\end{Bmatrix}=\begin{Bmatrix}\beta^{\mathscr{H}}\hat{\mathbf{e}}\\ \beta^{\mathscr{X}}\hat{\mathbf{e}}\\ \beta^{\mathscr{M}}\hat{\mathbf{e}}\end{Bmatrix} \tag{2.3}$$

where $\hat{\mathbf{e}}=(\mathbf{y}'-\mathbf{y})/|\mathbf{y}'-\mathbf{y}|$ is the unit vector aligned with the direction of the deformed bond between material points $\mathbf{x}$ and $\mathbf{x}'$, as depicted in Fig.2.2. The parameter $W(\mathbf{x})$ is called the strain energy density arisen from the summation of micro-potentials caused by the incremental change in the length of the bonds in $\mathscr{N}_{\mathbf{x}}$. For a homogeneous isotropic material, where $\mathscr{N}_{\mathbf{x}}=\mathscr{H}_{\mathbf{x}}$, the equation for strain energy density is given in Ref.[36]. However, to account for the complexity of FGMs in terms of their gradient and interface

effects, the strain energy density for any point $\mathbf{x}$ should be modified as follows:

$$W(\mathbf{x}) = W_{\mathscr{H}_\mathbf{x}}(\mathbf{x}) + W_{\mathscr{X}_\mathbf{x}}(\mathbf{x}) + W_{\mathscr{M}_\mathbf{x}}(\mathbf{x}) \tag{2.4}$$

where

$$W_{\mathscr{H}_\mathbf{x}}(\mathbf{x}) = \gamma^2_{\mathscr{H}_\mathbf{x}} + \frac{6\mu_\mathbf{x}}{\pi h \delta^3} \iint\limits_{\mathscr{H}_\mathbf{x}} \frac{(\Delta l)^2}{|\Delta \mathbf{x}|} d\mathscr{H}_\mathbf{x} \tag{2.5a}$$

$$W_{\mathscr{X}_\mathbf{x}}(\mathbf{x}) = \gamma^2_{\mathscr{X}_\mathbf{x}} + \frac{6}{\pi h \delta^3 (\psi+1)} \iint\limits_{\mathscr{X}_\mathbf{x}} (\psi\mu_\mathbf{x} + \mu_{\mathbf{x}'}) \frac{(\Delta l)^2}{|\Delta \mathbf{x}|} d\mathscr{X}_\mathbf{x} \tag{2.5b}$$

$$W_{\mathscr{M}_\mathbf{x}}(\mathbf{x}) = \gamma^2_{\mathscr{M}_\mathbf{x}} + \frac{6}{\pi h \delta^3 (\psi+1)} \iint\limits_{\mathscr{M}_\mathbf{x}} (\mu_\mathbf{x} + \psi\mu_{\mathbf{x}'}) \frac{(\Delta l)^2}{|\Delta \mathbf{x}|} d\mathscr{M}_\mathbf{x} \tag{2.5c}$$

Here, the γ terms are the amount of energy attributed by dilatation of the points and are calculated as:

$$\gamma_{\mathscr{H}_\mathbf{x}} = \frac{\sqrt{2\phi_\mathbf{x}}}{\pi h \delta^2} \iint\limits_{\mathscr{H}_\mathbf{x}} \frac{\Delta l}{|\Delta \mathbf{x}|} \Lambda \, d\mathscr{H}_\mathbf{x} \tag{2.6a}$$

$$\gamma_{\mathscr{X}_\mathbf{x}} = \frac{\sqrt{2}}{\pi h \delta^2 \sqrt{\psi+1}} \iint\limits_{\mathscr{X}_\mathbf{x}} \sqrt{\psi\phi_\mathbf{x} + \phi_{\mathbf{x}'}} \frac{\Delta l}{|\Delta \mathbf{x}|} \Lambda \, d\mathscr{X}_\mathbf{x} \tag{2.6b}$$

$$\gamma_{\mathscr{M}_\mathbf{x}} = \frac{\sqrt{2}}{\pi h \delta^2 \sqrt{\psi+1}} \iint\limits_{\mathscr{M}_\mathbf{x}} \sqrt{\phi_\mathbf{x} + \psi\phi_{\mathbf{x}'}} \frac{\Delta l}{|\Delta \mathbf{x}|} \Lambda \, d\mathscr{M}_\mathbf{x} \tag{2.6c}$$

Herein, the parameters h and $\Delta l = (|\Delta \mathbf{y}| - |\Delta \mathbf{x}|)$ represent the thickness and the change in the length of the bond with $\Delta \mathbf{y} = (\mathbf{y}' - \mathbf{y})$ and $\Delta \mathbf{x} = (\mathbf{x}' - \mathbf{x})$ being the relative final and initial positions of the constituent points, respectively. ψ, named as the *dominancy rate*,

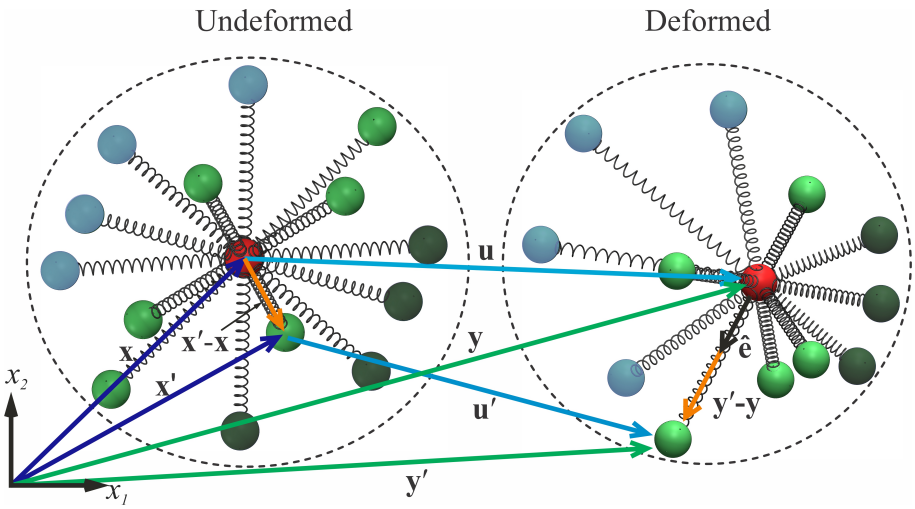

Figure 2.2: Deformation state of PD continuum

is the newly introduce parameter which plays an important role in realistic modeling of FGMs that encounter any possible high/low material gradients or any jump in the structure including; interfaces, defects, degraded material regions, and void contents. The effects of the dominancy rate on such cases will extensively be investigated for various gradients and defects in Chapter 4 of this study. Accordingly, other parameters can be defined as:

$$\Lambda = \frac{\Delta \mathbf{y}}{|\Delta \mathbf{y}|} \cdot \frac{\Delta \mathbf{x}}{|\Delta \mathbf{x}|} \tag{2.7}$$

$$\phi = \kappa - 2\mu \tag{2.8}$$

where κ and μ are the bulk and shear modulus of the related points, respectively. It should be noted that the strain energy density terms of each domain in Eq.(2.5) is a function of the related domain only, thereby, resulting in a zero partial derivative with respect to other domains. Hence:

$$\frac{\partial W(\mathbf{x})}{\partial \left(|\mathbf{y}'_{\mathscr{H}} - \mathbf{y}|\right)} = \frac{\partial W_{\mathscr{H}_\mathbf{x}}(\mathbf{x})}{\partial \left(|\mathbf{y}'_{\mathscr{H}} - \mathbf{y}|\right)} + 0 + 0 \tag{2.9a}$$

$$\frac{\partial W(\mathbf{x})}{\partial \left(|\mathbf{y}'_{\mathscr{X}} - \mathbf{y}|\right)} = 0 + \frac{\partial W_{\mathscr{X}_\mathbf{x}}(\mathbf{x})}{\partial \left(|\mathbf{y}'_{\mathscr{X}} - \mathbf{y}|\right)} + 0 \tag{2.9b}$$

$$\frac{\partial W(\mathbf{x})}{\partial \left(|\mathbf{y}'_{\mathscr{M}} - \mathbf{y}|\right)} = 0 + 0 + \frac{\partial W_{\mathscr{M}_\mathbf{x}}(\mathbf{x})}{\partial \left(|\mathbf{y}'_{\mathscr{M}} - \mathbf{y}|\right)} \tag{2.9c}$$

After substituting for $W(\mathbf{x})$ and $W(\mathbf{x}')$ in Eq.(2.3) from Eqs.(2.4-2.9) and taking the associated partial derivatives, the scalar terms $\beta^{\mathscr{H}}$, $\beta^{\mathscr{X}}$, and $\beta^{\mathscr{M}}$ in Eq.(2.3) can explicitly be defined as:

$$\beta^{\mathscr{H}} = 2\alpha \left(\delta S \mu_\mathbf{x} + \Theta \phi_\mathbf{x}\right) \tag{2.10a}$$

$$\beta^{\mathscr{X}} = \frac{2\alpha}{\psi + 1} \left[(\delta S - \Theta)(\psi \mu_\mathbf{x} + \mu_{\mathbf{x}'}) + \frac{1}{2}\Theta(\psi \kappa_\mathbf{x} + \kappa_{\mathbf{x}'}) \right] \tag{2.10b}$$

$$\beta^{\mathscr{M}} = \frac{2\alpha}{\psi + 1} \left[(\delta S - \Theta)(\mu_\mathbf{x} + \psi \mu_{\mathbf{x}'}) + \frac{1}{2}\Theta(\kappa_\mathbf{x} + \psi \kappa_{\mathbf{x}'}) \right] \tag{2.10c}$$

where S is the stretch of the bond between $\mathbf{x}$ and $\mathbf{x}'$ which is calculated as:

$$S = \frac{\Delta l}{|\Delta \mathbf{x}|} \tag{2.11}$$

The other parameters in Eq.(2.10) are defined as:

$$\alpha = \frac{12}{\pi h \delta^4} \tag{2.12}$$

$$\Theta = \frac{\delta^2}{12|\Delta\mathbf{x}|}\Lambda(\theta_{\mathbf{x}} + \theta_{\mathbf{x}'}) \tag{2.13}$$

in which, $\theta_{\mathbf{x}}$ and $\theta_{\mathbf{x}'}$ are the dilatation of the points $\mathbf{x}$ and $\mathbf{x}'$, respectively, and are calculated as follows:

$$\theta_{\mathbf{x}} = \frac{2}{\pi h \delta^2} \iint\limits_{\mathscr{N}_{\mathbf{x}}} \frac{\Delta l}{|\Delta\mathbf{x}|}\Lambda \, d\mathscr{N}_{\mathbf{x}} \tag{2.14a}$$

$$\theta_{\mathbf{x}'} = \frac{2}{\pi h \delta^2} \iint\limits_{\mathscr{N}_{\mathbf{x}'}} \frac{\Delta l}{|\Delta\mathbf{x}|}\Lambda \, d\mathscr{N}_{\mathbf{x}'} \tag{2.14b}$$

It is worth mentioning that by setting the value of ψ to 1 in Eqs.(2.5-2.10), one can easily achieve the FGM models suggested in Refs.[34, 35]. It should also be noted that for an isotropic material, where the material properties are constant (i.e., $\mathscr{X} = \mathscr{M} = 0$), the model yields to the one of isotropic materials given in Ref.[36].

2.1. Peridynamic discretization

In PD and so any other mesh-free approach, in order to numerically implement the integro-differential equations, the body is discretized into uniformly distributed material points having discrete volumes, V. these volumes are then grouped into material point families, as depicted in Fig.2.3. The interaction of any material point in PD is set to exist with the points within its family, only. However, some points may not completely fall inside the family of a specific material point, thereby, resulting in a volume truncation, as seen in Fig.2.4. Therefore, in such cases a linearly approximated correction factor is calculated as follows to determine the truncated volumes [36]:

$$V_{fac}^{(i)(j)} = \frac{\delta + \Delta x/2 - r_{(i)(j)}}{\Delta x} \tag{2.15}$$

Here, $r_{(i)(j)} \in [\delta - \Delta x/2, \delta]$ is the distance between point i and its neighbour point j. Then the equation of motion in PD for any point $i \ni [i \in \mathscr{N}]$ can be written in its discrete form using the corrected volumes, $V' = V_{fac}V$, as follows:

$$\rho_i \ddot{\mathbf{u}}_i = \sum_{j=1}^{N_i^{\mathscr{H}}} (\mathbf{t}^{\mathscr{H}}_{(i)(j)} - \mathbf{t}^{\mathscr{H}}_{(j)(i)})V'_{(j)} + \sum_{j=1}^{N_i^{\mathscr{X}}} (\mathbf{t}^{\mathscr{X}}_{(i)(j)} - \mathbf{t}^{\mathscr{X}}_{(j)(i)})V'_{(j)} + \sum_{j=1}^{N_i^{\mathscr{M}}} (\mathbf{t}^{\mathscr{M}}_{(i)(j)} - \mathbf{t}^{\mathscr{M}}_{(j)(i)})V'_{(j)} + \mathbf{b}_{(i)} \tag{2.16}$$

or

$$\rho_i \ddot{\mathbf{u}}_i = \sum_{j=1}^{N_i^{\mathscr{H}}} \beta^{\mathscr{H}}_{(i)(j)} \, \hat{\mathbf{e}} \, V'_{(j)} + \sum_{j=1}^{N_i^{\mathscr{X}}} \beta^{\mathscr{X}}_{(i)(j)} \, \hat{\mathbf{e}} \, V'_{(j)} + \sum_{j=1}^{N_i^{\mathscr{M}}} \beta^{\mathscr{M}}_{(i)(j)} \, \hat{\mathbf{e}} \, V'_{(j)} + \mathbf{b}_{(i)} \tag{2.17}$$

where $N_i^{\mathscr{H}}$, $N_i^{\mathscr{X}}$, and $N_i^{\mathscr{M}}$ are the number of neighbours of point i with equal, higher, and lower material properties, respectively. After substituting for the terms $\beta_{(i)(j)}^{\mathscr{H}}$, $\beta_{(i)(j)}^{\mathscr{X}}$, and $\beta_{(i)(j)}^{\mathscr{M}}$ the equation of motion can be achieved in its final form as:

$$\begin{aligned}\rho_i \ddot{\mathbf{u}}_i = 2\delta \sum_{j=1}^{N_i^{\mathscr{H}}} \left[\alpha \mu_{(i)} S_{(i)(j)} + \frac{\phi_{(i)}}{\pi h \delta^3} \frac{\Lambda_{(i)(j)}}{|\Delta \mathbf{x}_{(i)(j)}|} (\theta_{(i)} + \theta_{(j)}) \right] \hat{\mathbf{e}}\, V_j' \\ + \frac{2\delta}{\psi+1} \sum_{j=1}^{N_i^{\mathscr{X}}} \left[\alpha (\psi \mu_{(i)} + \mu_{(j)}) S_{(i)(j)} + \frac{(\psi \phi_{(i)} + \phi_{(j)})}{\pi h \delta^3} \frac{\Lambda_{(i)(j)}}{|\Delta \mathbf{x}_{(i)(j)}|} (\theta_{(i)} + \theta_{(j)}) \right] \hat{\mathbf{e}}\, V_j' \\ + \frac{2\delta}{\psi+1} \sum_{j=1}^{N_i^{\mathscr{X}}} \left[\alpha (\mu_{(i)} + \psi \mu_{(j)}) S_{(i)(j)} + \frac{(\phi_{(i)} + \psi \phi_{(j)})}{\pi h \delta^3} \frac{\Lambda_{(i)(j)}}{|\Delta \mathbf{x}_{(i)(j)}|} (\theta_{(i)} + \theta_{(j)}) \right] \hat{\mathbf{e}}\, V_j'\end{aligned} \tag{2.18}$$

with the dilatation terms discretized as follows:

$$\theta_{(i)} = \frac{2}{\pi h \delta^2} \sum_{p=1}^{N_{(i)}} S_{(i)(p)} \Lambda_{(i)(p)}\, V_{(p)}' \tag{2.19a}$$

$$\theta_{(j)} = \frac{2}{\pi h \delta^2} \sum_{k=1}^{N_{(j)}} S_{(j)(k)} \Lambda_{(j)(k)}\, V_{(k)}' \tag{2.19b}$$

in which $N_{(i)}$ and $N_{(j)}$ are the total number of points in the family of point i and j, respectively.

2.2. PD corrections

One of the major drawbacks of non-local approaches is the truncation of the non-locality range, i.e., horizon. In a PD domain, this truncation effect can either arise from geometric (Type-G) or material (Type-I) discontinuities, as shown in Fig.2.5. In traditional PD, as the formulations fail to address the interface effects with enough accuracy,

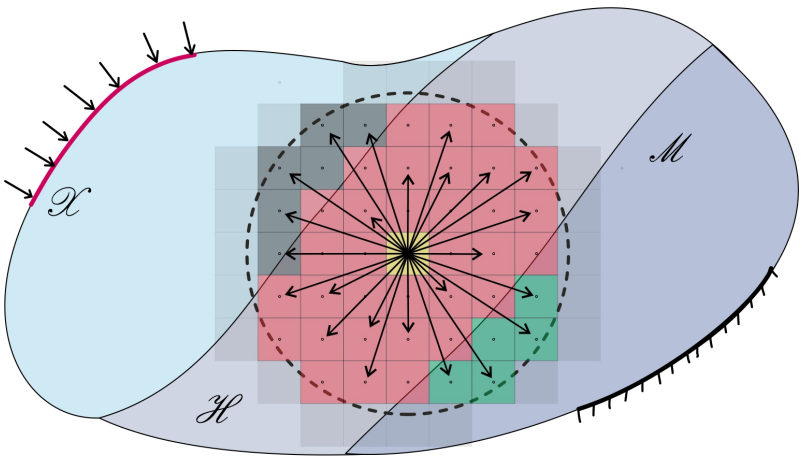

Figure 2.3: Discretized PD domain

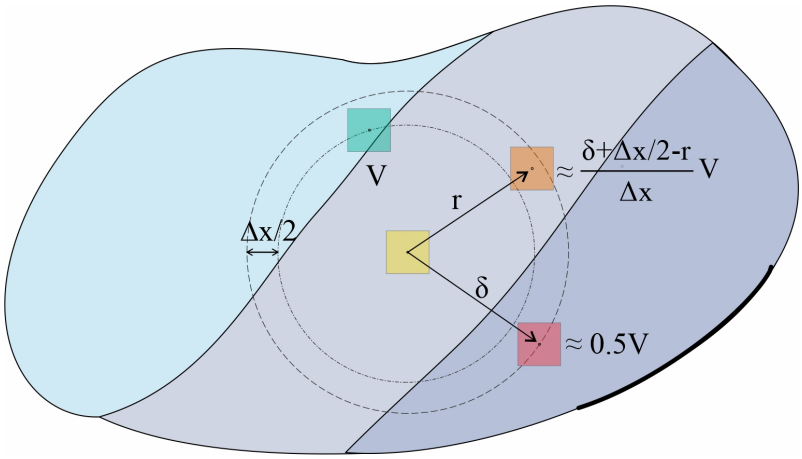

Figure 2.4: Volume truncation effect

a correction is applied to both Type-I and Type-G truncations [36]. However, the present formulation only requires a correction on Type-G truncations, given that the interface effects are modeled by the ψ parameter with enough sensitivity. A general approach, based on the comparison of the results obtained from classical continuum mechanics (CCM) with the ones of PD [36], is adopted here for Type-G corrections which is applied only to the points of the boundary regions. The correction factors are calculated for both dilatation and strain energy density of the points as follows:

$$SED_i^{cor} = \frac{4\mu_{(i)}\varepsilon^2}{W_{\mathscr{X}_{(i)}} + W_{\mathscr{H}_{(i)}} + W_{\mathscr{M}_{(i)}}} \tag{2.20}$$

$$DIL_i^{cor} = \frac{2\varepsilon}{\theta_{(i)}} \tag{2.21}$$

in which ε is the deliberately applied displacement amount in x and y direction.

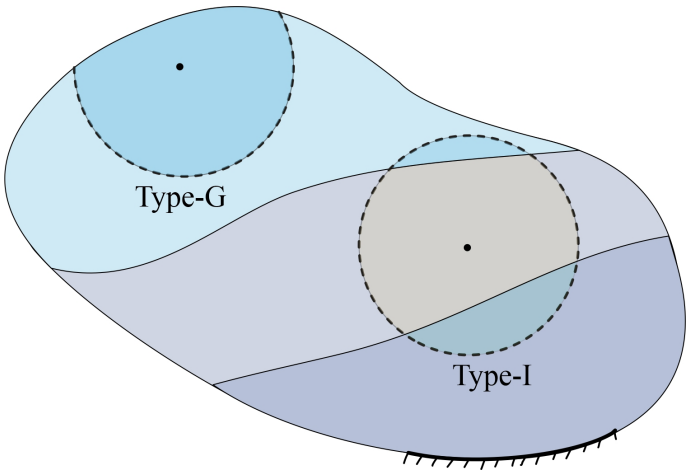

Figure 2.5: Type-G and Type-I truncations in PD

2.3. Damage modeling in FGMs

In PD the propagation of a crack is controlled by breakage of the bonds, where a bond is assumed to be broken if the stretch, S, exceeds the critical stretch, S^c. With the inclusion of the dominancy rate, the equation of the critical stretch value for any bond ij in a two-dimensional case should be updated as follows:

$$S^c_{(i)(j)} = \begin{cases} \sqrt{\frac{2G_c^{(i)}}{\frac{32\delta}{9\pi^2}\phi_{(i)}+\alpha\mu_{(i)}}} & if \quad j \in \mathscr{H}_i \\ \sqrt{\frac{2(\psi G_c^{(i)}+G_c^{(j)})}{\frac{32\delta}{9\pi^2}(\psi\phi_{(i)}+\phi_{(j)})+\alpha(\psi\mu_{(i)}+\mu_{(j)})}} & if \quad j \in \mathscr{X}_i \\ \sqrt{\frac{2(G_c^{(i)}+\psi G_c^{(j)})}{\frac{32\delta}{9\pi^2}(\phi_{(i)}+\psi\phi_{(j)})+\alpha(\mu_{(i)}+\psi\mu_{(j)})}} & if \quad j \in \mathscr{M}_i \end{cases} \tag{2.22}$$

where G_c represents the critical energy release rate. Furthermore, a damage criterion is introduced as in Eq.(2.23) to account for the total damage of a point:

$$\varphi_{(i)} = 1 - \frac{\sum_{p=1}^{N_{(i)}} \lambda_{(i)(j)} V'_{(j)}}{\sum_{j=1}^{N_{(i)}} V'_{(j)}} \tag{2.23}$$

Herein, $\lambda_{(i)(j)}$ is the piecewise control function over the breakage of the bond ij. Hence:

$$\lambda_{(i)(j)} = \begin{cases} 1 & if \quad S_{(i)(j)} \leq S^c_{(i)(j)} \\ 0 & otherwise \end{cases} \tag{2.24}$$

Finally, a forward-step integration scheme is adopted to explicitly integrate the equation of motion with respect to time. For which, the optimum time-step size can be calculated using the standard Von Neumann stability analysis [37] as:

$$dt^c = 0.8\sqrt{\frac{\chi_{min}}{\pi\alpha\delta^3}} \tag{2.25}$$

where χ_{min} is the minimum possible value of $\rho_{(i)}/\mu_{(i)}$ such that $i \in \mathscr{N}$.

2.4. PD implementation and algorithms

The overall PD algorithm is mainly composed of two modules, a preprocess and a time integration module, as shown in Algorithm 1. The program starts by acquiring the necessary inputs and assigning initialized storage IDs for field variables. Although, the row-storage method is generally preferred because of its faster access speed, herein, a matrix-storage system is used due to its easier accessibility in complex sub-region domains. Hence, throughout this study the $[i, j]$ notation refers to the point located at i^{th}

row in x- and j^{th} row in y-directions. The left bottom corner of the geometry is taken as the zero-reference point while discretizing the domain into material points, as shown in Algorithm 2. The major blocks in pre-process module are the determination of family members (Algorithm 3) and calculation of correction factors (Algorithm 4). The *members*, *NoM*, and *address* arrays are used to store PD interactions, number of interactions per each family, and address of the first interaction for each family in *members* array, respectively. The *type* array is used to store the type of the material domain of the neighboring points. Hence, it is, in turn, 0, 1 and -1 for $\mathscr{H}$, $\mathscr{X}$, and $\mathscr{M}$ domains. Furthermore, for the cases bearing pre-existing cracks with different orientations, an easily comprehended methodology, given in Algorithm 5 is adopted, in which *fail_flag* array is used to store the healthy and broken bonds as 1 and 0 values, respectively.

The time integration module is consisted of a single step routine, as given in Algorithm 6, and a result output step. It should be noted that these routines are given for dynamic loading conditions. For a static case one may change the sequence of solution by taking the force boundary conditions out of the time integration loop and applying a faster convergence methodology such as adaptive dynamic relaxation [38]. The flow chart of the overall solution procedure for the proposed formulations in this thesis is given in Fig.2.6.

Algorithm 1 PD solver

```
    <Preprocess>
 1:   ▷ Get input
 2:   ▷ Discretize domain
 3:   ▷ Apply material sub-regions (if exist)
 4:   ▷ Apply holes (if exist)
 5:   ▷ Determine PD families
 6:   ▷ Calculate PD correction factors
 7:   ▷ Apply pre-existing crack(s) (if exist)
 8: <Time integration>
 9: for t ← 1 to Total time-steps do
10:     ▷ Do singel step calculations
11:     ▷ Write results
12: end for
```

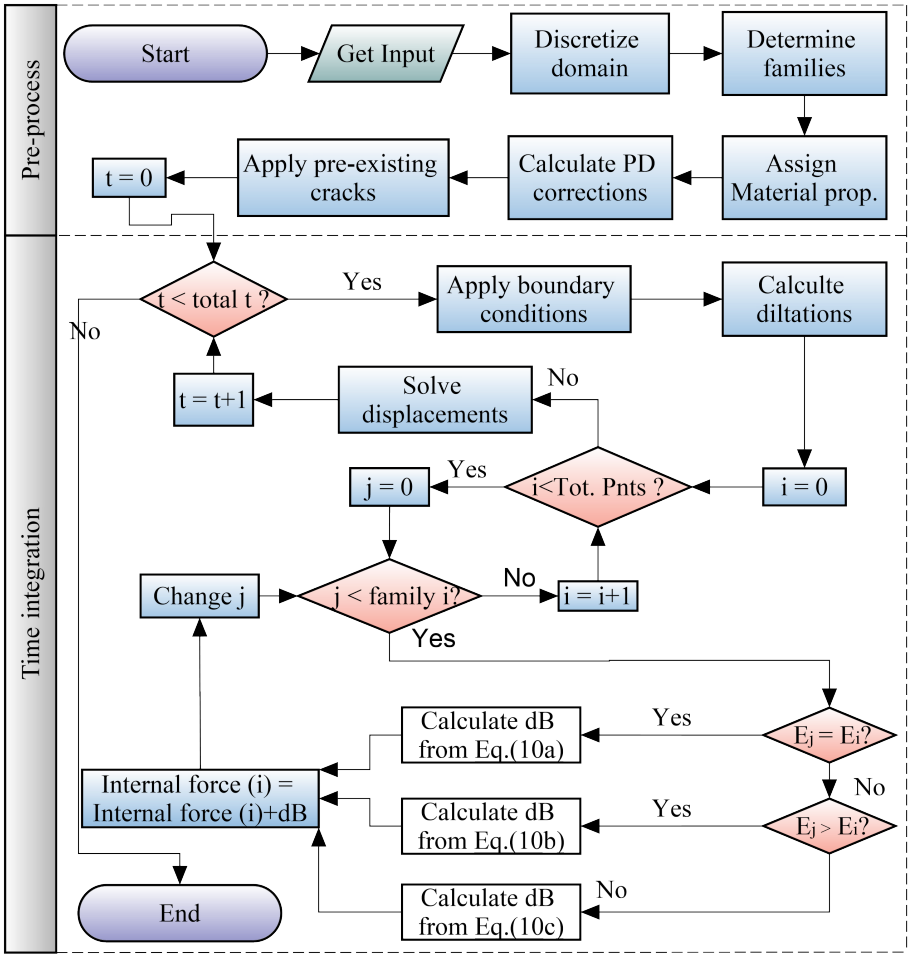

Figure 2.6: General solution procedure of PD

Algorithm 2 Discretize PD domain

```
tpx ← Length/Δx
tpy ← Width/Δx
for j ← 1 to tpy do
    for i ← 1 to tpx do
        xcord [i,j] ← (i − 1)Δx + Δx/2
        ycord [i,j] ← (j − 1)Δx + Δx/2
    end for
end for
```

Algorithm 3 Determine PD families

```
initialize → count, members, NoM, address, type
tpy ← Number of points in y-direction
tpy ← Number of points in x-direction
for j ← 1 to tpy do
    j0s = max(1, j−δ/Δx − 1)
    j0f = min(tpy, j+δ/Δx + 1)
    for i ← 1 to tpx do
        i0s = max(1, i−δ/Δx − 1)
        i0f = min(tpy, i+δ/Δx + 1)
        xcordi ← xcord(i,j)
        ycordi ← ycord(i,j)
        for j0 ← j0s to j0f do
            for i0 ← i0s to i0f do
                xcordj ← xcord(i0,j0)
                ycordj ← ycord(i0,j0)
                r= √((xcordi − xcordj)^2 + (ycordi − ycordj)^2)
                if r ≤ δ then
                    members[count,0]=i0
                    members[count,1]=j0
                    NoM[i,j]=NoM[i,j]+1          ▷ Sum number of members
                    if E[i0, j0] = E[i, j] then type[count]=0
                    elseif E[i0, j0] > E[i, j] then type[count]=1
                    else type[count]=-1
                    count=count+1;
                end if
            end for
        end for
        address[i,j] ← count-NoM[i,j]
    end for
end for
```

Algorithm 4 Calculate PD correction factors

```
▷ Apply displacement increments in x- and y-direction
for j ← 1 to tpy do
    for i ← 1 to tpx do
        for k ← 0 to NoM(i,j) do
            i0 ← members[address[i,j]+k,0]
            j0 ← members[address[i,j]+k,1]
            neighbour point ← point [i0,j0]
            ▷ Calculate volume correctin factors from Eq.2.15
            ▷ Calculate dilatation correctin factors from Eq.2.21
            ▷ Calculate SED correctin factors from Eq.2.20
        end for
    end for
end for
```

Algorithm 5 Apply pre-existing crack

```
fail_flag ← 1
xcs ← x start of the crack
ycs ← y start of the crack
xcf ← x finish of the crack
ycf ← y finish of the crack
cslope ← slope of the crack
for j ← 1 to tpy do
    for i ← 1 to tpx do
        xbs ← xcord[i,j]
        ybs ← ycord[i,j]
        for k ← 1 to NoM[i,j] do
            i0 ← members[address[i,j]+k,0]
            j0 ← members[address[i,j]+k,1]
            xbf ← xcord[i0,j0]
            ybf ← ycord[i0,j0]
            bslope ← slope of the bond
            if cslope ≠ bslope then
                xint ← x intersection of bond and crack
                yint ← y intersection of bond and crack
                if xbs ≤ xint ≤ xbf and ybs ≤ yint ≤ ybf then
                    if xcs ≤ xint ≤ xcf and ycs ≤ yint ≤ ycf then
                        fail_flag[(j-1)tpx+i,k]=0
                    end if
                end if
            end if
        end for
    end for
end for
```

Algorithm 6 Single step calculations for dynamic solution in PD

```
▷ Apply force boundary conditions
▷ Apply displacement boundary conditions
▷ Calculate dilatations from Eq.2.19
for j ← 1 to tpy do
    for i ← 1 to tpx do
        ▷ initialize dB
        for all family members do
            if bond is not broken then
                bndn ← address[i,j]+k
                i0 ← members[bndn,0]
                j0 ← members[bndn,1]
                dtype ← type[bndn]
                neighbour point ← point[i0,j0]
                Calculate stretch, S
                If S > S^c then break the bond
                if dtype=0 then
                    dB ← Eq.2.10a
                else if dtype > 0 then
                    dB ← Eq.2.10b
                else
                    dB ← Eq.2.10c
                end if
                internal force [i,j] ← internal force [i,j]+dB
            end if
        end for
    end for
end for
for j ← 1 to tpy do
    for i ← 1 to tpx do
        ▷ Calculate accleration[i,j]
        ▷ Calculate velocity[i,j]
        ▷ Calculate displacement[i,j]
    end for
end for
```

Part II

Overview of Part II

Part II of this thesis includes the numerical implementations of toughening mechanisms in homogeneous and functionally graded materials (FGMs) each corresponding to a chapter. The present OSB-PD formulations are implemented as an in-house code using the C++ programming language. A linear-elastic and plane stress condition is assumed for the study cases throughout this thesis.

In the first chapter of this part, a published article is presented in which traditional OSB-PD is used to introduce toughening mechanisms for homogeneous materials. The toughening model comprises various combinations of void internal features which are exemplified by stop-holes. In this chapter, the effects of the position and shape of stop-holes on toughness enhancement of brittle homogeneous materials are investigated under different loading and fracture mode conditions. Here, it is revealed that how an optimum enhancement effect can be achieved by changing the distance, shape and combinations of stop-holes.

The second chapter of this part addresses the shortcomings of traditional peridynamics in modeling interfaces and high gradient FGMs. This chapter mainly focuses on the effects of the newly introduced peridynamic parameter, *the dominancy rate*, in modeling gradient transitions and jumps in the material properties under dynamic and static loading conditions. The accuracy of the model is investigated for 0.1 up to 1000 $times$ order of magnitudes of the change in material properties. Herein, it is shown that how the properties of a bond are affected by the properties of its constituent points and how their relation with the *dominancy rate* parameter should be. This chapter further presents numerically validated toughening models with the help of which the strength of FGMs against crack propagations can highly be enhanced.

3

An Ordinary State-Based Peridynamic Model for Toughness Enhancement of Brittle Materials through Drilling Stop-Holes

Mohammad Naqib Rahimi, Adnan Kefal, Mehmet Yildiz, Erkan Oterkus
Published in: International Journal of Mechanical Science
https://doi.org/10.1016/j.ijmecsci.2020.105773

3.1. Abstract

In this paper, the ordinary state-based peridynamic (OSB-PD) is used to simulate and study the effects of different-shaped stop-holes with different combinations on crack dynamics in brittle materials in order to establish a detailed knowledge about the toughening effect of internal features that can be in the form of holes and pores. Using the traditional OSB-PD analyses, a new easy-to-apply technique is introduced to toughen the materials against crack propagations. As a first case study, the high accuracy of peridynamic approach in damage prediction is demonstrated through solving a collection of numerical and experimental benchmark problems. Moreover, the bi-hole, parabolic, branched, bi-parabolic, and mixed-parabolic combinations of stop-holes under tensile loading, and the T-shape, I-shape, bi-linear, linear, and linear-parabolic combinations of stop-holes under shear loading are suggested for notably enhancing material toughness and are practically and functionally compared with each other. In general, the suggested geometries are proven to be highly effective on toughness enhancement of materials with a relative ease of implementation, in comparison to other internal features such as micro-cracks. Additionally, a further case study is carried out on the effects of the distance of stop-holes from the initial crack-tip on crack dynamics and material toughness, in which it is observed that every hole has a specific μ-range, and thus, the crack dynamics are affected by the hole if and only if the crack enters this range. Overall, the arrestment and accelerating effects of the stop-holes on crack dynamics are carefully explained in numeric and conceptual perspectives, which will help engineers and designers to maximize the positive effects of stop-holes on material toughness and design a tougher micro-structural material using easily applied defects.

Keywords: Peridynamics; fracture mechanics; non-local approaches; stop-holes; material toughening.

3.2. Introduction

Making a perforation, i.e., stop-hole, at the vicinity of the growing cracks is one of the widely used toughening models to reduce the crack growth rate in brittle materials. The existence of a hole has two major effects on dynamics of the crack in a body, namely as arresting and accelerating effects. Any growing crack tends to accelerate towards the hole located in the vicinity of its tip or along its original propagation path. On the other hand, when a crack joins the hole, the hole arrests the growing crack for a significant amount of time causing the crack to release its strain energy accumulation, thereby resulting in a longer crack growth life [39]. Among early studies available in literature, Broek [13] experimentally investigated the accelerating effects of stop-holes on crack dynamics in a continuum by allocating a stop-hole on propagation path of the crack. Miyagawa et al.[14] later demonstrated the arresting effects of holes by extending Broek's investigation to two and four hole combinations. Several researchers have investigated the arresting effect of stop-holes drilled at the vicinity of the pre-existing crack and have suggested drilling stop-holes as a repairing technique for the cracked parts of structures. For instance, Fu et. al.[40] investigated the effects of one and two drilled stop-holes on the fatigue life of steel bridge deck. The evidence of their study indicated an increase in the fatigue life with a directly proportional relation to the diameter of the drilled stop-hole. Ghfiri et al.[41] used the hole-expansion method to introduce residual stresses that can reduce the effective stress around the crack tip under axial fatigue test. Similarly, Song et. al.[42] used stop-hole drilling procedure to improve the fatigue life of aluminium alloys and stainless steel. Aside from these experimental works, Ayatollahi et al.[43] numerically investigated the effects of drilling one stop-hole based on classical fracture mechanics model, in which their main variable was the size of the stop-hole. As is evident, most of the works on stop-holes have been focused on the effects of a singular hole. Only recently, Ferdous et al.[9] investigated the effect of four uniformly distributed stop-holes on fatigue life of specimens.

Although several of the above researchers have numerically/experimentally studied the effects of one circular stop-hole on crack propagation path and fatigue life, to the best of authors' knowledge, no literature has been dedicated to the investigation of the effects of the "linear" and/or "non-linear" combinations of more than one stop-hole on material toughness under "tensile" and "shear" loadings. Hence, the main novelty of the current study is to present a detailed knowledge about the various toughening effects of stop-hole combinations through the OSB-PD analyses, while introducing a new approach of implementing linear and/or nonlinear combinations of stop-holes as a material toughening technique.

3.3. Numerical Examples

3.3.1. Homogeneous plate with holes under dynamic loading

This problem was originally solved in [44] using dynamic phase field method (DPF) and was compared with experimental results. The authors investigated the effects of circular holes on crack propagation path, which are placed in a parallel combination to a pre-existing crack with a length of $l = 2mm$ in a poly methyl methacrylate (PMMA) plate with dimensions $LxW = 50mmx25mm$. The material properties of PMMA are given in Table 3.1. Four different geometries were considered for the plate and were subjected to a uni-axial loading, as shown in Fig.3.1). Herein, the problem is solved using traditional OSB-PD approach to validate the present algorithm and its implementation on similar cases. The plate is uniformly discretized using $200x100$ material points along the length and width directions, respectively, leading to uniform particle spacing of $\Delta x = 0.25mm$. In order to reduce the computation time, the cross-head velocity boundary condition is applied as $300mm/s$ and is deployed on a virtual boundary of three layers (of material points) at the top and the bottom boundaries of the plates having a thickness equal to Δx.

Consequently, the crack in geometries a, b, c, and d starts to propagate after approximately 2900^{th} time-step. To gain a foreknowledge of the crack propagation paths and understand physical interface of the crack growth, we investigate the displacement and strain energy distributions in the geometries at an instant of time before propagation initiation, i.e., 2600^{th} time-step. Accordingly, the x and y displacements of geometries a, b,

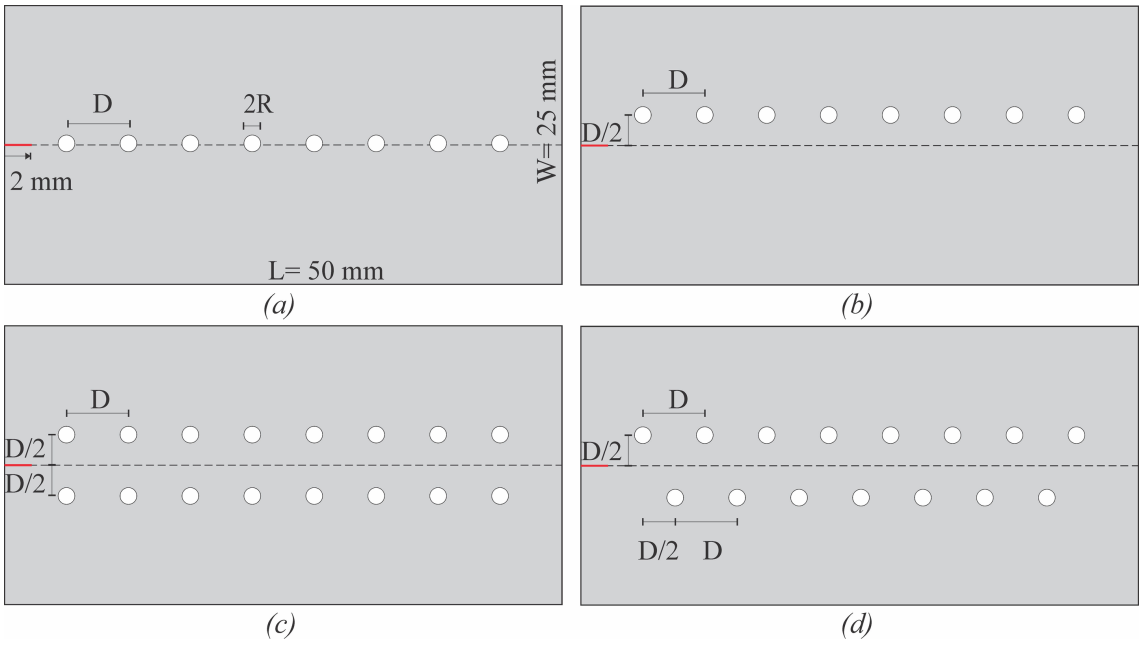

Figure 3.1: Geometric properties of homogeneous plates under dynamic loading with 2R=3L/100 and D=L/9

Table 3.1: Material properties of homogeneous plate under dynamic loading

E	v	ρ	G_c
3.24 GPa	0.35	1190 Kg/m^3	200 J/m^2

c, and d at 2600^{th} time-step are presented in Fig.3.2, where the spatial variation of the displacement contours precisely matches with the expected physical/mechanical response of the tensile loading. Moreover, a high vertical displacement jump is observed in the region of the pre-existing crack demonstrating the crack opening in this region which finally leads to a mode-I fracture loading. In fact, any increase in relative displacement of two adjacent material points causes an increase in strain energy density of the bond between these points. If the strain energy density (or stretch) of a bond exceeds the critical strain energy density (or critical stretch), the bond breaks. Fig.3.3 shows the distribution of the

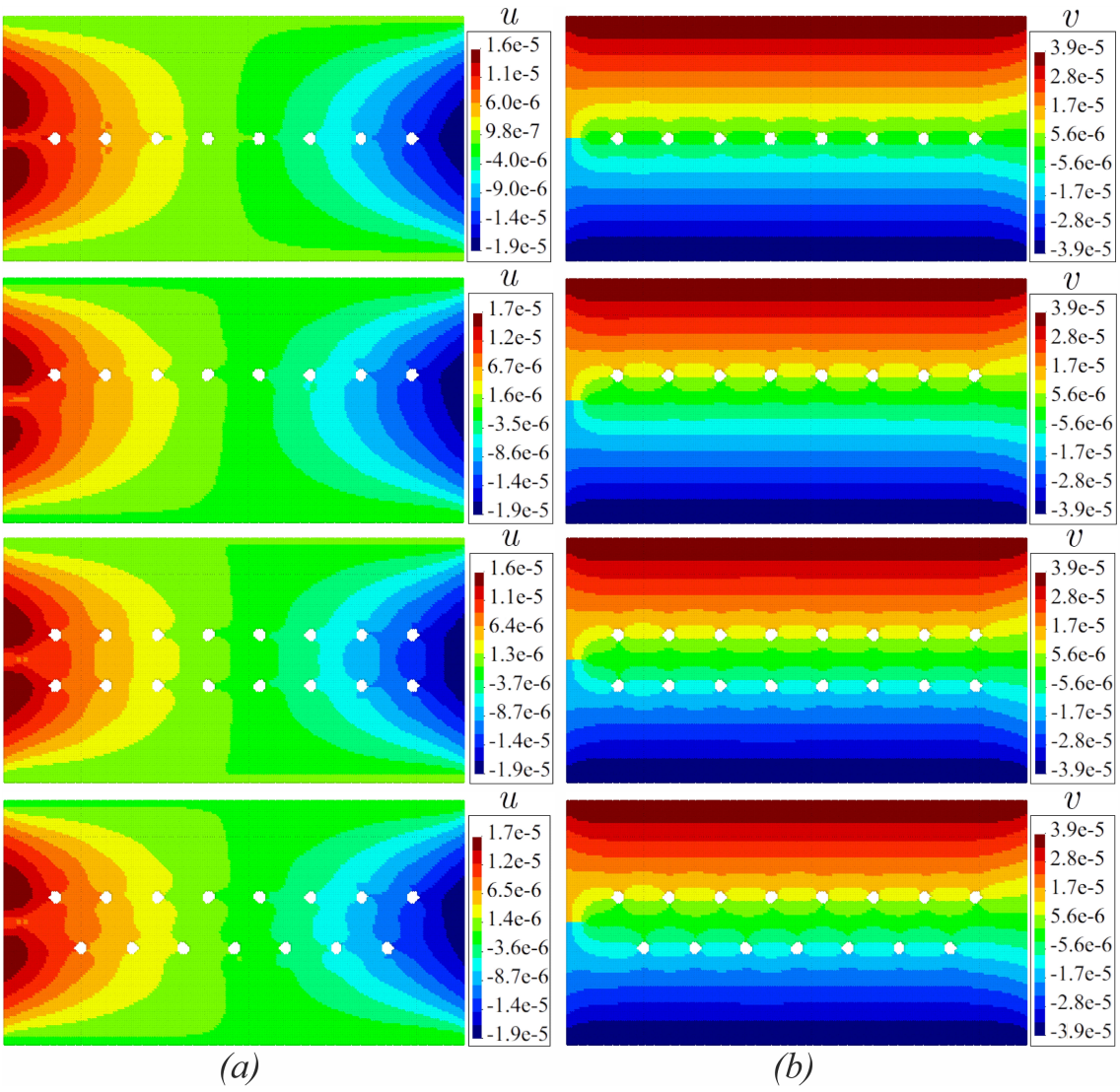

Figure 3.2: Displacement in a) x-direction, u [m], and b) y-direction, v [m], of geometry a, b, c, and d at 2600^{th} time-step

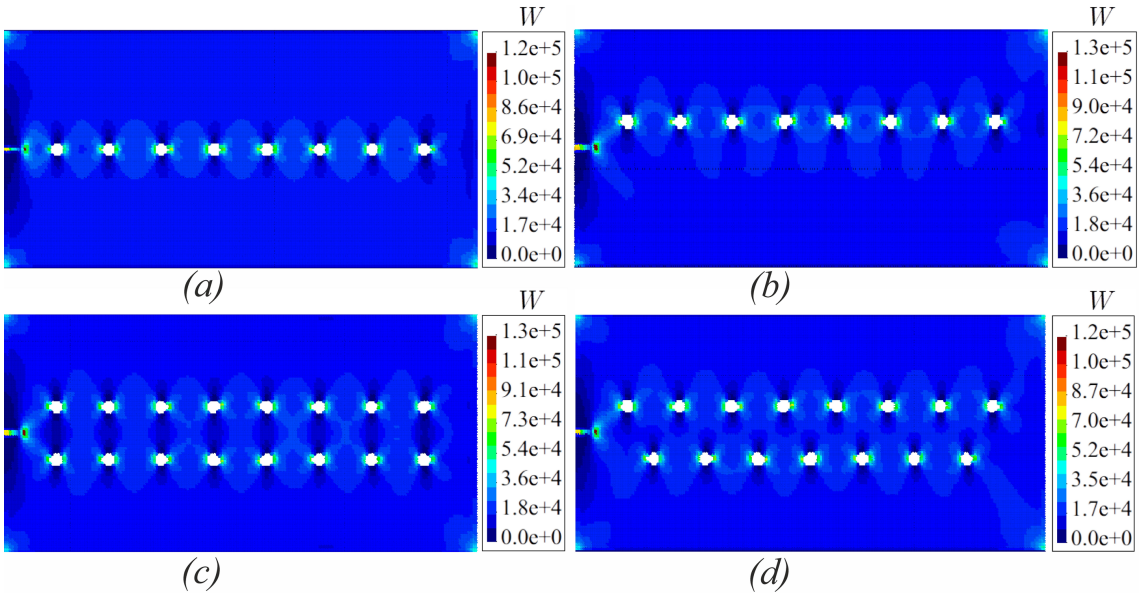

Figure 3.3: Strain energy densities, $W\,[J/m^3]$, of the geometries at 2600^{th} time-step

strain energy density over the plate at 2600^{th} time-step for each geometry. As can be seen, micro-cracks are likely to be born from perimeter of the holes in geometry b, c and

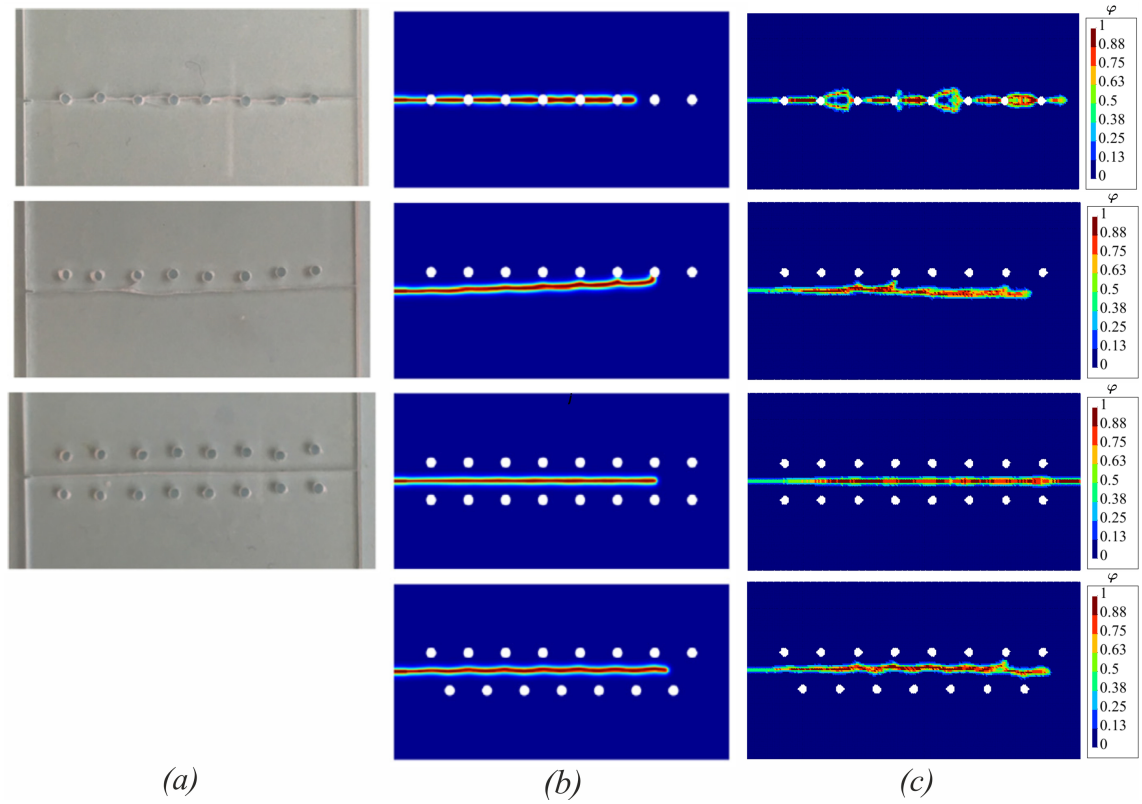

Figure 3.4: Comparison of the results obtained from a) experiments [44], b) DPF [44] and c) OSB-PD analyses where the first row represents geometry a; second row represents geometry b; third row represents geometry c and fourth row represents geometry d

d since the strain energy densities of the points near the holes are relatively higher than the ones located in the far field. However, the experimental results demonstrate no generation of new cracks from the holes (Fig.3.4). This may be attributed to the increased fracture toughness of cut-out surfaces of the holes due to the drilling process [45]. To comply with such phase change of material, the critical stretch value for two material layers around the holes are doubled for all geometries. This prevents the generation of micro-crack formations around the hole, thus resulting in a more elastic material properties in this region. Moreover, if the spacing between material points is small enough (a finer mesh), the region with increased elasticity becomes very small, thus, providing a negligible effect on behavior of the main crack.

The above results of OSB-PD analyses are compared with those of DPF analysis and experiment [44] in Fig.3.4. A superior prediction of the crack paths in geometries a and b is obtained using the traditional OSB-PD implementation. OSB-PD was able to capture the branching effect of the crack in geometry a, which is much similar to the experimental result where the branching effect is seen after the third and the fifth holes (Fig.3.4). On the other hand, a small amount of crack branching is also predicted in other regions of the crack propagation path in geometry a, which may be attributed to the different velocity boundary conditions applied herein [46]. Furthermore, the results obtained for geometry b using OSB-PD approach sufficiently indicates the higher accuracy of the prediction of the crack path by OSB-PD analyses. In geometry b, the propagation path predicted by DPF eventually joins the holes whereas the OSB-PD method predicts an almost parallel propagation path to the horizontal, which is quite similar to the real propagation path of the crack observed in experiment.

3.3.2. Diagonally Loaded Square Plate (DLSP)

To further indicate the accuracy and robustness of present algorithm, a fracture test configuration, named as the “DLSP (Diagonally Loaded Square Plate) specimen [47]”, is solved under pure mode-I, pure mode-II, and mixed mode I-II fracture loading conditions and is validated against the experimental results. The modeled geometry has the following dimensions and crack orientations: side length of $2w = 150\,mm$, thickness of $h = 5\,mm$, and a crack with an initial length of $2a = 45\,mm$ located at the center of the plate with an angle of α. The material properties of the plate are given in Table 3.2. A set of numerical

Table 3.2: Material properties of the DLSP test specimen

E	v	ρ	G_c
$2.94\,GPa$	0.38	$1200\,Kg/m^3$	$602\,J/m^2$

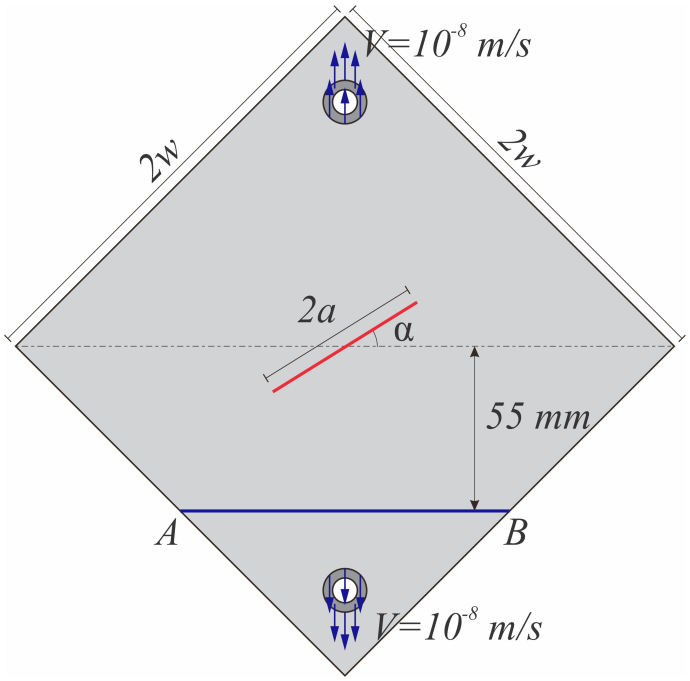

Figure 3.5: Geometric properties of DLSP specimen

configurations is analyzed under the velocity boundary condition of $V = 10^{-8} m/s$ to achieve a quasi-static loading condition. The velocity condition is applied to three layers of material points around the upper and lower circular cut-outs of the plate as depicted

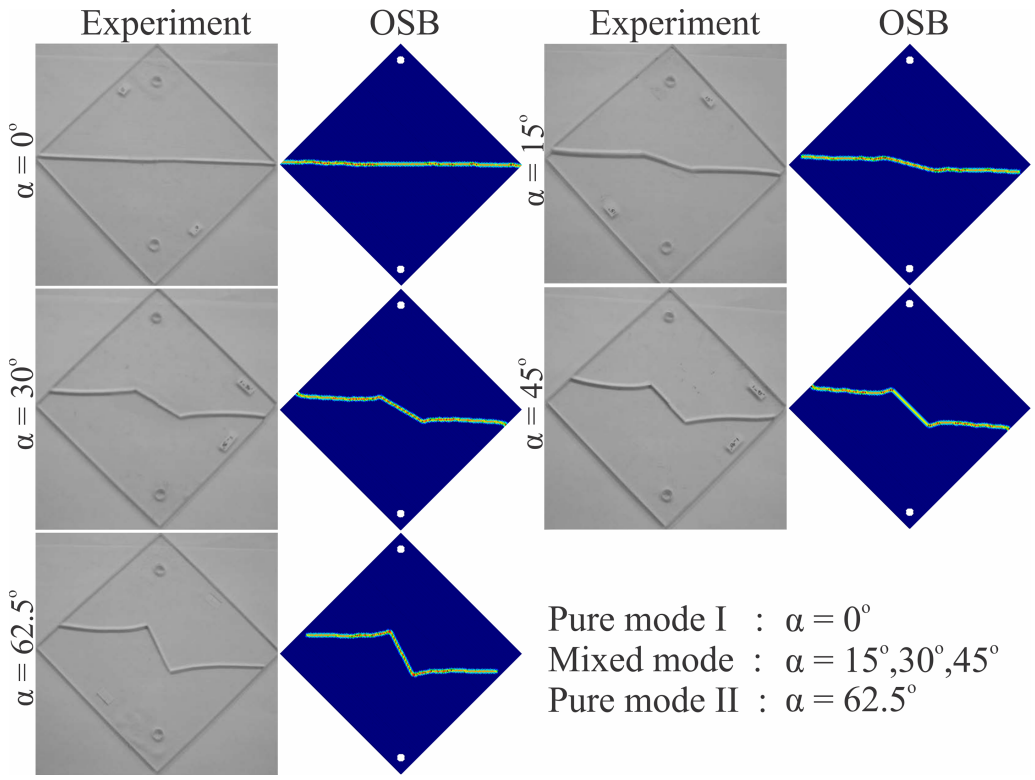

Figure 3.6: Comparison of the final crack path of the experiments and OSB results for DLSP specimens

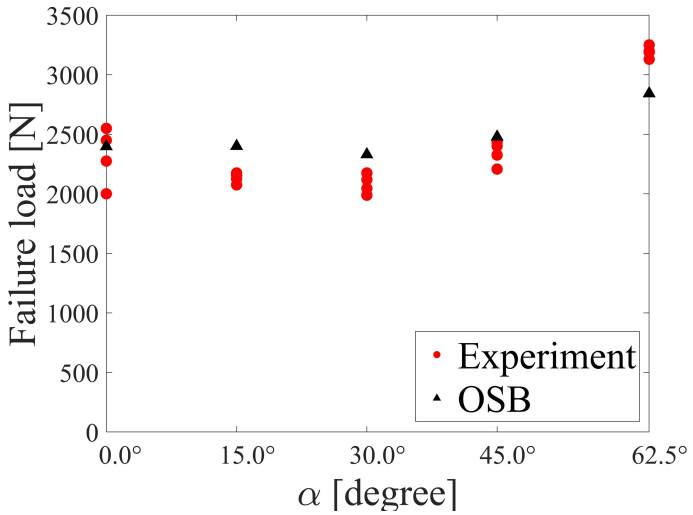

Figure 3.7: Comparison of the Failure load of the experiments and OSB results for DLSP specimens

in Fig.3.5. The DLSP domain is discretized into $150x150$ points with particle spacing of $\Delta x = 1\,mm$. The quasi-static displacement solution is achieved using adaptive dynamic relaxation method [38]. The analyses are run for a total of 40000 time-steps with a time-step size of $dt = 1s$. Fig.3.6 shows a comparison of the final crack path obtained from OSB analyses with the experimental ones for α values of 0^o, 15^o, 30^o, 45^o, and 62.5^o. The specific value of $\alpha = 0^o$ corresponds to the pure mode-I loading condition. The angle, $\alpha = 62.5^o$ with $a/w = 0.3$ corresponds to a pure mode-II loading whereas the α values between 0 and 62.5 leads to the mixed mode I-II. The failure loads are monitored by summing the forces over the interactions passing through the line AB and are compared with the experimental results in Fig.3.7. The results obtained from the OSB-PD analyses are in a good agreement with the ones of experiments in terms of both the final crack path and internal forces. Hence, it can be stated that the algorithm used herein is able to model the crack dynamics reliably under any in-plane loading conditions.

3.3.3. Stop-hole combinations under uniaxial loading

In this section, different combinations of stop-holes are applied to a PMMA plate, with dimensions $LxW = 50mmx50mm$ and material properties given in Table 3.2, to strengthen the plate against crack propagation under tensile loading condition. A pre-existing crack with a length of $25\,mm$ is located at the left-middle part of all geometries (Fig.3.8). The geometries are then subjected to a velocity boundary condition with a cross-head velocity of $5\,m/s$, representing a uni-axial loading at the top and bottom boundaries. All the analyses are performed for the differential time-step of $dt = 4.0e^{-8}\,s$, which is lower than the stable dt value proposed in Eq.(2.25). To obtain a fine PD model, $500x500$ material points are used in the discretization of the plate domain. Firstly, the ge-

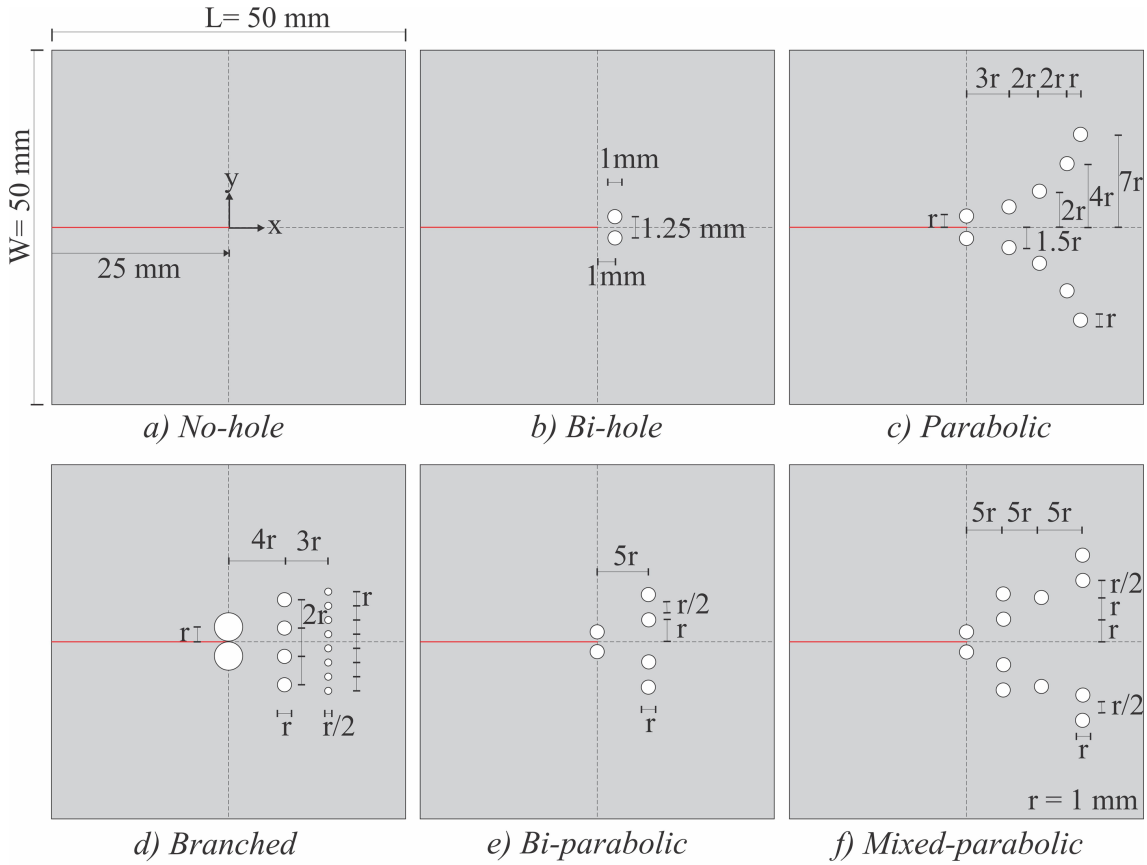

Figure 3.8: Geometric properties of stop-hole combinations under shear loading with $r = 1mm$

ometry with no hole (Fig.3.8a) is solved to have a reference on the dynamics of the crack and to determine the time-steps for the start of crack propagation and complete rupture. As a result, the crack propagation is observed to start approximately after 500^{th} time-step and eventually causing the complete rupture to happen after nearly 1650 time-steps, which are considered as the reference of crack propagation interval for the following analyses. Six different combinations of stop-holes, namely the No-hole, Bi-hole, Parabolic, Branched, Bi-parabolic and Mixed-parabolic cases, are considered in the plate domain for toughness enhancement (Fig.3.8). A similar case to the Bi-hole combination was also solved in Ref.[48], where the authors used two horizontal micro-cracks in order to investigate the influence of micro-cracks on main-crack dynamics. When the diameters of the applied holes are significantly small, holes and micro-cracks behave geometrically alike each other. However, if the diameters of the holes are large enough, the strain energy concentration is dispersed along the perimeter of the holes, which is in contrary to the case of micro-cracks, where the strain energy concentration occurs at the singular crack-tips. Therefore, stop-holes can cause a decrease in the average velocity of the main crack propagation as opposed to the particular case in Ref.[48], where two parallel micro-cracks near the main crack tip accelerated the crack propagation.

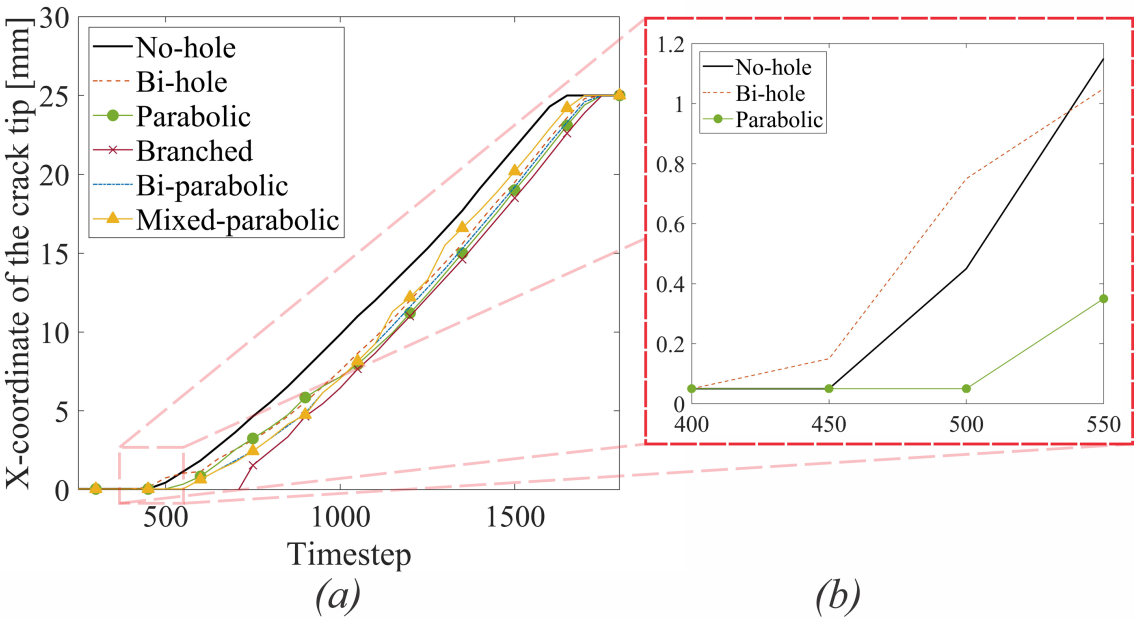

Figure 3.9: The graph of crack propagation vs time-step for No-hole, Bi-hole, Parabolic, Branched, Bi-parabolic and Mixed-parabolic stop-hole combinations

The six different cases are compared with each other by means of crack growth rate for every 50 time-steps in Fig.3.9. It is clear from the graph that almost every combination of holes caused a delay in crack initiation time. The slopes of the lines in the graph imply the average velocity of crack propagation with the unit of mm/time-step. A relatively higher average propagation velocity is seen for some combinations of stop-holes at the portions of the graph near the crack tip. A higher crack propagation velocity indicates that the crack experiences a time-dependent acceleration between the adjacent time-steps due to the presence of the nearby holes. In fact, the presence of a hole in a body has two major effects on crack dynamics: (1) the accelerating effect, and (2) arresting effect. When a crack gets close enough to a hole, it tends to run towards the hole with a continuously growing velocity until it joins the hole. This can be referred to as the "accelerating effect". Once the crack joins a hole, it relaxes for a while by releasing its accumulated energy. This relaxation causes a decrease in the average propagation velocity of the crack, which can be referred to as the "arresting effect". The accelerating and arresting effects of stop-holes can be seen between 400^{th} and 550^{th} time-steps for the No-hole, Bi-hole and Parabolic geometries in Fig.3.9b. The holes are located $1mm$ ahead of the crack tip in Bi-hole geometry, which affects the crack in this region to accelerate towards the hole for the $1mm$ distance. Hence, in this region the crack propagation velocity of Bi-hole geometry is higher than the one encountered in No-hole geometry. On the other hand, in Parabolic geometry the first two holes are adjacent to the crack tip, which allows no distance for the crack to accelerate. Therefore, only the arresting effect of the holes exists in this region, causing a decrease in average velocity of the crack propagation.

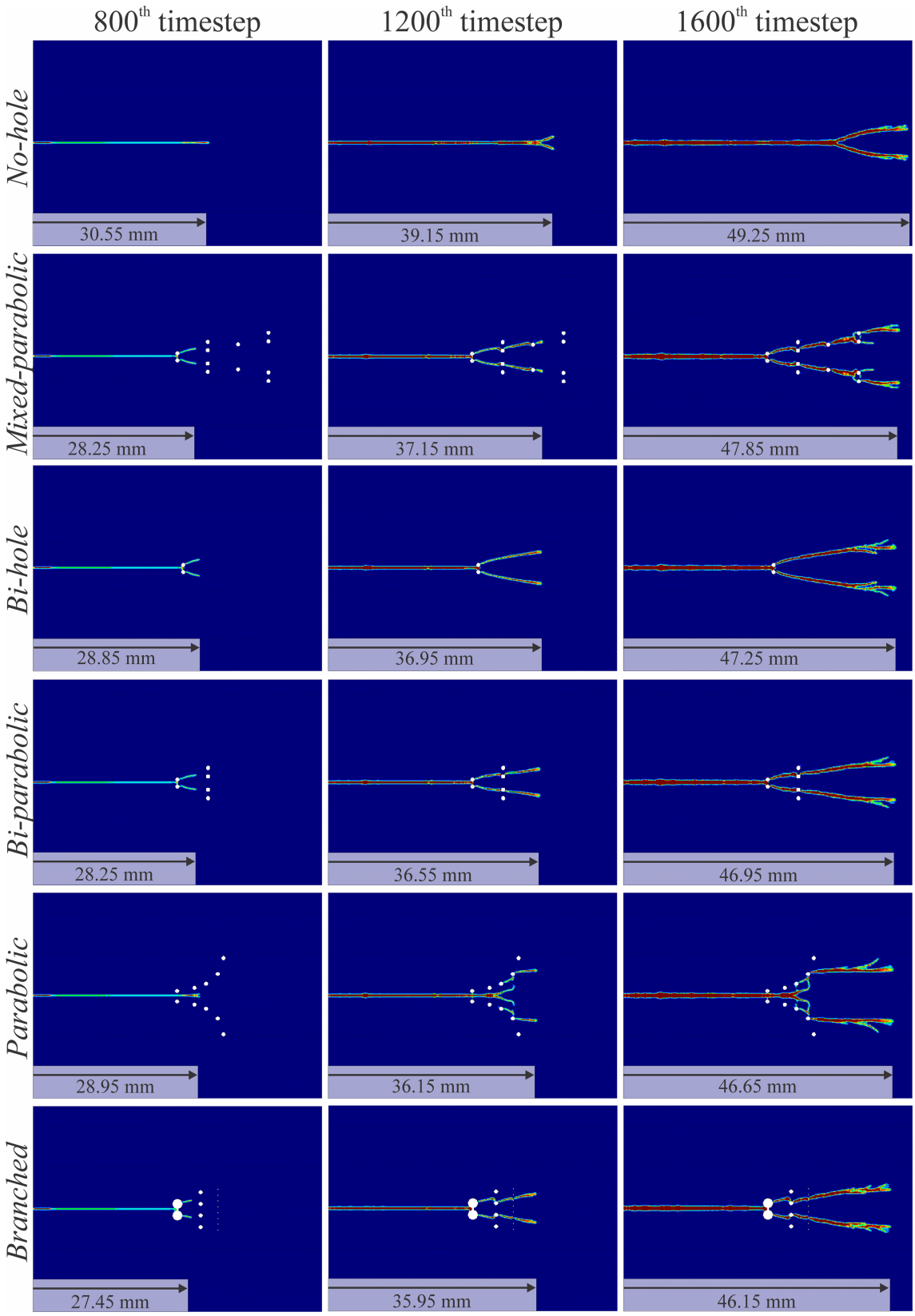

Figure 3.10: Crack length and branching effects of the geometries under tensile loading after 800^{th}, 1200^{th} and 1600^{th} timesteps

Fig.3.10 shows the evolution and the length of the cracks along with the branching effects at 800^{th}, 1200^{th} and 1600^{th} time-steps for the listed geometries. The geometries are

zoomed into the failure zone, given that no failure has been detected in other regions of the plate. As is seen, stop-holes can also affect the propagation angle of the cracks located in its neighborhood. This effect is extremely seen in the case of parabolic geometry, in which the crack has propagated towards the fourth hole with an angle of almost 90^o, while the rest of the crack propagation is almost horizontal. Furthermore, the Branched combination of stop-holes, so far, has proven to have the highest impact on material toughness (Table 3.3). Although the average propagation velocity between 800^{th} and 1600^{th} time-steps of the Branched combination is the same with the one in No-hole combination, the branched combination has a higher effect on delaying the initiation time of crack propagation (almost 50%). This effect is the opposite in Bi-hole and relatively lower in Bi-parabolic and Mixed-parabolic combinations. In the Bi-hole geometry, despite its earlier initiation time, the average velocity of the crack propagation is much lower than that of No-hole geometry, leading to a high toughening effect. On the other hand, Mixed-parabolic combination causes a relatively higher average propagation velocity between the previously mentioned time-steps. However, the total arresting effects in this geometry is higher than the total accelerating effects, which literally causes an increase in material toughness. Moreover, the parabolic combination results in a relatively higher delay in initiation time of the crack propagation and causes the lowest crack propagation velocity, leading to a second-high toughening effect. Nevertheless, the precise implementation of

Table 3.3: Summary of the crack dynamics of the geometries under tensile loading

	No-hole	Mixed-parabolic	Bi-hole	Bi-parabolic	Parabolic	Branched
Crack propagation initiation time-step	480	580	450	580	540	720
X-coordinate of the crack tip at 800^{th} time-step [mm]	5.55	3.25	3.85	3.25	3.95	2.45
X-coordinate of the crack tip at 1600^{th} time-step [mm]	24.25	22.85	22.25	21.95	21.65	21.15
Average velocity between 800^{th} and 1600^{th} steps [mm/step]	24.25	22.85	22.25	21.95	21.65	21.15
Difference in average velocity with respect to No-hole	-	4.81%	−1.60%	0.0%	−5.35%	0.0%
Delay in crack initiation time with respect to No-hole	-	20.8%	−6.25%	20.8%	12.5%	50.00%
Difference in crack length after 1600 steps	-	−5.8%	−8.3%	−9.5%	−10.7%	−12.8%

Table 3.4: Comparison of the geometries under tensile loading

	Reproducibility	Material Cost	Toughness Enhancement
No-hole	★★★★★	★★★★★	
Mixed-parabolic	★★	★★	★★
Bi-hole	★★★★	★★★★	★★★
Bi-parabolic	★★★★	★★★	★★★
Parabolic	★	★★	★★★★
Branched	★★★	★	★★★★★

this geometry can be challenging. On the other hand, the branched geometry is much easier to implement. In summary, it can be stated that the Branched geometry has the highest effect on material toughness and the lowest material cost with an average rate of reproducibility (Table 3.4).

3.3.4. Stop-hole combinations under shear loading

In this section, a plate of dimensions $50mm\,x\,50mm$ is analyzed under velocity shear loading of $5\,m/s$ at the upper boundary, while the lower boundary is fixed. The material properties of the plates are same as the ones used in the previous case. A pre-existing crack with the length of $L/4$ ($12.5\,mm$) is located at the central left portion of the plate, as shown in Fig.3.11. For all the analyses carried out in this section the time step size is taken as $dt = 1.064e^{-7}s$ which is the stable time step size calculated from Eq.(2.25). The breakage of the bonds is permitted under both tension and compression conditions with the equal magnitude of the critical stretches. To account for total failure of the body, we consider the crack propagation lengths in both x- and y-directions. The contours of the displacements and failure are shown in Fig.3.12 for No-hole geometry after 1350 time-steps. Two new crack branches are formed in the body during the loading process, namely the lower and upper branches (Fig.3.12a). The lower crack branch is due to the internal tensile force caused by the boundary condition, whereas the upper crack branch is formed because of the compression effect of the loading on upper portion of the plate. The crack propagations in No-hole, T-shaped, I-shaped, Bi-linear, Linear and Linear-parabolic geometries are shown in Fig.3.13. In order to have a reference failure state for toughness enhancement comparison, we define two different failure scale parameters: (1) total split length of material and (2) total failure length of material. To measure the total split length, the length of the split surface between different parts of plate is considered. Herein, this includes the length of the propagated crack as well as any other defect where the split surface passes through (e.g., the length of the first three upper holes in Linear and Linear-

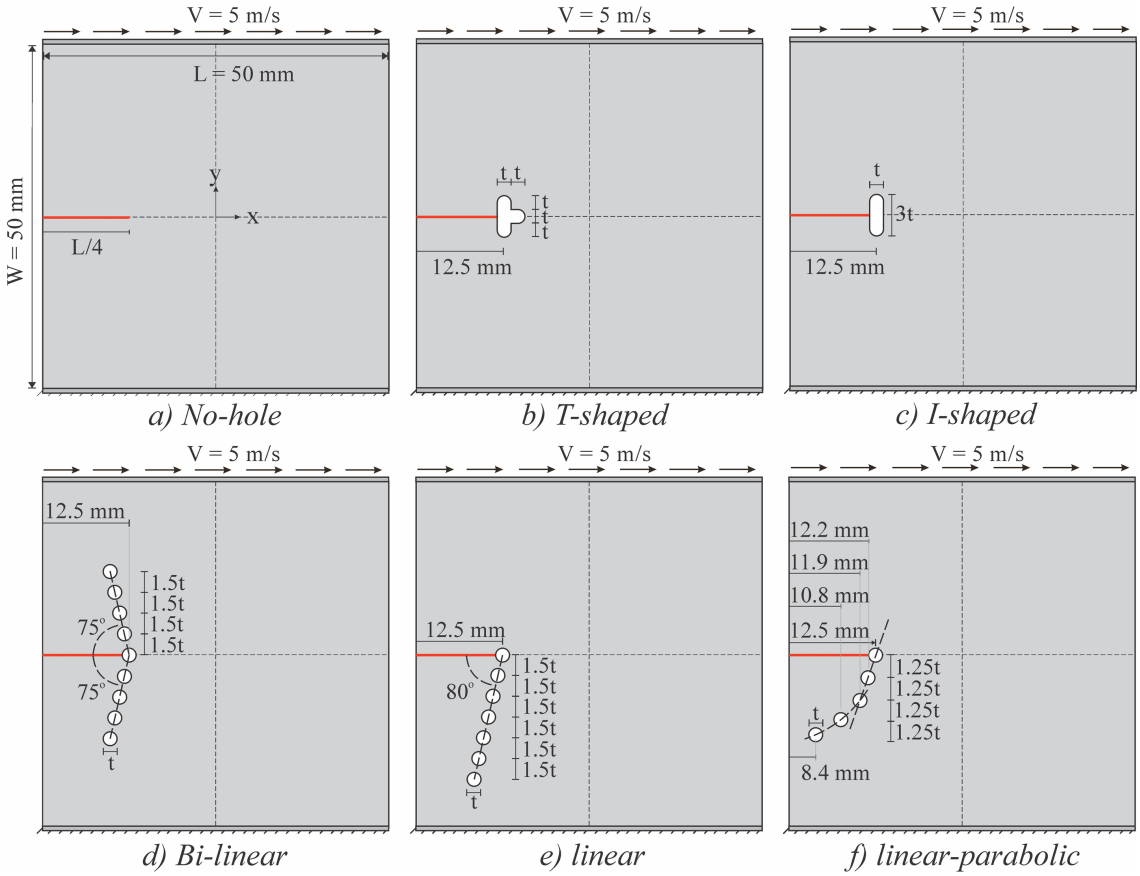

Figure 3.11: Geometric properties of the plates under shear boundary condition, with $t = 2mm$

parabolic geometries). In other words, a total split length can be considered as a measure of the global failure of a material for which all defects existing in the body are taken into account. On the other hand, a total failure length can be considered as the total length of the surface where the bonds between material points has failed due to exceeding the critical stretch (i.e. local failure). The variation of the above failure parameters against every incremental 50 time-steps are plotted in Fig.3.14 for each geometry. A summary of the crack dynamics in the above geometries is also given in Table 3.5, from which it

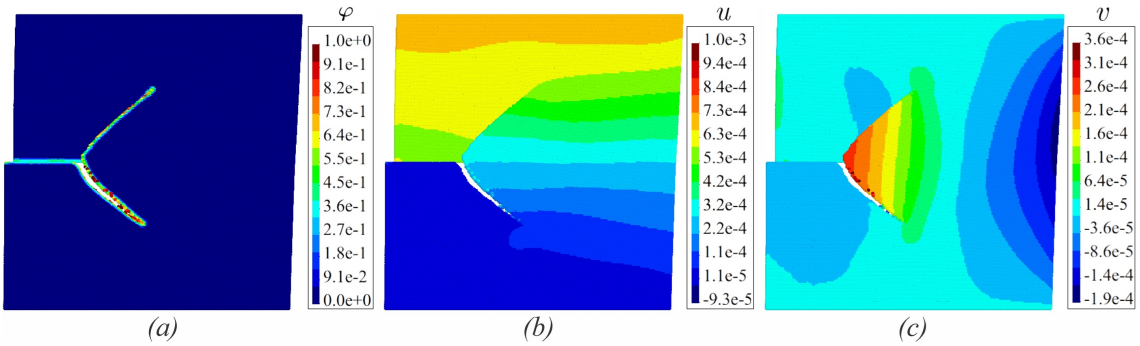

Figure 3.12: Counter-plot of a) damage, b) displacement in x-direction [m] and c) displacement in y-direction [m] of No-hole geometry at 1350^{th} time-step

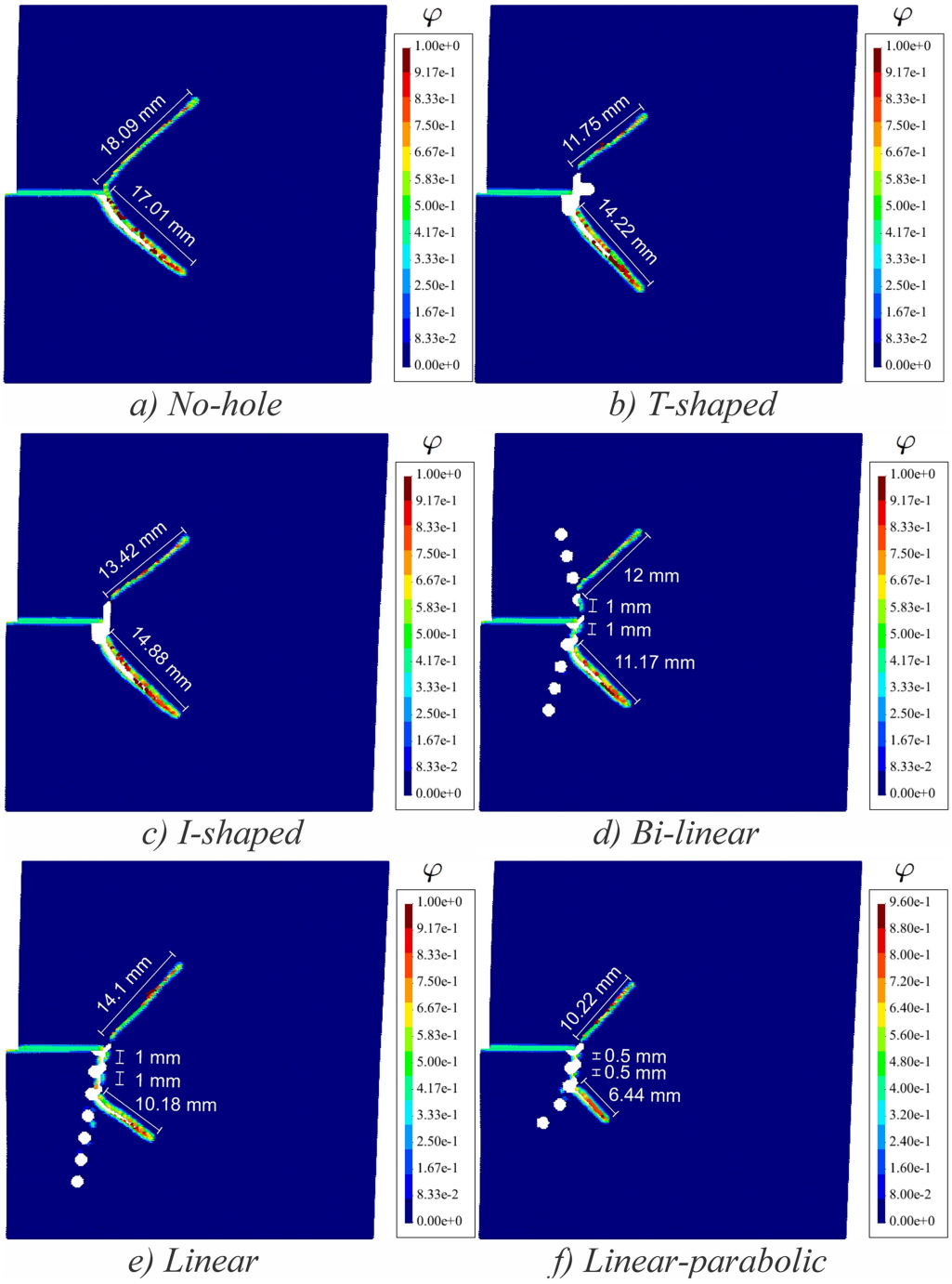

Figure 3.13: Crack surface and propagation length of the geometries under shear loading at 1350^{th} time-step

can be seen that all the listed geometries have caused a significant amount of increase in the strength of the material. This toughening effect can be seen in the shape of a decrease in the average propagation velocity and/or a delay in the propagation initiation time. It is worthy to notice that almost every linear combinations of the circular stop-holes have a decreasing effect on the average velocity of the propagation, eventually causing a relatively higher toughness enhancement. However, the toughness enhancement in the T-shaped and I-shaped geometries are largely seen in the form of the delay in initiation time

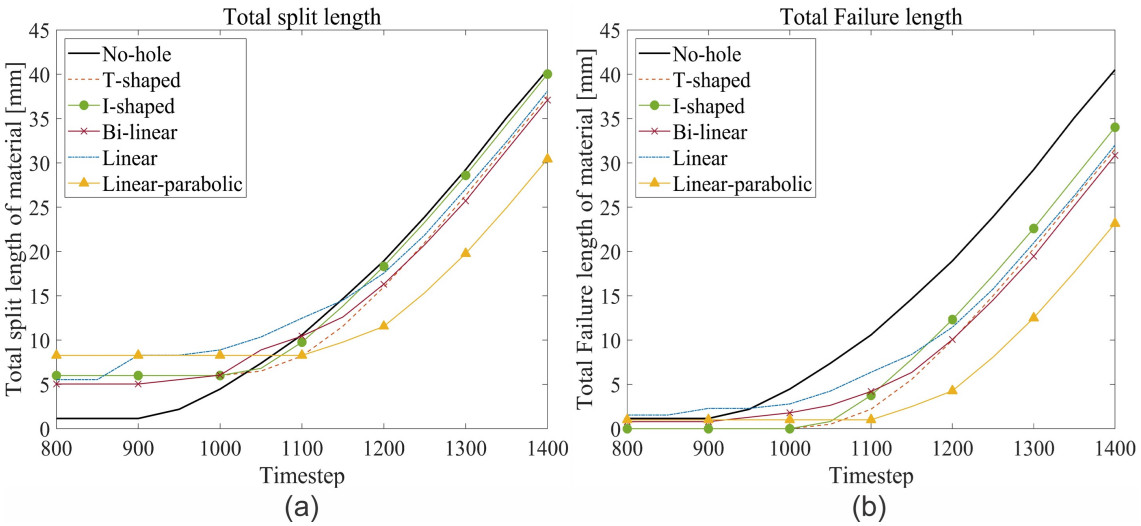

Figure 3.14: Graphs of a) total split length and b) total failure length of material vs time-step for the geometries under shear loading

of the propagation. The toughening effect is the highest in Linear-parabolic combination due to the presence of both of the situations mentioned above. Furthermore, the Bi-linear combination of stop-holes causes the highest decrease in material cost, with a second-high toughening effect. In fact, the implementation of the Bi-linear combination of stop-holes is more economic and much easier than that of the Linear-parabolic combination, as seen in Table 3.6.

Table 3.5: Summary of the crack dynamics in geometries under shear loading

	No-hole	T-shaped	I-shaped	Bi-linear	Linear	Linear-parabolic
Crack initiation time-step	950	1050	1050	950	850	1100
Total split at initiation time-step [mm]	2.19	6.5	6.81	5.54	5.54	8.27
Total split at 1400^{th} time-step [mm]	40.05	37.53	40.014	37.086	38.101	30.428
Average velocity of the propagation [mm/step]	0.0841	0.0887	0.0949	0.0701	0.0592	0.0739
Delay in crack initiation	-	10.5%	10.5%	0.0%	−10.5%	15.8%
Difference in average velocity	-	5.4%	12.8%	−16.7%	−29.6%	−12.2%
Difference in crack length after 1400 steps	-	−6.3%	−0.1%	−7.4%	−4.9%	−24.0%

Table 3.6: Comparison of the geometries under shear loading

	Reproducibility	Material Cost	Toughness Enhancement
No-hole	★★★★★	★★★★★	
I-shaped	★★★★	★★☆	★
Linear	★★★	★☆	★★
T-shaped	★★★☆	★★	★★☆
Bi-Linear	★★☆	★	★★★
Linear-parabolic	★	★★	★★★★★

3.3.5. Effects of the distance of stop-holes from the crack-tip on crack dynamics

In this section, the effect of the distance of stop-holes from the crack tip is investigated under the tensile loading. For this purpose, a plate with $LxW = 50mmx25mm$ dimensions having a pre-existing crack with a length of $L/5$ $(10\,mm)$ located at its central left part is analyzed. The material properties of the plate are given in Table 3.1. The distance between material points, dx, is taken as $0.25\,mm$. The plate is subjected to a uni-axial velocity boundary condition of $+150\,mm/s$ and $-150\,mm/s$ at its upper and lower boundaries, respectively. As a first approach, a circular hole of diameter $D = 2\,mm$ is applied to the plate at a distance of d from the crack tip (Fig.3.15a). Eq.(2.25) is used to ensure a time-step size smaller than the stable one. Fig.3.16 shows the position of the crack-tip plotted versus every 10 time-steps for various values of d. As is seen, the presence of the hole has caused the crack to have a position dependent velocity. Depending on initial relative position of the crack-tip from the hole, the average propagation velocity of the crack can either be increasing, decreasing or constant. A singular stop-hole causes a decrease in

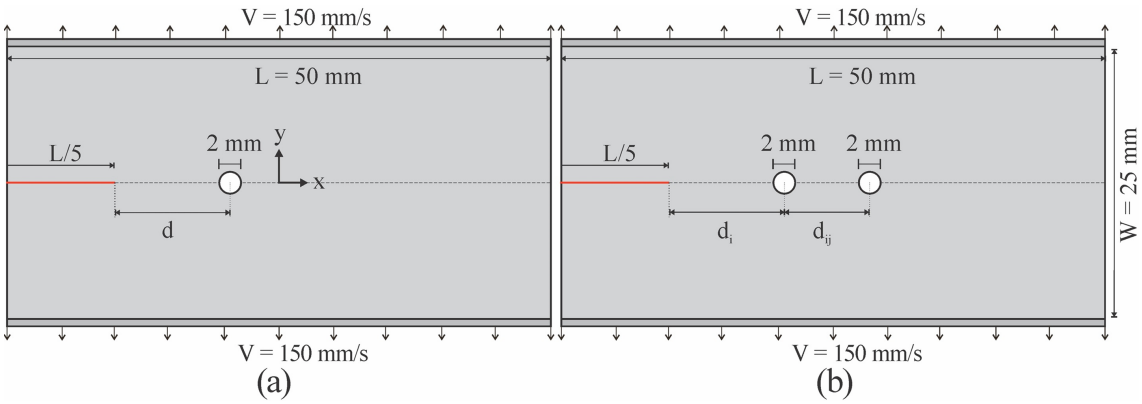

Figure 3.15: Geometric properties of the plate with a) one and b) two holes under uniaxial tension

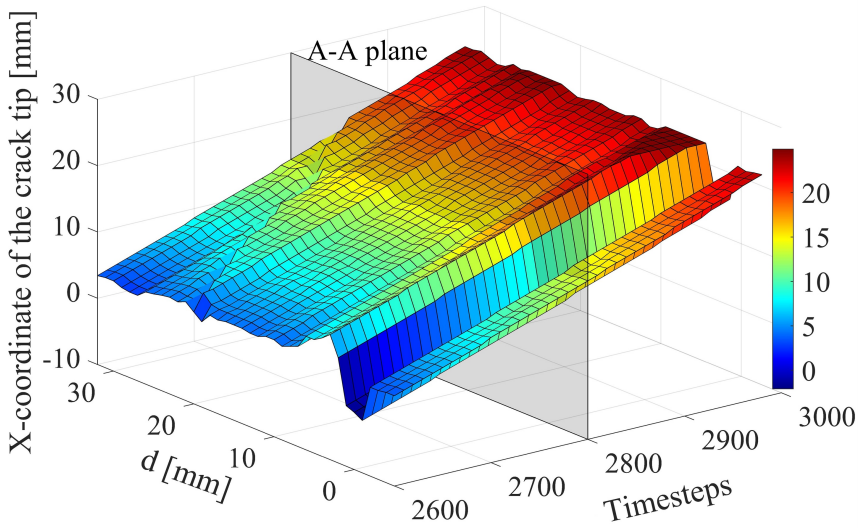

Figure 3.16: Graph of the change in position of the crack tip vs time-step for various values of d for the plate with one hole

average propagation velocity of the crack if it is implemented to the material in such a way that the relative position of the crack tip falls inside the perimeter of the hole (i.e., $|d| \leq D/2$). This effect is the highest when the hole is located ahead of the crack at the exact tangency of the crack tip (i.e., $d = -D/2$). However, when the distance between the hole and the initial crack tip gets higher (i.e., $d \geq D/2$), the hole affects the material toughness in a negative manner by increasing the average crack propagation velocity. Interestingly, this effect is recorded as a decreasing function of d after a certain distance (e.g. $d \approx 2D$ for the present case). Thus, it can be concluded that a certain constant influence range of μ exists for a hole such that; whenever a crack enters the μ-range it

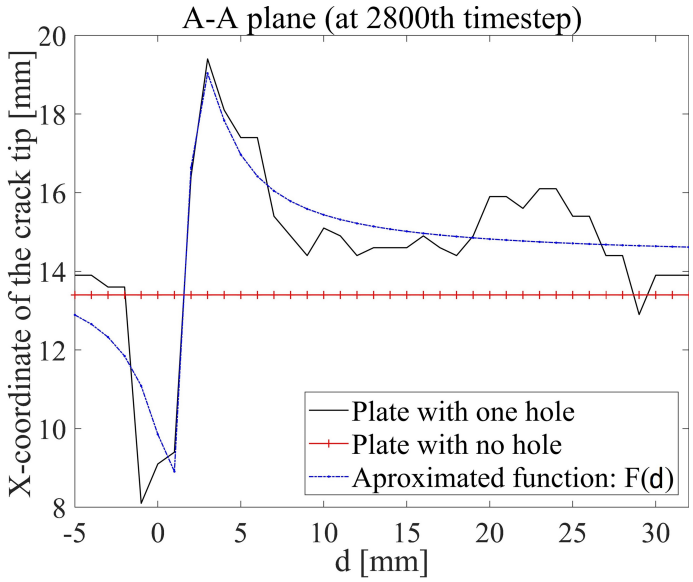

Figure 3.17: The graph of the change in position of the crack tip at 2800^{th} time-step vs d for the plate with one hole

accelerates whereas for any distance beyond this range, the effect of the hole on crack dynamics is zero. The position of the crack-tip with respect to d (plotted in Fig.3.17 as two-dimensional graph) can be approximated through the curve fitting with a function of:

$$F(d) = \frac{14.3d^2 - 39.73d + 37.68}{d^2 - 3.448d + 3.823} \tag{3.1}$$

where $F(d)$ denotes the position of the crack tip at an instant of time (2800^{th} time-step in the present case). If the distance, d, is significantly large, i.e., $d \to \infty$, the function approaches to the constant value of $F(d) = 14.3\,[mm]$. This reveals the fact that if the hole is located far enough from the crack tip, the hole, independent from its position, will accelerate the crack for a constant distance if and only if the crack enters the μ-range. This distance can be related with the μ-acceleration as follows:

$$14.3 - X_c = \frac{1}{2} a_\mu t_\mu^2 \tag{3.2}$$

where X_c is the position of crack tip at the same instant of time for the situation in which no stop-hole exists in the body ($13.44\,mm$ for the present case). The parameters a_μ and t_μ are so-called the μ-acceleration (the acceleration caused by the hole) and μ-time (the time interval of μ-acceleration), respectively. Hence, the $F(d)$ function may be used to measure the amount of the accelerating effect of the stop-holes on crack propagations.

The crack dynamics may also be altered by the number of holes in the body. In order to have a better insight on such effects, a second stop-hole is placed at a distance of d_{ij} from the first hole (Figure 18b). For this purpose, a rupture corresponding to 80% of the plate (equivalently, the crack tip reaches the coordinate of $x = 15$ mm) is taken as the basis of comparison. Fig.3.18 clearly indicates that the toughening effect is the highest for the values of $d_i \in [0-1mm]$ and $d_{ij} \in [0-1mm]$. Furthermore, for the higher values of d_i and d_{ij} a decrease in the strength of the material is observed. This weakening effect, however, approaches a constant value when d_i and d_{ij} get larger. Additionally a strengthening effect from the small values of d_i and an abating weakening effect from the high values of $d_{ij} \in [4-10mm]$ is clearly noticeable in Fig.3.19, hence leading to a higher toughness. This also indicates that the toughening effect of a hole placed near the crack tip is much higher than the weakening effect of a hole located in far-hand regions. On the other hand, for larger values of d_i, the variation of d_{ij} has a very low impact on the strength of the material. This well agrees with our previous findings on the μ-ranges of stop-holes where it was stated that for any large value of d, any stop-hole regardless of the distance d will accelerate the crack propagation for a constant distance. It should be noted that the above conclusions were made only by taking into account the horizontal relative positions of the initial crack-tip and holes. A more detailed study should be carried out as the crack dynamics is not only affected by the horizontal distance of the holes but also the vertical

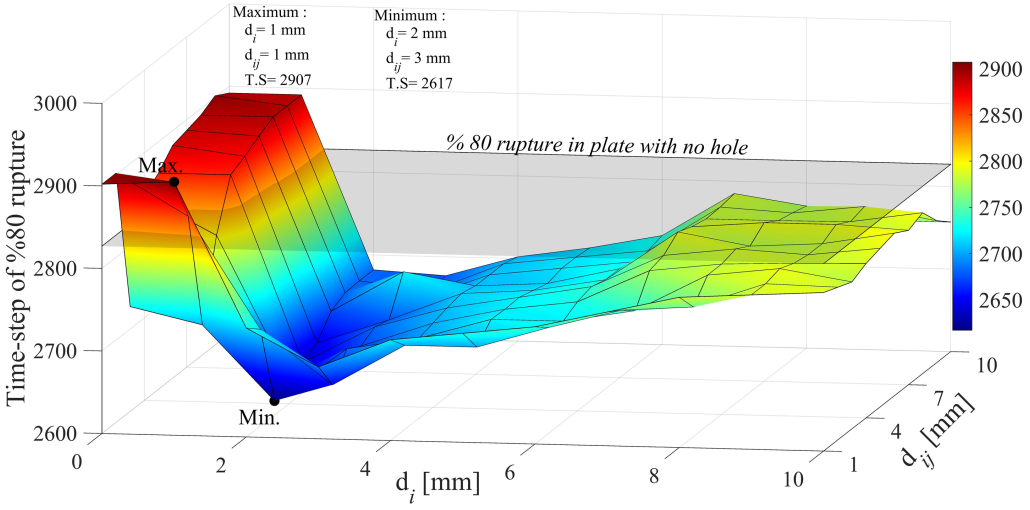

Figure 3.18: Graph of the change in time-steps of the 80% rapture of the plate with two holes vs di and d_{ij}

distance and the diameter, D, of the holes as well as the initial pre-existing crack length, which are beyond the extents of this paper.

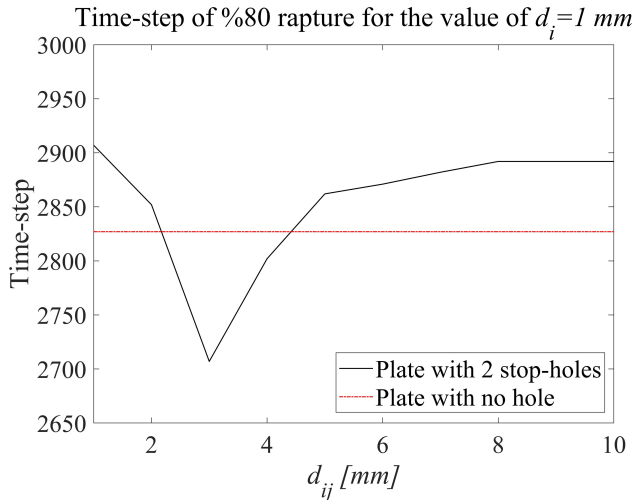

Figure 3.19: The variation of the time-step of the 80% rupture vs d_{ij} of the plate with two stop-holes

3.4. Conclusions

In the scope of this study, the effects of various linear/non-linear combinations of stop-holes on toughness enhancement in brittle materials are investigated under tensile and shear loadings by performing traditional ordinary state-based peridynamic (OSB-PD) analyses. The numerical algorithm is assessed by solving benchmark cases with various fracture modes while comparing the results with the experimental-numerical finding of literature. It is demonstrated the OSB-PD can predict very similar final fracture patterns

observed in the experiments for mode-I, mode-II, and mixed mode I-II loading conditions. Additionally, the accuracy of present approach is further validated with respect to experiments and dynamic phase-field method for crack propagations in porous media. The OSB-PD is shown to produce superior final fracture pattern than that of phase-field method. Furthermore, Broek ([13]) and Miyagawa et al. ([14]) reported in their experimental studies that a crack is attracted towards any nearby hole in a porous media. This important physical phenomenon is accurately captured by our numerical implementations.

Having validated the proposed algorithm and its numerical implementation on various challenging problems, we have studied further complex problems that involves various stop-holes combinations for toughness enhancement under tensile and shear loadings. The toughening effects of the proposed stop-hole configurations are evaluated referring to the total split and failure lengths. These stop-holes combinations are shown to be highly effective in decreasing the total split lengths, the total failure lengths and the average propagation velocity of the cracks, hence increasing the material toughness. The effect of the distance of multiple stop-holes from the crack tip is also investigated. It is observed that every stop-hole has an influence domain (i.e., the μ-range) beyond which the crack dynamics is not significantly affected. It is shown that when the stop-hole intercepts the crack-tip, the material toughening is maximized. On the other hand, if the stop-hole is located in the far field from the crack tip, the material toughness decreases. Additionally, it is concluded from the analysis with two stop-holes that the toughening effect is maximized when both of the stop-holes are placed near the crack tip. Which elaborates that depending on the distance between the holes, the material toughness can be tailored. Finally, the influence of drilling stop-holes on labour and material cost is also compared for different stop-hole configurations, which can provide valuable information for addressing time-cost-trade off problems

4

An Improved Peridynamic Formulation for Modeling FGMs with Sharp Interface Transitions

Mohammad Naqib Rahimi, Adnan Kefal, Mehmet Yildiz

Submitted to: International Journal of Mechanical Sciences

4.1. Abstract

This study proposes an enhanced formulation of Ordinary-State based peridynamic which can model functionally graded materials (FGMs) with sharps jumps in material properties through introducing a novel peridynamic parameter, referred to as the dominancy rate. The current formulation takes into account the multi-scale nature of peridynamics as well as the material transition (interface) effects. As a result of extensive comparison efforts with FEM literature, traditional peridynamics, and ANSYS, this study reveals that the properties of a PD-bond should not be equally affected by the properties of the constituent points in modeling FGMs. Additionally, it is found that the correctness of the results is negatively influenced if the bond properties are determined using only one of the weaker or stronger constituent point. Furthermore, a better accuracy is achieved, specially at the material transition regions, through considering that the properties of the bonds are mostly dependent on that of the weaker constituent point. To demonstrate the capability of the proposed model, a numerically validated toughening mechanism against crack propagations is presented for FGMs. It is found that the local toughness of FGMs can be effectively enhanced by tailoring the location and material properties of the sub-regions.

Keywords: Ordinary State-Based Peridynamics, Functionally graded materials, High gradients, Material transitions, Interface modeling, Toughness enhancement.

4.2. Introduction

In many engineering problems one may come across to situations in which incongruous properties of materials are needed. For example, in most of the machinery and automobile industries, a part is needed to be ductile as well as hard. The other desired material attribute is of course the minimal weight. As traditional engineering materials fail to exhibit such combined behaviors [49–51], Functionally Graded Materials (FGMs) have been developed. Unlike conventional composites, in FGMs, the properties of the constituent materials vary smoothly and continuously thereby circumventing the sharp interfaces between the layers which might lead to delamination failure [52]. Moreover, the smooth variation of the properties in FGMs play an important role in preventing stress singularities and reducing residual stresses at material interfaces. Such characteristics of FGMs attracted an uncommon interest of researchers in a short period of time [53–56] and widened the usage of FGMs to many engineering and medical fields [57–60]. The experimental works on mechanical and thermomechanical properties of FGMs have fairly been widened. Much works were carried out investigating the optimum material compositions [57, 58, 61], thermal and mechanical residual stresses [55, 62] and fracture mechanics [63, 64] of FGMs. Although these works form the fundamental knowledge to generalize specific properties, it is practically impossible to experimentally identify which variable dominates the overall properties of interest, given that there are quite many parameters interrelated to each other. This basically requires additional data generation that can easily be handled by both modeling and numerical perspectives. There an obvious increasing trend in modeling FGMs is seen within the past few decades. Among the earlier researchers, for example, Fukui et al. [65] numerically and analytically studied the effects of gradation of components on the strength and deformation of FGM tubes under internal pressure. Berezovski et al. [66] and Hedayatrasa et al. [67] investigated the elastic wave propagations in FGMs using different finite element approaches. One other most significant discussion in FGMs is the fracture occurrences, which has extensively been studied through the years.

Numerical modeling of imperfection formations (e.g., cracks, damage, holes, material interfaces) in FGMs are quite challenging due to the non-symmetrical property variations. This has been an object of researches since the 1980s [68]. Studies have indicated that the stress field of the crack tip is mostly influenced by the inverse-square-root-singularities, in which the elastic variation has a significant role while the role of Poisson's ratio is negligible [69]. Therefore, in complex medias such as FGMs, the variation of elastic modulus may result in complicated damage propagations. Moreover, in FGMs in situations where the crack is not parallel to the gradient direction or the circumstances where the loading is not symmetrically applied with respect to the crack surface, a mixed-mode fracture oc-

curs. There have been quite valuable efforts on modeling such fracture occurrences of complex nature. To name a few, Kirugulige et al. experimentally [70] and numerically [71] investigated this type of crack propagations under dynamic loadings by utilizing cohesive zone finite element method. Abotula et al. [72] used asymptotic approach to model the stress field at the crack-tip. Hirshikesh et al. [73] and Doan et al. [74] modeled the dynamic crack propagations by utilizing various Phase Field methods. As is seen, most of the efforts regarding the wave and fracture modeling in FGMs are carried out using the traditional methods based on classical continuum mechanics formulations (CCM). Only recently, Chen et al. [34] and Ozdemir et al. [35], in turn, proposed a Bond-Based (BB-PD) and Ordinary State-Based Peridynamic (OSB-PD) models for simulating dynamic crack propagations in FGMs. But yet, due to the assumptions in driving the bond properties, these models fail to address the material transitions, interfaces, and multi-scale effects.

Hence, by introducing a novel PD parameter, the *dominancy rate* (ψ), we propose an improved formulation of PD for FGMs to account for transition and interface effects. We systematically evaluate the proposed model for the behavior of FGMs under wave propagations, static loadings, and dynamic fractures. Moreover, as an application of the present formulation, we present a novel numerical toughening model to enhance the properties of FGMs against crack propagations. Even though, there a wide range of numerical toughening models exist for different material types, to the best of authors' knowledge, no study has been dedicated to the numerical toughening mechanisms of FGMs. Recently, a similar model was proposed by authors [75] in which stop-holes were implemented to plates in order to increase the toughness of isotropic materials. Herein, the model is further developed for FGMs by introducing homogeneous and flipped sub-regions consisting of slightly or highly different material properties. With the help of the recent developments in the area of additive manufacturing [76], the proposed toughening model in this effort may be useful to further enhance the FGM capabilities against crack propagations by employing considerably negligible changes to the geometry.

4.3. Numerical Examples

4.3.1. Mixed-Mode Dynamic Crack Propagations in FGMs Under Three-Point Bending

The OSB-PD model proposed in this study is validated through revisiting the complex benchmark problem solved in [70], which involves the mixed-mode damage occurrence. A plate with the length $L = 152\,mm$, and width $W = 43\,mm$, given in Fig.4.1, is subjected to three-point bending stress of $\sigma_0 = 25\,MPa$ with a rump-up and rump-down time of $30\,\mu s$ and a total loading duration of $200\,\mu s$ (Fig.4.2). The load is applied asymmetrical to crack surface to ensure a mixed-mode damage propagation. Since the experimental loading profile is not provided in Ref. [70], the loading conditions used in this test case is given in Fig.4.2 in accordance with Refs.[34, 35, 74]. Two different scenarios are considered: 1) the plate with the pre-existing crack length of $a = 8.6\,mm$ located on the stiff side, and 2) the plate with the pre-existing crack of the same length located on the

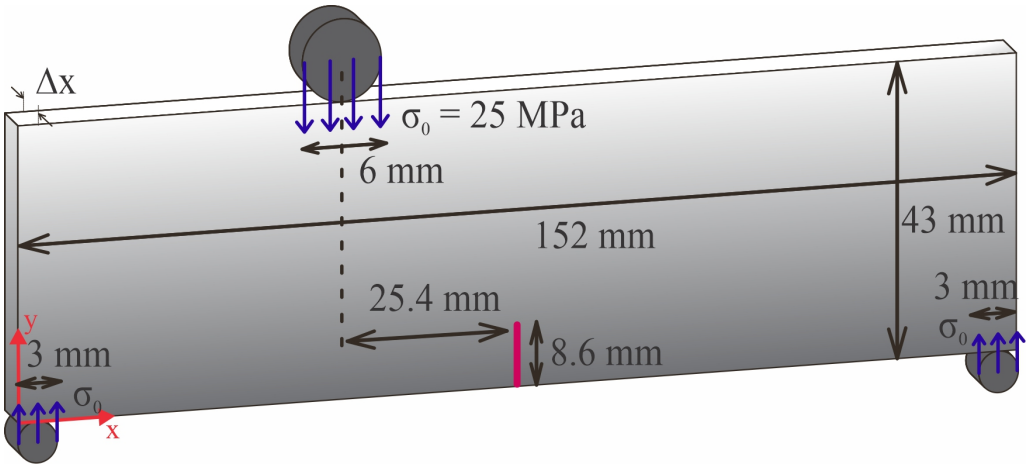

(a) Crack located on the stiff side

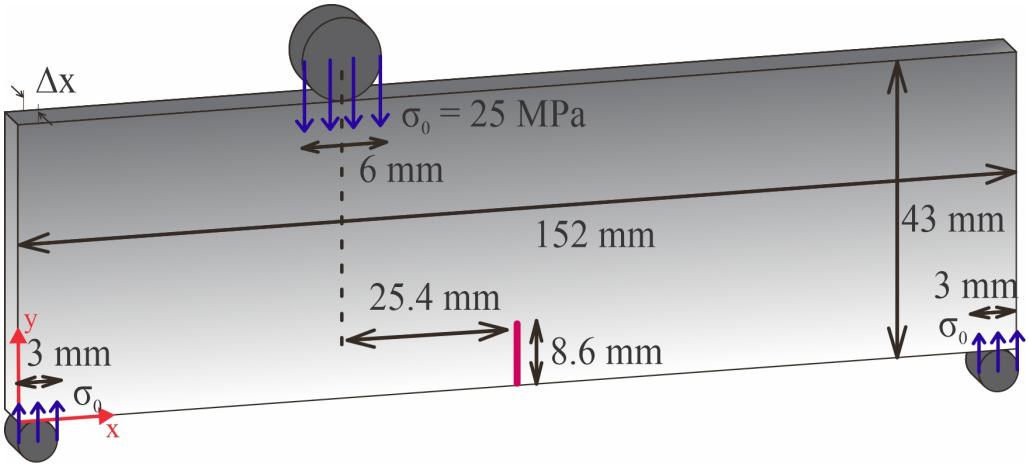

(b) Crack located on the compliant side

Figure 4.1: Geometric properties of FGM plates under three-point bending test

Table 4.1: Material properties of the plate under three-point bending test

Elastic Modulus	Density	Poisson's ratio	KIc
Best fit (Fig.4.3)	Best fit (Fig.4.3)	$0.33+0.000465y$	$2.2-0.0186y$

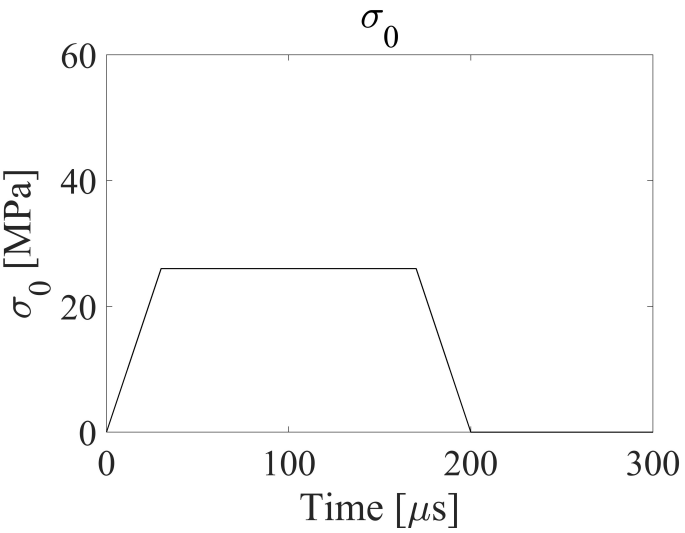

Figure 4.2: Rump-up-down loading profile of the plate under three-point bending test

compliant side. The material properties of the plate (given in Table 4.1 and Fig.4.3) are obtained by digitizing the experimental data in Ref.[70]. The plates are discretized into $152x43$ points with a material point spacing of $\Delta x = 1\,mm$ and horizon size of $\delta = 3\Delta x$. The incremental time-step size is taken as $dt = 20\,ns$ which is selected in accordance with the stability condition (Eq.2.25). The analyses were explicitly carried out for a total time of $300\,\mu s$.

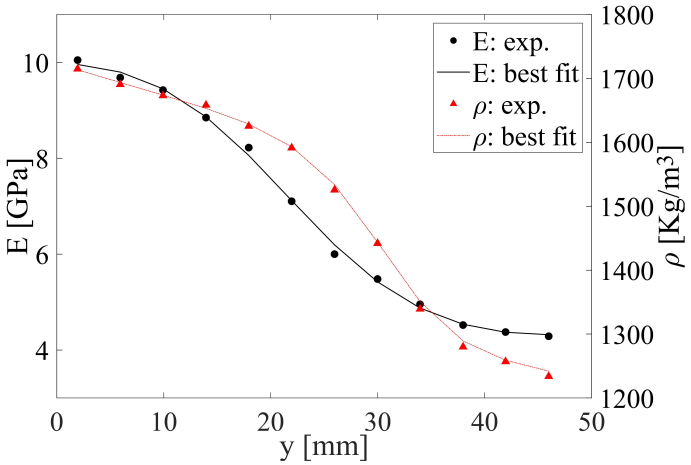

Figure 4.3: Elastic modulus and density variation of the FGM plate under three-point bending test

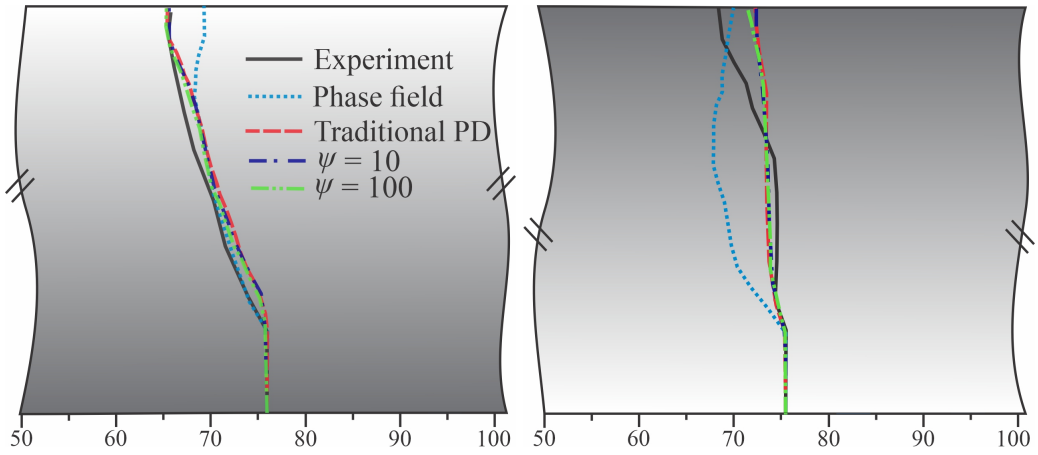

(a) Crack located on the stiff side (b) Crack located on the compliant side

Figure 4.4: A comparison of the final crack path in plates under three-point bending with the experimental [70] and Phase field [74] results

Fig.4.4 shows a comparison of the final crack path obtained by the OSB-PD analyses with the ones of experiments [70] and Phase Field model [74]. As seen in Fig.4.4a, in the plate with crack located on the stiff side, the OSB-PD approach successfully predicts the experimentally observed behavior of the crack with negligible fluctuations. It is observed that these fluctuations become larger in the plate with crack located on the compliant side (Fig.4.4b). This can be attributed to the missing experimental loading profile as well as the different support conditions assumed in the analyses stage. In the experimental configuration, the beam is supported by two blocks of soft putty while the simulations are conducted under free-free end boundary conditions, thereby preventing the support reactions, which are known to have an important effect on fracture behavior [70, 74]. The accuracy of the proposed OSB-PD model in predicting the crack path can be seen for both configurations, the plate with the crack located on stiff side and the plate with crack located on compliant side. The analyses are carried out for different values of the dominancy rate, ψ. However, the ψ values are observed not to change the final results. This is due to the smoothness of FGM properties between the neighboring points. Because of the small material gradient in a given horizon (i.e., $\delta = 3mm$), different values of ψ result in approximately the same inter-family bond properties. Thus, in order to see effects of ψ on the results, a high material gradient or a sudden change (jump) in the material properties between the neighboring points should exist. Therefor, in the proceeding case study, we will investigate the effects of ψ on FGMs by introducing a region with notably different material properties, referred to as the sub-regions.

4.3.2. Wave propagations in FGMs of high gradient

The original form of this problem was firstly solved in [66] and reproduced in [34, 35, 67, 77] for the FGM plate with dimensions $L = 49mm$ and $W = 24.5mm$ ($200x100$

points). The upper portion of the plate is consisted of ceramic (alumina) with high elasticity (named as Phase 1) while the lower portion is made of metal (aluminum) (named as Phase 2). Three different material gradients were considered, namely, Case A, C and D, utilizing the gradient function $F = F^0(y/W)^d$. In which y and W is the vertical position of the point and width of the plates, respectively. In Case A, the value of F^0 and d are in turn taken as 0.36 and 0, which result in a plate with homogeneous properties. The value of F^0 in Case C and D is taken as 0.6 with d being equal to 0.25 and 4, in the given order. Such a setting leads to a low material gradient for Case C and slightly higher material gradient for Case D. The effective material properties, P_{eff}, for any point in FGM region are then calculated as:

$$P_{eff} = P_{phase1}F + P_{phase2}(1-F) \tag{4.1}$$

In all of the above cases, the change in the material properties between the neighboring points is considerably small to observe the effects of ψ on the solution. Thus, to bet-

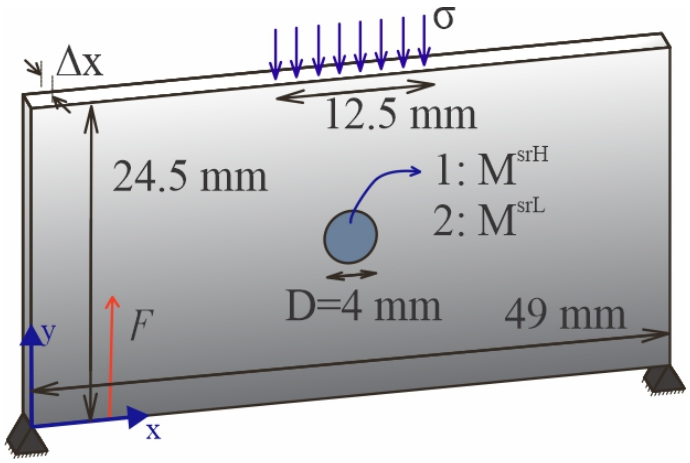

(a) Geometry S (smaller subregion)

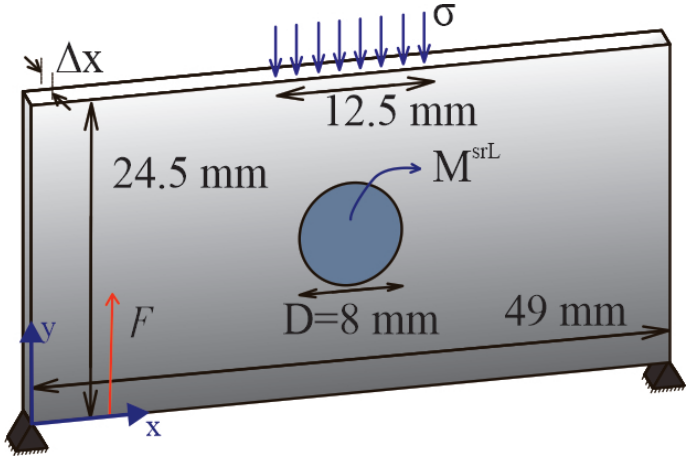

(b) Geometry L (larger subregion)

Figure 4.5: Geometric properties of FGM plates under sinusoidal impact loading

Table 4.2: Material properties of the plate under three-point bending test

	Phase 1 (top) Ceramic (Alumina)	Phase 2 (bottom) Metal (Aluminum)	M^{srH}	M^{srL}
E[GPa]	420	70	100	10
$\rho[Kg/m^3]$	3200	2800	3000	1200
Poisson's ratio	0.17	0.3	1/3	1/3

ter reveal the capabilities of the current approach, we implemented two different circular sub-regions with diameters of $4\,mm$ (Geometry S) and $8\,mm$ (Geometry L) into the central portion of the original FGM plate, as shown in Fig.4.5. This modification can simply demonstrate the sharp interfaces and can safely represent the effects of material transitions in FGMs with high gradients, given that the FGMs are formed by combinations of small micro-blocks of sub-regions having different material properties. In other words, an FGM plate with a high gradient can be assumed as the set of sub-regions with gradually increasing properties, whereas the material properties may vary significantly. Accordingly, Two different materials are considered for the sub-region in Geometry S, namely, Geometry S1 with M^{srH} and Geometry S2 with M^{srL} properties, whereas due to the expected similar effects, only M^{srL} properties are applied to the sub-region with Geometry L (Table 4.2). All the geometries in this section are subjected to an impact-sinusoidal loading of $\sigma = 125\sin^2(\pi(t-1.5)/1.5)$ which is applied to the $12.5\,mm$ central-upper portion of the plate, while the lower corners are supported in x- and y- directions, as depicted in Fig.4.5. The total loading duration is considered as $1.5\,\mu s$ reaching a peak of $\sigma_p = 125\,MPa$ in $0.75\,\mu s$, as seen in Fig.4.6. The analyses are carried out for $3\,\mu s$ with $dt = 1\,ns$. The effects of ψ are investigated for three different material gradients in three different geometries which in total make nine different scenarios. Among these, the cases of Geometry S2 are the most critical ones with the highest percent differences due to the high change of the material properties in a small region. Hence, for the brevity of the study, the contours of the displacements (Fig.4.7) and percent differences (Fig.4.8) with respect to ANSYS are shown for Geometry S2 only. The percent differences (PE) depicted in Fig.4.8 are calculated as:

$$PE_{(i)} = \frac{|U^{(i)}_{ANS} - U^{(i)}_{PD}|}{U^{max}_{ANS}} \tag{4.2}$$

where U^{max}_{ANS}, $U^{(i)}_{ANS}$, and $U^{(i)}_{PD}$ are maximum displacement of the plate, displacement of point i obtained by ANSYS, and present OSB-PD analysis, respectively.

As can be seen from Fig.4.8, by increasing the values of ψ, the maximum PE in the maximum displacement direction (y-direction) decreases from almost 14% to 6% for the cases A and C, and from 7.5% to 4.8% for Case D. Although the maximum PE is seen to be more than 5% in some cases, such an error stays in an acceptable range considering that the comparison is made between local and non-local continuum methods. It should also be noted that the maximum PE is only seen for a small portion of the plate (5-10 material points) while for the rest the PE is only around 2%. To examine the accuracy of

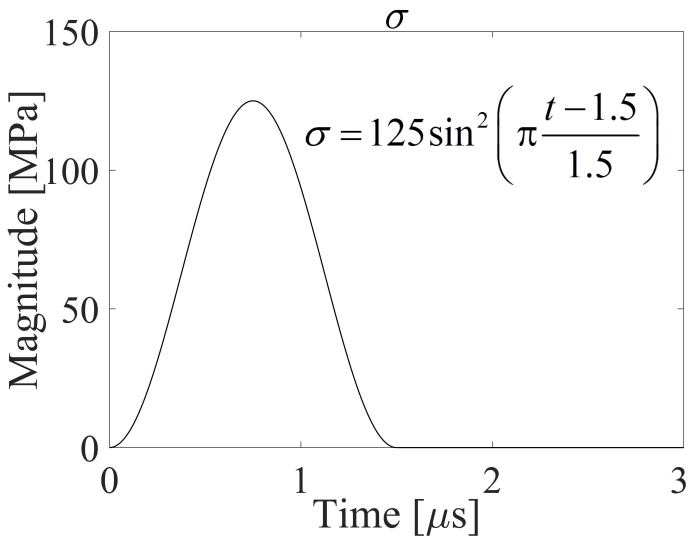

Figure 4.6: Loading profile of the impact on plate with sub-regions

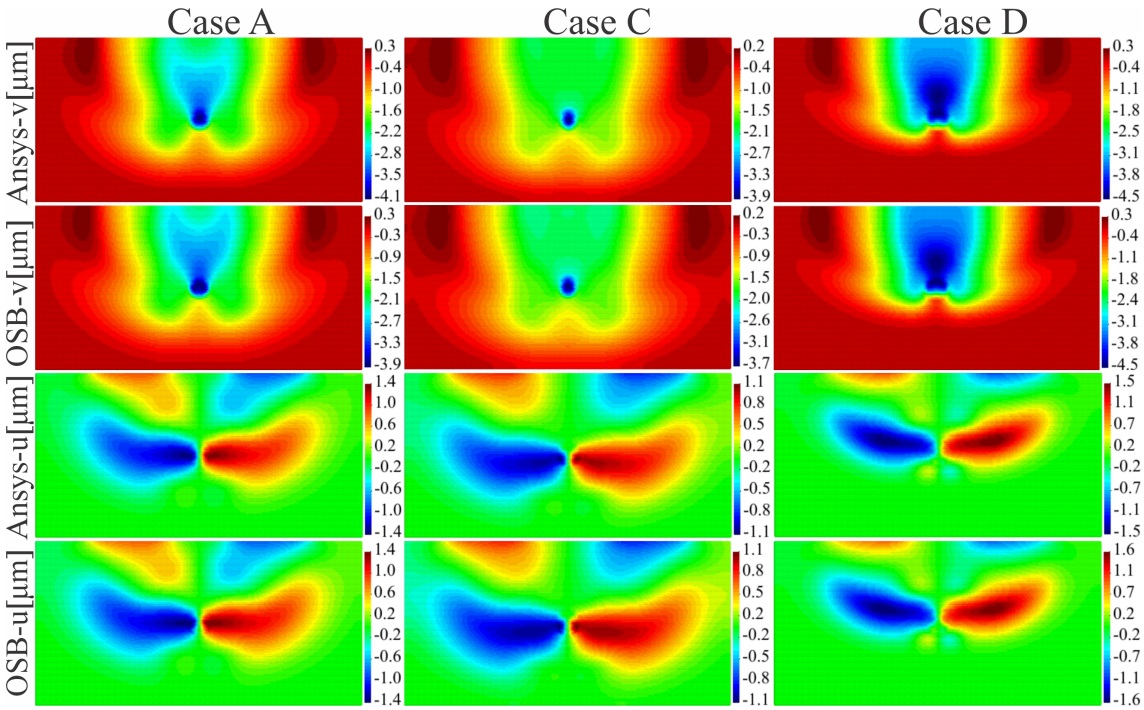

Figure 4.7: Contours of horizontal, $u(x)$ and vertical, $v(y)$, displacements obtained from ANSYS and OSB-PD analyses (with $\psi = 100$) after $3\,\mu s$ (end of simulation) for Geometry S2

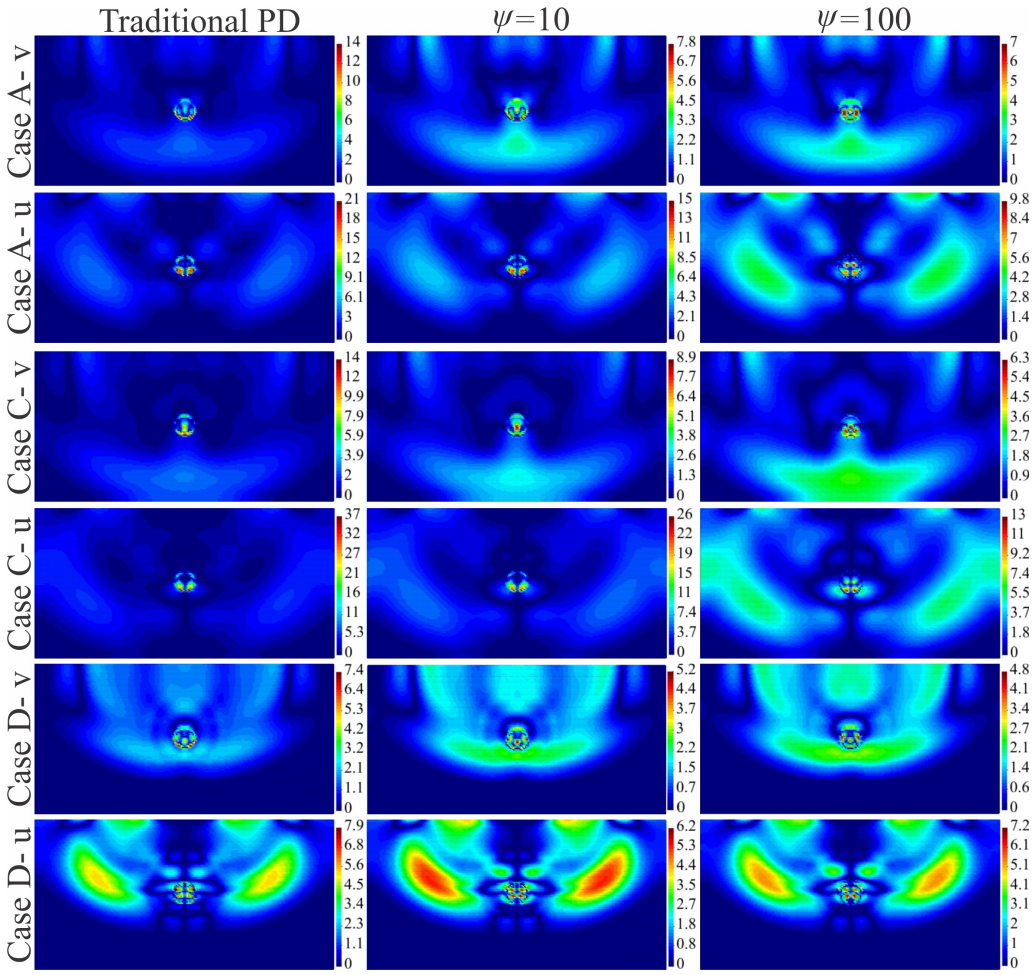

Figure 4.8: Contours of percent differences for horizontal, $u(x)$, and vertical, $v(y)$, displacements after $3\,\mu s$ (end of simulation) in Geometry S2

the results more quantitatively for changing values of ψ, the average PEs are calculated at the maximum displacement portions and are listed in Table 4.3. Note that the maximum displacement portion corresponds to the central circular region of the plates with a diameter of $10\,mm$. It can readily observed from Table 4.3 that the average PEs between ANSYS solutions and PD predictions become less than 1.5% by leveraging larger values of ψ, thereby demonstrating the higher accuracy of the present approach over the

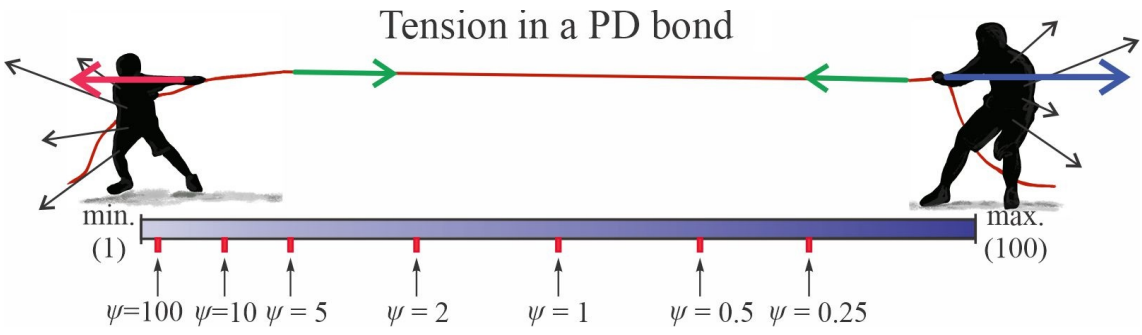

Figure 4.9: A schematic representation of the *dominancy rate* (ψ)

Table 4.3: Average percent differences for u and v displacements in Geometries L and R under impact loading

			Traditional PD	$\psi = 10$	$\psi = 100$
Geometry S1	Case A	u	1.40%	1.35%	**1.31%**
		v	0.73%	0.71%	**0.70%**
	Case C	u	1.22%	1.11%	**1.04%**
		v	**0.42%**	0.42%	0.43%
	Case D	u	0.77%	0.77%	**0.77%**
		v	1.59%	1.59%	**1.59%**
Geometry S2	Case A	u	1.85%	1.49%	**1.21%**
		v	1.35%	**1.33%**	1.34%
	Case C	u	2.13%	1.91%	**1.53%**
		v	0.98%	0.97%	**0.89%**
	Case D	u	1.21%	**1.20%**	1.29%
		v	1.62%	1.52%	**1.44%**
Geometry L	Case A	u	2.14%	1.62%	**1.18%**
		v	1.62%	1.60%	**1.40%**
	Case C	u	2.54%	2.02%	**1.36%**
		v	1.84%	1.79%	**1.55%**
	Case D	u	1.45%	1.28%	**1.25%**
		v	1.20%	1.18%	**1.10%**

traditional PD. As it is seen, average percent differences have been decreased in almost every scenario by increasing the value of ψ. This is physically what is expected. If the bond between two material points is considered as an elastic rope between two person with different strengths, then the tension in the rope would be dominated by the weaker person's strength, as shown in Fig.4.9. This similar physics is applicable for all the scenarios involving more than one material type as in the case of FGMs. Accordingly, it can be conspicuously inferred that, in problems with material transitions, the properties of a bond are mostly dependent on the properties of the weaker point and, thus, Eq.(2.18) should be used with the large values of ψ ($\psi \geq 100$) to accurately model these transition effects. It is worth mentioning that a value of $\psi \geq 100$ roughly results in the bond properties calculated as the harmonic average of the constituent points.

4.3.3. High gradient FGMs under static loading

In this case study, an FGM plate with dimensions of $L = 80mm$ and $W = 40mm$ ($200x100$ points) is subjected to a linearly distributed static load of $300kN/m$ (Fig.4.10).

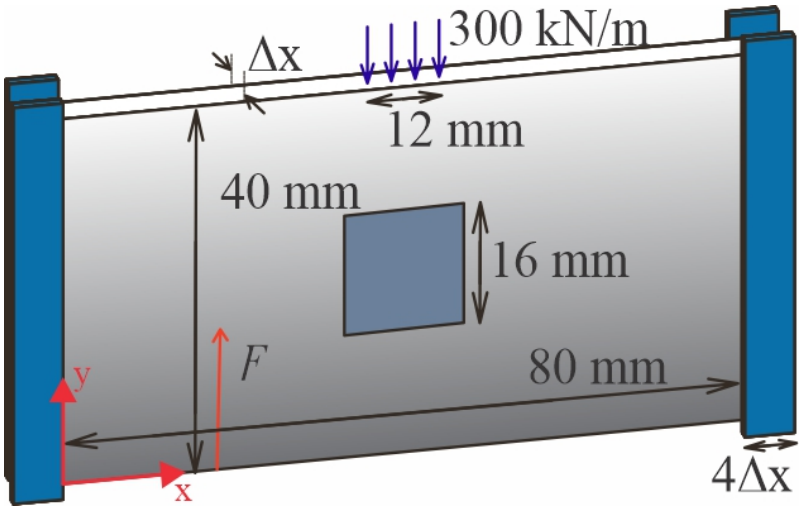

Figure 4.10: Geometric properties of FGM plate under static loading

The left and right ends of the plate are constrained in x- and y-direction by four layers of fictious material points. The material properties of the plates are taken the same as Case D of the previous problem. A square sub-region with the side length of $16mm$, a density of $\rho = 2800Kg/m^3$ and Poisson's ratio of $\nu = 0.3$ is defined in the central portion of the plate. The elastic modulus of the sub-region is taken as $E_{sub} = E_r E_{min}$. Herein, E_r is the ratio of the elastic modulus of the sub-region to the minimum possible value of the elastic modulus in the plate, E_{min}. The analyses are carried out for different values of E_r and ψ by utilizing the adaptive dynamic relaxation method [38].

Fig.4.11 and Fig.4.12, in turn, show the vertical and horizontal displacements along the vertical and horizontal lines, for different values of E_r and ψ. As can be seen from the figures, for the value of $E_r = 1$ (low gradient), the accuracy of the result is not affected by the change in the value of ψ. However, for larger change in the material properties (i.e., $E_r = 10, 0.1, 0.01, ...$), the value of ψ is observed to have high impact on the prediction capability of the model, specially at the transition regions, i.e., sub-region boundaries where the plate encounters a high gradient (a sudden jump in material properties). At these boundaries, the displacement values predicted by traditional PD show an abnormal trend, while the present formulation delivers a higher precision (Fig.4.11). Another important observation from the figures is that the properties of a bond should not completely be dependent on the properties of a single point. In other words, the value of ψ should not completely neglect the effects of the point with higher material properties. Otherwise the accuracy of the model is negatively affected, as is observed, for example, in the graphs of U_y (maximum deformation direction), for the value of $E_r = 0.01, 0.005, 0.002, 0.001$. In such cases, for high values of ψ the dominancy rate of the point with lower material properties become so high that the effects of the point with higher material properties approach zero, resulting in a lower accuracy (Fig.4.11). It is worthy to mention that the

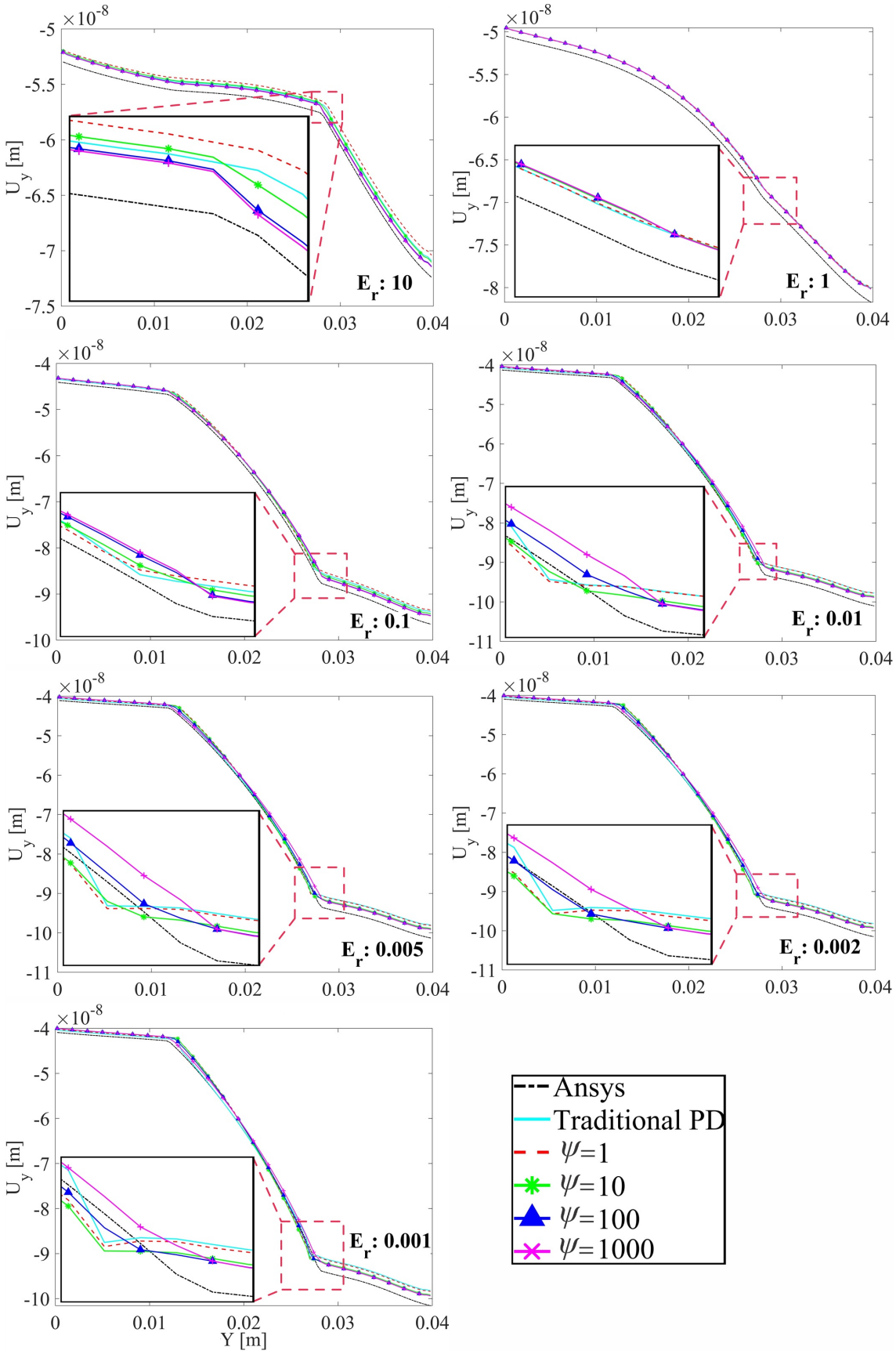

Figure 4.11: Vertical displacement, U_y, of the vertical central line in FGM plates under static loading

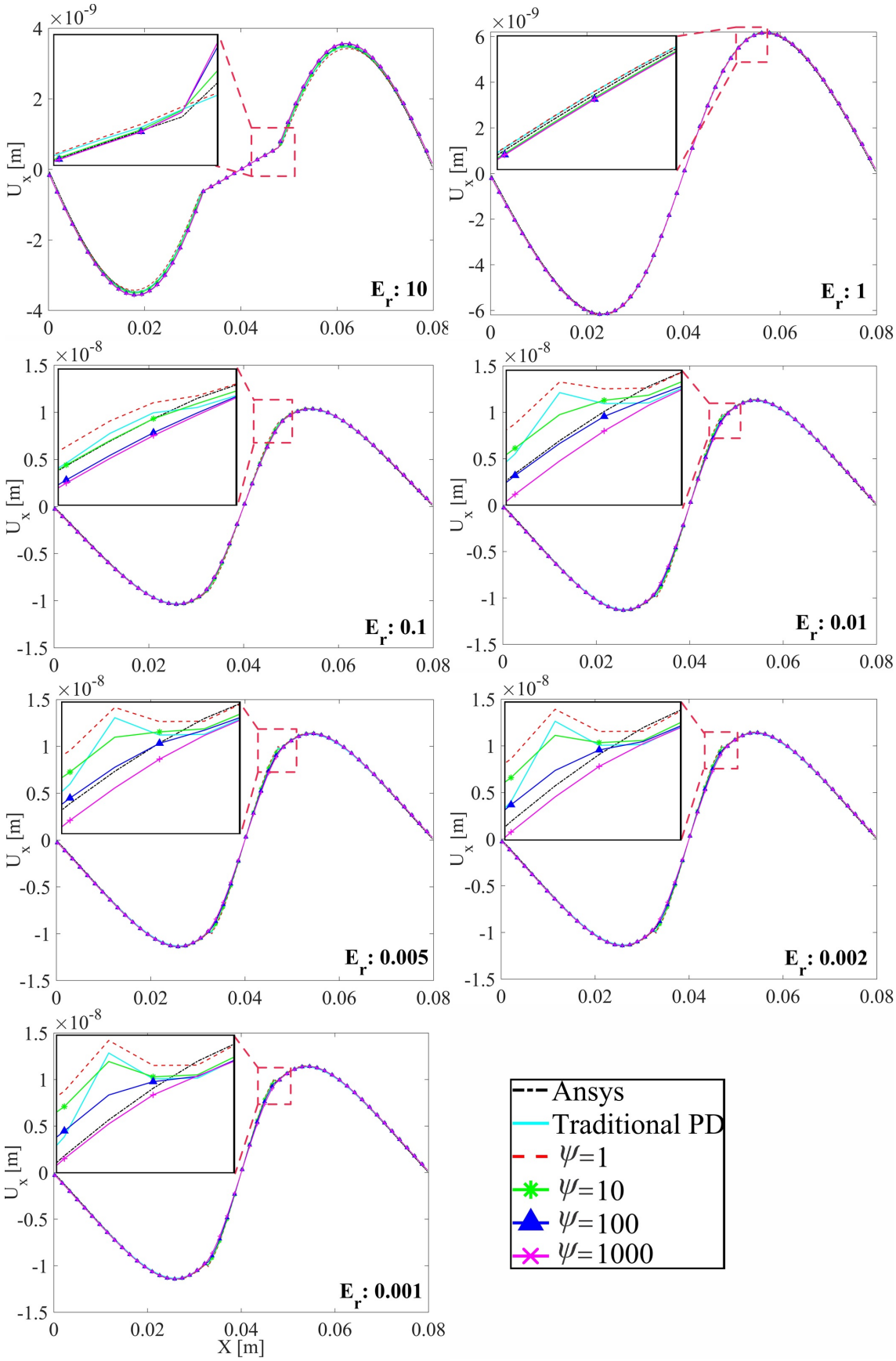

Figure 4.12: Horizontal displacement, U_x, of the horizontal central line in FGM plates under static loading

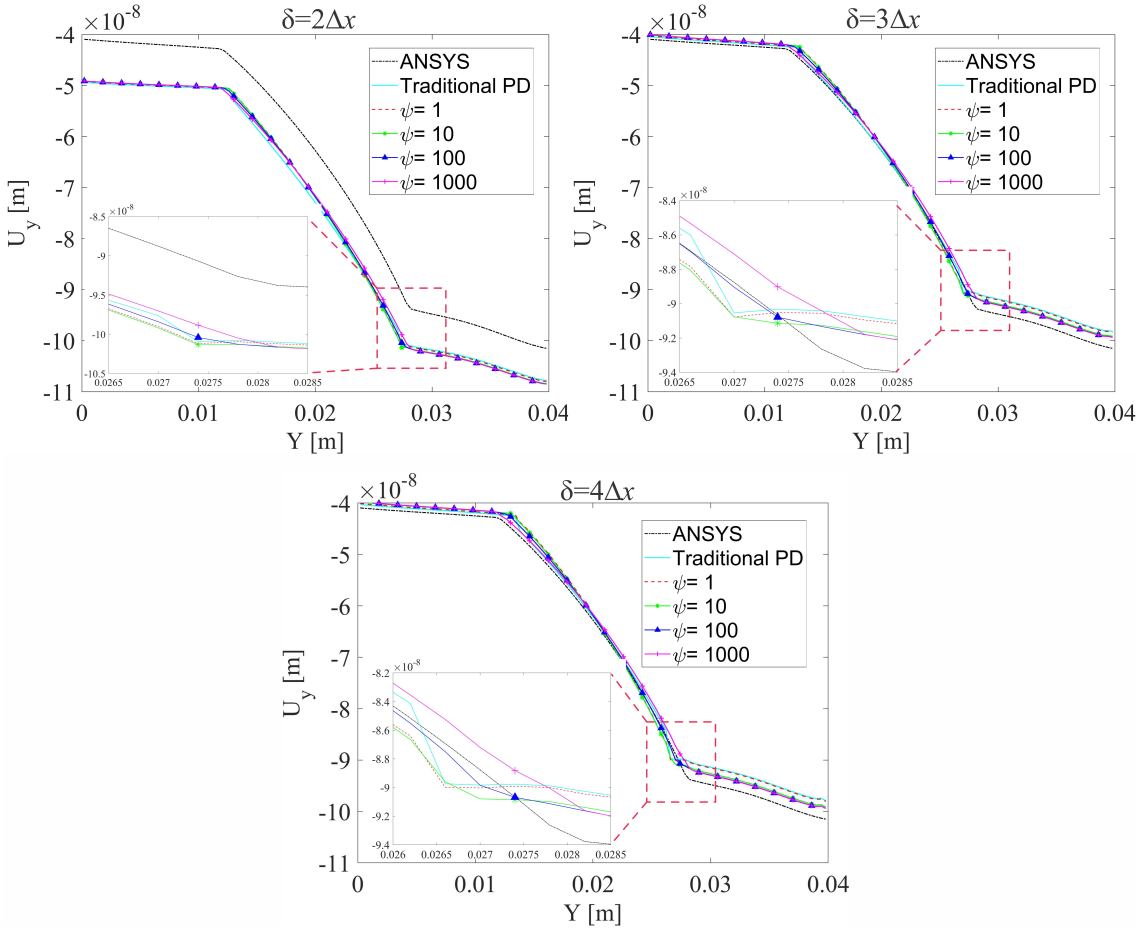

Figure 4.13: Graph of horizon-convergence for different values of ψ

size of horizon, δ, does not significantly affect the dominancy rate parameter but it does affect the overall PD accuracy, as is seen in Fig.4.13 in which different values of ψ as well as the traditional PD have yield to the same final results. This is because the change in the material properties of the neighboring points is independent of the non-locality range. However, the effects of the ψ become more obvious in the problems where the distance between material points, Δx, is significantly large. Fig.4.14 shows a comparison of the current approach with the traditional PD for different mesh resolutions with $\delta = 4\Delta x$. As is seen, the accuracy of the traditional approach has significantly decreased with increasing values of Δx, while current formulation has delivered good precision for even very high particle distancing.

4.3.4. Toughness enhancement of FGM plates using homogeneous sub-regions

In this section, we present a novel numerical toughening model to enhance FGMs against crack propagations. For this purpose, a circular sub-region with a diameter of $7\,mm$ is implemented into a plate made of FGMs with material properties given in Table

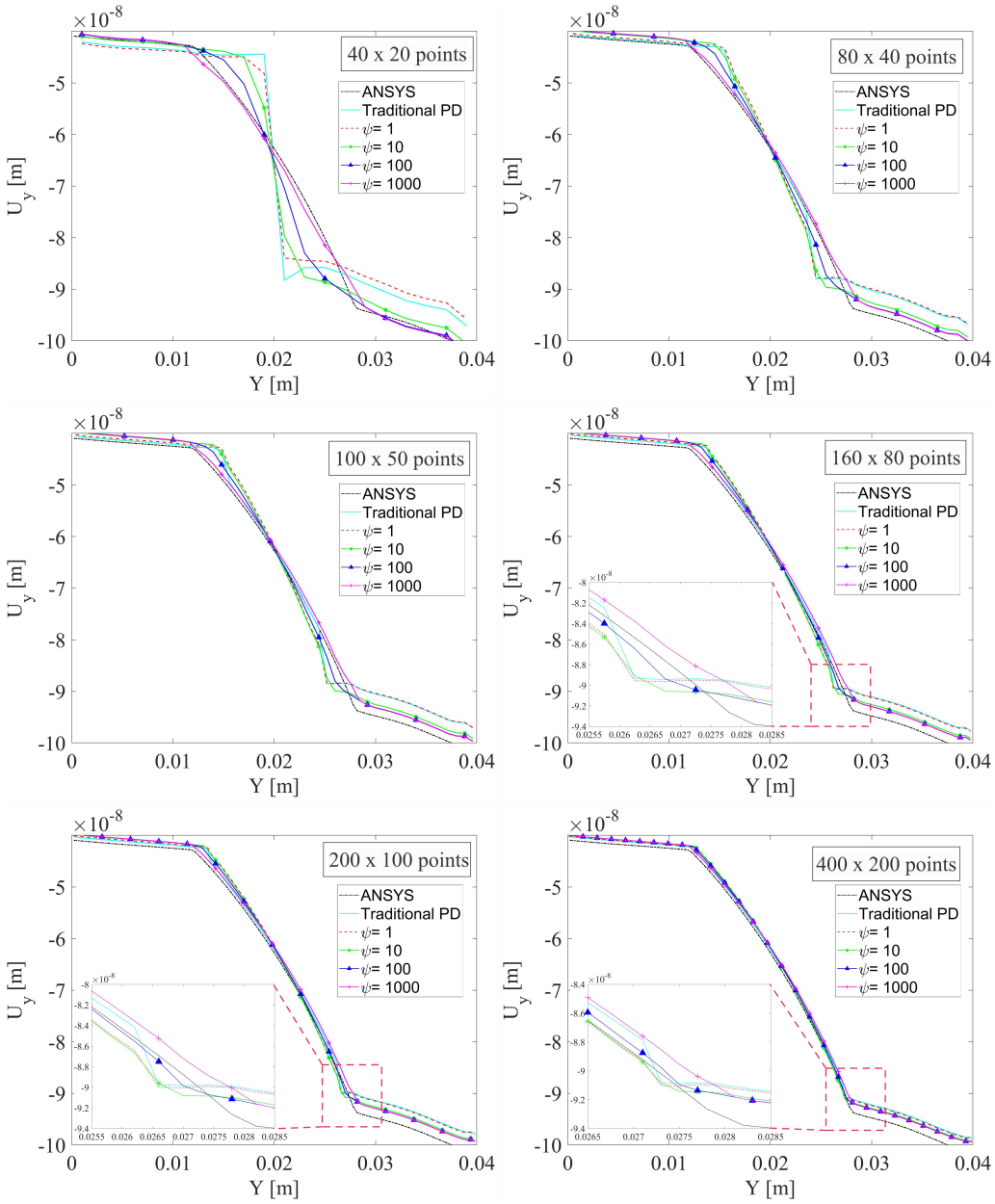

Figure 4.14: Graph of Δx-convergence for different values of ψ

4.1. The dimension of the plate is $LxW = 43mmx43mm$ which leads to a discretization of $100x100$ points. The elastic modulus of the sub-region is set to be $E = 2.94\,GPa$ which is lower than the minimum value of E in the original FGM plate. The density, Poisson's ratio, and fracture toughness of the sub-region is $\rho = 1200Kg/m^3$, $v = 0.38$ and $KIc = 1.33MPa\sqrt{m}$, respectively. The plate is subjected to a cross head velocity boundary condition of $200mm/s$ in x-direction which is applied to three fictious layers of material points at each end, as shown in Fig.4.15. The propagation of the crack is investigated for two different cases. In one of which, a pre-existing crack with the length of $8.5mm$ is located on the stiff side while in the other one, the pre-existing crack is positioned on the compliant side. Fig.4.16 shows the evolution of the crack with respect to time for the value of $\psi = 100$ in the plate with the pre-existing crack located on stiff side.

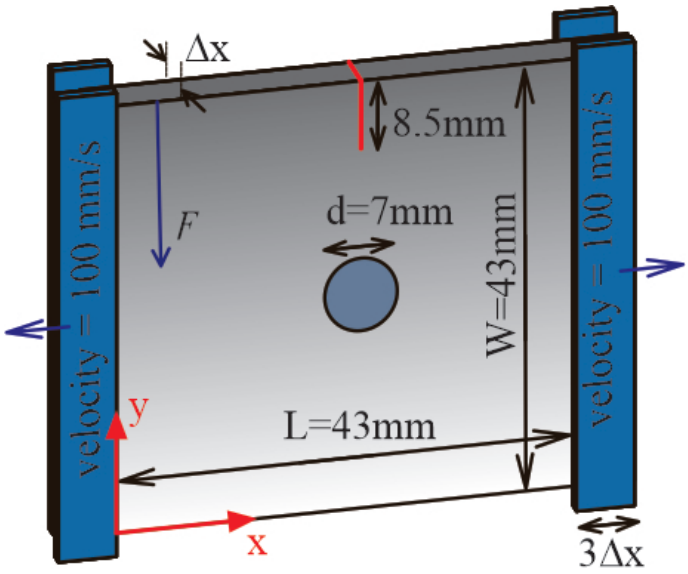

(a) Crack on stiff side

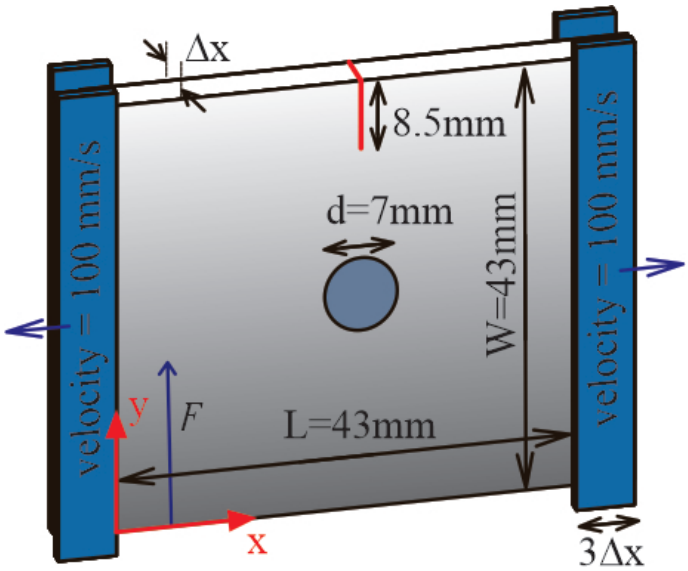

(b) Crack on compliant side

Figure 4.15: Geometric properties of the plate with a circular homogeneous sub-region

Due to the change from brittle region to elastic one, in the pristine plate, the propagation of the crack located on stiff side starts at an earlier stage of the loading than that of the compliant side. Because of the more elastic behaviors of the upper portions, at the later time-steps, the crack propagation stops for a while and continues with a relatively lower velocity. This phenomenon is even more obvious in the plate with a sub-region of slightly lower elastic modulus. As can be seen from Fig.4.16, the presence of the sub-region stops the crack propagation for a significant amount of time. This is because, when the crack enters into the sub-region with lower elastic modulus, it requires higher displacement or strain energy for further propagation, thereby putting the crack into a relaxation mode (between $400\mu s - 600\mu s$) which prolongs the complete rupture time of the FGM plate, as shown in Fig.4.17.

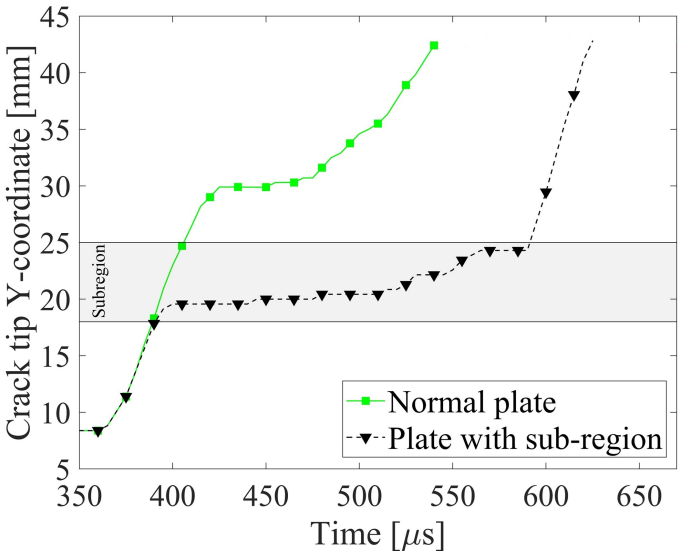

Figure 4.16: Tip evolution of the crack located on stiff side in pristine (normal) plate and the plate with sub-region

The effects of similar toughening mechanism are relatively smaller in the FGM plate with the pre-existing crack located on compliant side, as shown in Fig.4.18. This is because the location of the crack in higher elastic regions causes a delay in the crack initiation time. By the time the propagation starts, the stretch of the bonds in more brittle areas as well as in the sub-region would have already become close to their critical values. This

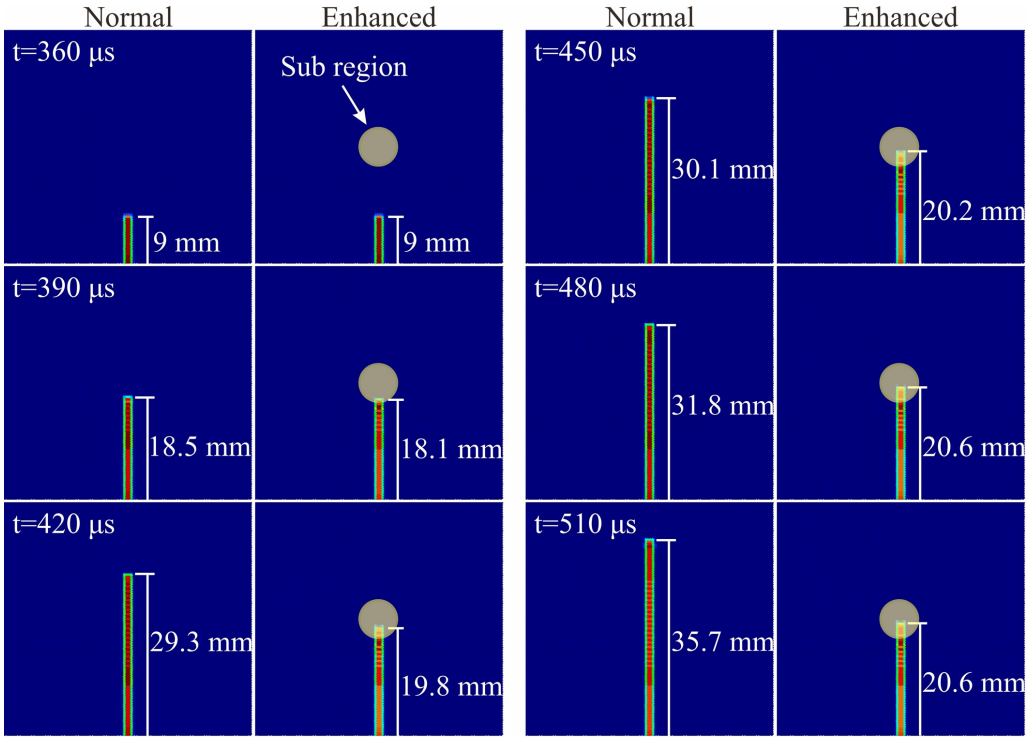

Figure 4.17: A comparison of the propagation length of the crack located on stiff side in pristine (normal) plate and the plate with sub-region

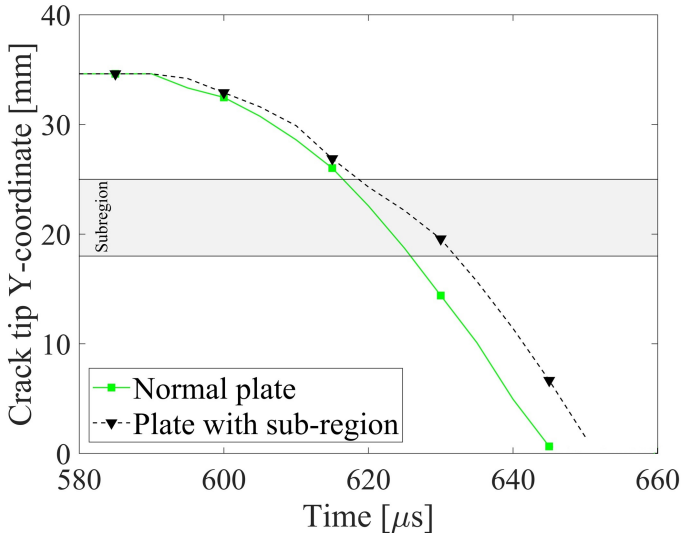

Figure 4.18: Tip evolution of the crack located on compliant side in pristine (normal) plate and the plate with sub-region

results in a rapid propagation towards more brittle regions with a continuously increasing velocity. That is why, the presence of the sub-region at the later stages of the propagation would not provide effective increment in the toughness. Nevertheless, there still a small toughening increase is seen due to the higher energy absorption of the sub-region. Overall, it can be stated that the presence of a small sub-region constituting geometrically 2% of the plate can be highly effective in increasing the total rupture time and decreasing the average crack propagation velocity.

4.3.5. Toughness enhancement of FGM plates using sub-regions of flipped properties

In this case study, the geometry, material properties, and loading condition of the previous case study are used to investigate the effects of the sub-regions with flipped properties. To this end, a square region (namely the sub-region) with the side lengths of $7mm$ is located at a y-distance of d from the crack tip. The properties of the sub-region is flipped from its central axis in y-direction, as shown in Fig.4.19, where two different scenarios are considered with the crack locations on stiff and compliant side. Fig.4.20 shows the evolution of the crack with respect to time in the pristine plate (with no sub-region) and the plate with flipped sub-regions (colored graph) for different values of d. A two-dimensional representation is also given in Fig.4.21. The regions of the colored graph which remains on the upper side of the shaded graph indicate the amount of enhancement against crack propagation. For instance in Fig.4.20a, at an instant of $560\,\mu s$, the crack tip reaches a distance of $35mm$ in the plate with the sub-region located at $d = 13mm$, whereas a complete rupture is observed in the pristine plate. Specifically, the presence of the sub-region has caused an almost $10mm$ decrease in the final length of the crack.

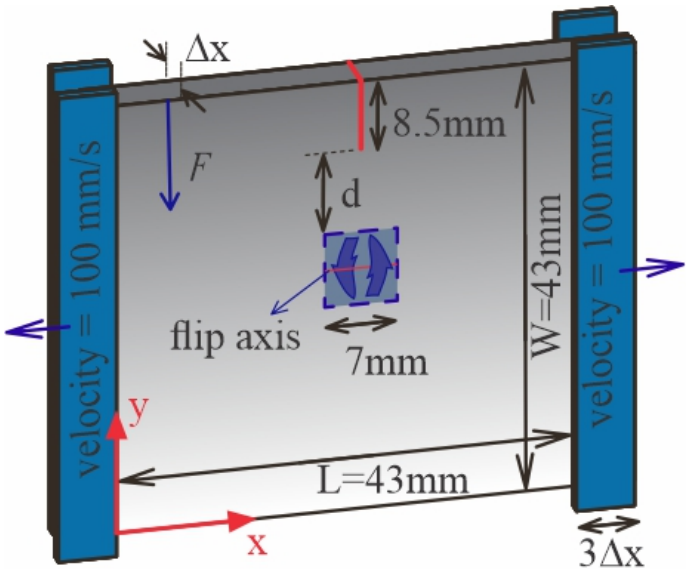

(a) Crack on stiff side

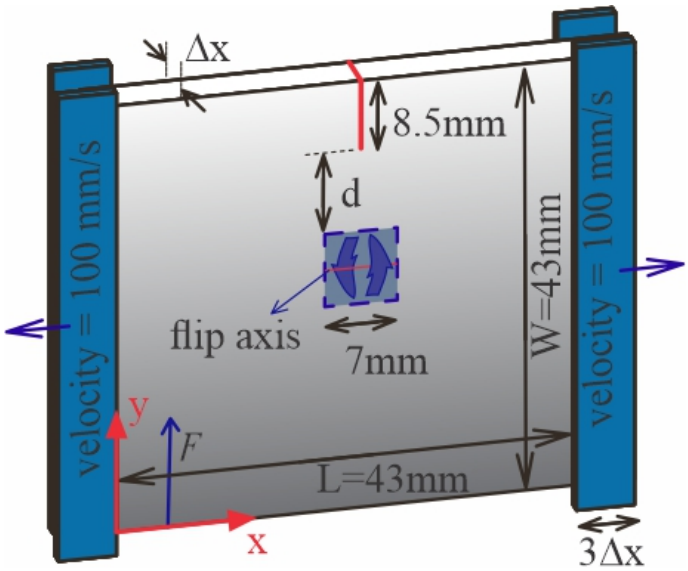

(b) Crack on compliant side

Figure 4.19: Geometric properties of the plate with square flipped sub-region

However, this toughening effect is noted to be irregularly varying with respect to time and the sub-region's location, d, in plate with crack located on stiff side. This irregular variation can be attributed to the irregular ex-change of the brittle properties of the lower portion of sub-region with the more elastic ones on the upper portion. In this geometry, the variation of the critical energy release rate, G_c, through the width of the plate has a sinusoidal profile, as seen in Fig.4.22. It is known that the profile has a maximal, minimal and inflection point (where $d \approx 13mm$). By introducing the sub-region at a distance of $d = 13mm$, a highly distinguishable change in the profile of G_c emerges, thereby resulting in a longer relaxation for the crack propagation. Moreover, a converse effect is captured for the values of $d = 3mm$ and $d = 5mm$, in which the crack relaxation begins later and lasts shorter. On the other hand, because of the symmetry existed around the maximal

and minimal points, flipping the geometry in these regions would not significantly affect the material properties, and thus resulting in negligible toughening effects. Although the same variation of G_c is present in the geometry with crack located on compliant side, the enhancement effect is observed to be regularly decreasing with increasing values of d. This is because the initiation of the crack propagation starts at an instant in which the stretch of the bonds is closer to their critical value. Due to the high velocity of the crack-propagation, the presence of sub-regions at the late stages remains incapable of sufficiently decreasing the propagation rate. Therefore, in the geometry with crack located on the compliant side, the sub-region is only effective when its located near the crack tip (at a $0-10mm$ distance from the tip). Such effects have been observed in the previous case studies as well. Hence, it can be concluded that the implementation of toughening

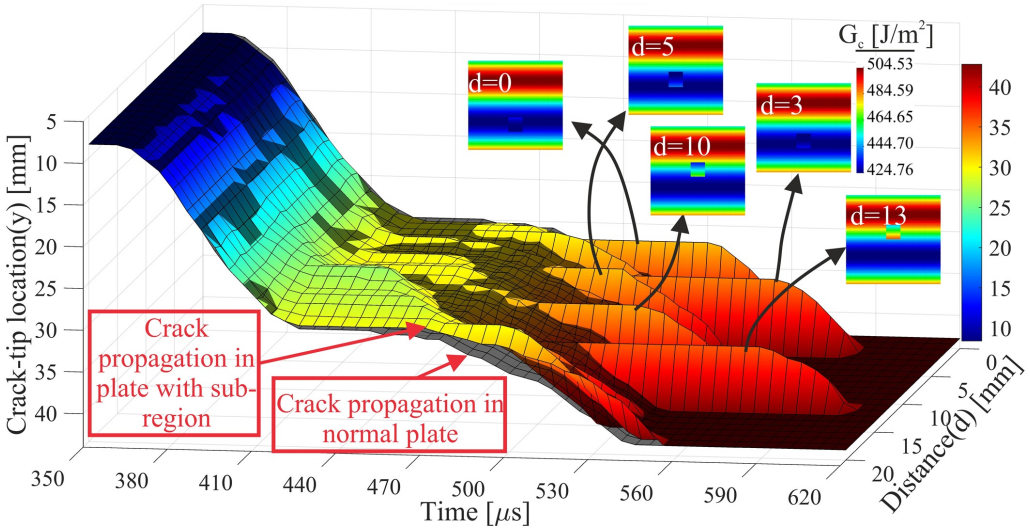

(a) Crack on stiff side

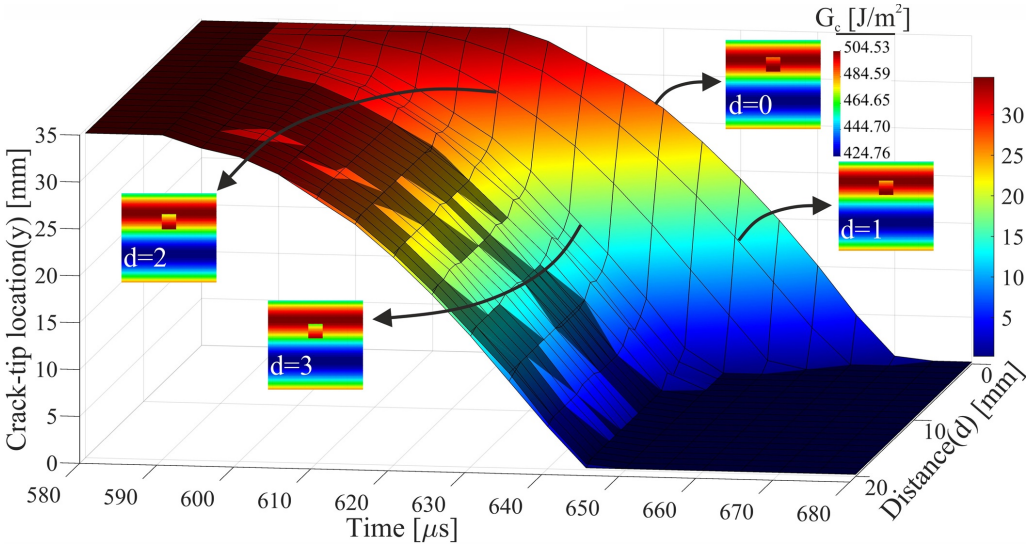

(b) Crack on compliant side

Figure 4.20: A 3D representation of the evolution of the crack with respect to time for different values of d

mechanism requires more attention for the case of pre-existing crack located on the compliant side. It is also important to note that where the shaded area in Fig.4.20 remains above the colored graph, inclusion of the sub-region accelerates the local speed of the crack propagation. Consequently, it is crucial to properly design the material properties of the sub-region and optimize its distance to obtain a superior toughening effect. Accordingly, this study sheds a light on viable design of toughening mechanisms in FGMs by providing the necessary guidelines with the comprehensive results depicted in Fig.4.20.

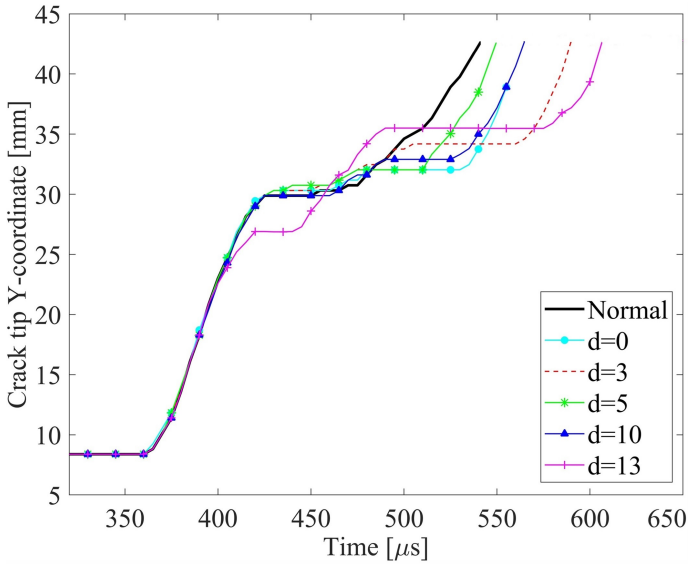

(a) Crack on stiff side

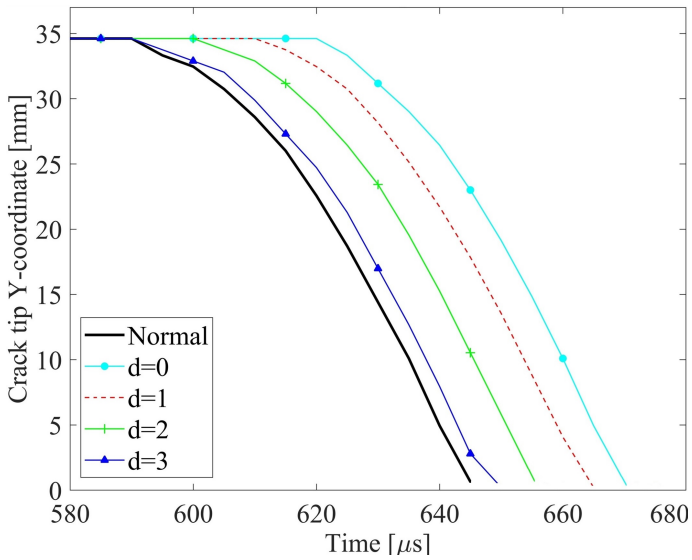

(b) Crack on compliant side

Figure 4.21: The 2D representation of the evolution of the crack with respect to time for different values of d

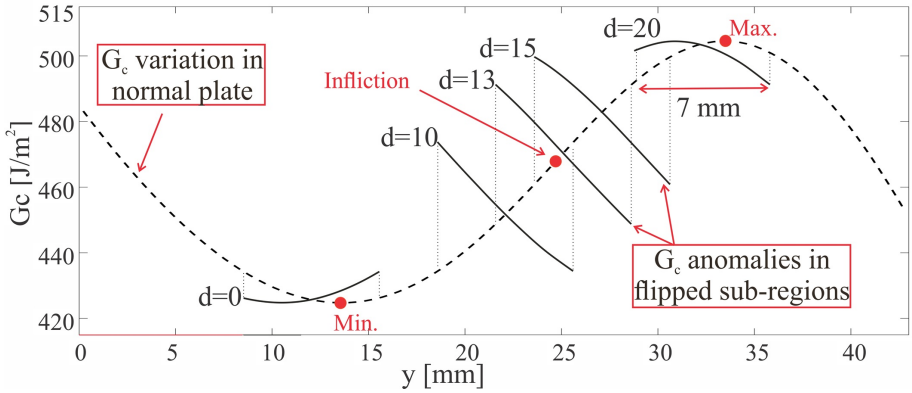

Figure 4.22: G_c variation in pristine (normal) plate and the plates with flipped sub-region

4.4. Conclusions

In the scope of this study, a comprehensive formulation of Ordinary-State based peridynamic (OSB-PD) approach is presented for accurate modeling of Functionally Graded Materials (FGMs) with high material gradients and/or a jump in the material properties. An important contribution of the current formulation is its adjustable nature through introducing the dominancy rate parameter, ψ, into PD literature for FGMs, which enables handling complex problems involving different length-scales. To this end, this paper indicates that the properties of a PD-bond should not be affected by that of constituent material points equally under different circumstances. The overall numerical methodology is corroborated by solving various test cases involving FGM plates with high gradients under dynamic/static loading conditions. In these test cases, sub-regions are introduced to exemplify the sharp and sudden transitions of the material properties in high gradient FGMs. It is demonstrated that the current model better captures the experimental and numerical crack behaviors if compared with phase field, FEM, and other existing peridynamic literature. It is indicated that different values of ψ yield to the same results when solving FGMs with low material gradients. However, the accurate selection of ψ is shown to be important for FGMs with higher gradients where the properties of the material points constituting a PD-bond can differ significantly. It is proved that the properties of a PD-bond should be dependent mostly on the properties of the weaker material point, i.e., $\psi \approx 100$ which roughly corresponds to the harmonic average properties of the points. It is also observed that the accuracy of the results is adversely affected if the properties of a bond is computed using the properties of only one of the weaker or stronger constituent points. Overall, a more realistic FGM-PD model is constructed by considering the multi-scale nature of PD as well as material transition effects.

Furthermore, as a particular application of the current formulation, a numerically validated toughening model is proposed to increase the toughness of FGMs against crack propagations. For this purpose, the propagation of the crack is investigated under two

different set-ups, namely, the FGM plates enhanced with homogeneous and with flipped sub-regions. While the former one requires a change in the material properties, the latter one necessitates a modification in the manufacturing procedure only. It is demonstrated that upon implementing either or both of the above approaches, the toughness of the FGMs can be increased notably. It is also observed that in the case of the flipped sub-region, the toughening effect is the highest if the flipping of the sub-region is performed at the regions near to the infliction point(s) of the G_c variation. Overall, this study provides a unique contribution to the existing state of the art in terms of proposing a novel PD methodology which can handle modeling of FGMs with sharp transitions in material properties as well as suggesting numerically validated new toughening configurations for FGMs.

Bibliography

[1] Haoxuan Cui et al. “Failure analysis of the brittle fracture of a thick-walled 20 steel pipe in an ammonia synthesis unit”. In: *Engineering Failure Analysis* 17.6 (2010), pp. 1359–1376. ISSN: 13506307. DOI: 10.1016/j.engfailanal.2010.04.002.

[2] V. Infante et al. “Failure of a crankshaft of an aeroengine: A contribution for an accident investigation”. In: *Engineering Failure Analysis* 35 (2013), pp. 286–293. ISSN: 13506307. DOI: 10.1016/j.engfailanal.2013.02.002.

[3] Torgeir Moan and Jorgen Amdahl. “Catastrophic failure modes of marine structures”. In: *Structural failure*. 1989, pp. 463–510.

[4] A G EVANS and K T FABER. “Crack-Growth Resistance of Microcracking Brittle Materials”. In: *Journal of the American Ceramic Society* 67.4 (1984), pp. 255–260. DOI: https://doi.org/10.1111/j.1151-2916.1984.tb18842.x.

[5] A G Evans and Y Fu. “Some effects of microcracks on the mechanical properties of brittle solids—II. Microcrack toughening”. In: *Acta Metallurgica* 33.8 (1985), pp. 1525–1531. ISSN: 0001-6160. DOI: https://doi.org/10.1016/0001-6160(85)90053-7.

[6] D. Vashishth, J. C. Behiri, and W. Bonfield. “Crack growth resistance in cortical bone: Concept of microcrack toughening”. In: *Journal of Biomechanics* 30.8 (1997), pp. 763–769. ISSN: 00219290. DOI: 10.1016/S0021-9290(97)00029-8.

[7] K. T. Faber and A. G. Evans. “Crack deflection processes-I. Theory”. In: *Acta Metallurgica* 31.4 (1983), pp. 565–576. ISSN: 00016160. DOI: 10.1016/0001-6160(83)90046-9.

[8] M. Fanni et al. “New crack stop hole shape using structural optimizing technique”. In: *Ain Shams Engineering Journal* 6.3 (2015), pp. 987–999. ISSN: 20904479. DOI: 10.1016/j.asej.2015.02.010.

[9] Md. Shafiul Ferdous et al. “A Review of Simple Methods for Arresting Crack Growth”. In: *Advanced Materials Research* 1110.June (2015), pp. 185–190. DOI: 10.4028/www.scientific.net/amr.1110.185.

[10] Hao Wu et al. “On the prediction of the residual fatigue life of cracked structures repaired by the stop-hole method”. In: *International Journal of Fatigue* 32.4 (2010), pp. 670–677. ISSN: 01421123. DOI: 10.1016/j.ijfatigue.2009.09.011.

[11] Y. Huang and A. J. Kinloch. "Modelling of the toughening mechanisms in rubber-modified epoxy polymers - Part I Finite element analysis studies". In: *Journal of Materials Science* 27.10 (1992), pp. 2753–2762. ISSN: 00222461. DOI: 10.1007/BF00540702.

[12] R.H.J. Hannink. *Toughening Mechanisms for Ceramics*. Vol. 19. Elsevier B.V., 1994. DOI: 10.1016/b978-1-4832-8382-1.50173-7.

[13] David Broek. "Practical Problems". In: *Elementary Engineering Fracture Mechanics*. Marinus Nijhoff, 1982, pp. 347–376. ISBN: 9024726565.

[14] Hiroomi Miyagawa and Hironobu Nisitani. "Retardation of Fatigue Crack Propagation Due to Additional Holes or Indentations in Plate Specimens". In: *Bulletin of the JSME* 28.244 (1985), pp. 84–0318. ISSN: 00213764. DOI: 10.1299/jsme1958.28.2219.

[15] A. A. Griffits. "The phenomena of rupture and flow in solids". In: *Masinovedenie* C.1 (1995), pp. 9–14. ISSN: 00254576. DOI: 10.1098/rsta.1921.0006.

[16] A Hillerborg, M Modéer, and P.-E. Petersson. "Analysis of crack formation and crack growth in concrete by means of fracture mechanics and finite elements". In: *Cement and Concrete Research* 6.6 (1976), pp. 773–781. ISSN: 0008-8846. DOI: https://doi.org/10.1016/0008-8846(76)90007-7.

[17] D S Dugdale. "Yielding of steel sheets containing slits". In: *Journal of the Mechanics and Physics of Solids* 8.2 (1960), pp. 100–104. ISSN: 0022-5096. DOI: https://doi.org/10.1016/0022-5096(60)90013-2.

[18] T. Belytschko and T. Black. "Elastic crack growth in finite elements with minimal remeshing". In: *International Journal for Numerical Methods in Engineering* 45.5 (1999), pp. 601–620. ISSN: 00295981. DOI: https://doi.org/10.1002/1097-0207(19)99062-0.

[19] S. A. Silling. "Reformulation of elasticity theory for discontinuities and long-range forces". In: *Journal of the Mechanics and Physics of Solids* 48.1 (2000), pp. 175–209. ISSN: 00225096. DOI: 10.1016/S0022-5096(99)00029-0.

[20] E. Askari et al. "Peridynamics for multiscale materials modeling". In: *Journal of Physics: Conference Series* 125 (2008). ISSN: 17426596. DOI: 10.1088/1742-6596/125/1/012078.

[21] S. A. Silling et al. "Peridynamic states and constitutive modeling". In: *Journal of Elasticity* 88.2 (2007), pp. 151–184. ISSN: 03743535. DOI: 10.1007/s10659-007-9125-1.

[22] S. A. Silling and E. Askari. “A meshfree method based on the peridynamic model of solid mechanics”. In: *Computers and Structures* 83.17-18 (2005), pp. 1526–1535. ISSN: 00457949. DOI: 10.1016/j.compstruc.2004.11.026.

[23] S. A. Silling. “Linearized theory of peridynamic states”. In: *Journal of Elasticity* 99.1 (2010), pp. 85–111. ISSN: 03743535. DOI: 10.1007/s10659-009-9234-0.

[24] Erkan Oterkus et al. “Combined finite element and peridynamic analyses for predicting failure in a stiffened composite curved panel with a central slot”. In: *Composite Structures* 94.3 (2012), pp. 839–850. ISSN: 02638223. DOI: 10.1016/j.compstruct.2011.07.019.

[25] Dong Yang et al. “An improved ordinary state-based peridynamic model for cohesive crack growth in quasi-brittle materials”. In: *International Journal of Mechanical Sciences* 153-154.February (2019), pp. 402–415. ISSN: 00207403. DOI: 10.1016/j.ijmecsci.2019.02.019.

[26] Selda Oterkus, Erdogan Madenci, and Abigail Agwai. “Fully coupled peridynamic thermomechanics”. In: *Journal of the Mechanics and Physics of Solids* 64.1 (2014), pp. 1–23. ISSN: 00225096. DOI: 10.1016/j.jmps.2013.10.011.

[27] Selda Oterkus, Erdogan Madenci, and Abigail Agwai. “Peridynamic thermal diffusion”. In: *Journal of Computational Physics* 265 (2014), pp. 71–96. ISSN: 10902716. DOI: 10.1016/j.jcp.2014.01.027.

[28] Adnan Kefal, Abdolrasoul Sohouli, and Erkan Oterkus. “Topology optimization of cracked structures using peridynamics”. In: *Continuum Mechanics and Thermodynamics* (2019). ISSN: 1432-0959. DOI: 10.1007/s00161-019-00830-x.

[29] A. Sohouli et al. “Continuous Density-Based Topology Optimization of Cracked Structures Using Peridynamics”. In: *Structural and Multidisciplinary Optimization* (0). ISSN: 00219606. DOI: 10.1063/1.1730376.

[30] Anahita Habibian et al. “Multi-material topology optimization of structures with discontinuities using Peridynamics”. In: *Composite Structures* 258 (2021), p. 113345. ISSN: 0263-8223. DOI: https://doi.org/10.1016/j.compstruct.2020.113345. URL: http://www.sciencedirect.com/science/article/pii/S0263822320332712.

[31] Muhammed Fatih Basoglu et al. “A computational model of peridynamic theory for deflecting behavior of crack propagation with micro-cracks”. In: *Computational Materials Science* 162.February (2019), pp. 33–46. ISSN: 09270256. DOI: 10.1016/j.commatsci.2019.02.032.

[32] Bahattin Kilic and Erdogan Madenci. “Coupling of Peridynamic Theory and The Finite Element Method”. In: *Journal of Mechanics of Materials and Structures* 5.5 (2010).

[33] Erdogan Madenci et al. “Isogeometric analysis using peridynamics and XFEM”. In: 210049. American Institute of Aeronautics and Astronautics, 2018, pp. 1–21. ISBN: 9781624105326. DOI: 10.2514/6.2018-1464.

[34] Zhanqi Cheng et al. “A peridynamic model for dynamic fracture in functionally graded materials”. In: *Composite Structures* 133 (2015), pp. 529–546. ISSN: 02638223. DOI: 10.1016/j.compstruct.2015.07.047.

[35] M. Ozdemir et al. “Dynamic fracture analysis of functionally graded materials using ordinary state-based peridynamics”. In: *Composite Structures* 244.February (2020), p. 112296. ISSN: 02638223. DOI: 10.1016/j.compstruct.2020.112296.

[36] Erdogan Madenci and Erkan Oterkus. *Peridynamic theory and its applications*. Vol. 9781461484. Springer, 2014. ISBN: 9781461484653. DOI: 978-1-4614-8465-3.

[37] Leon Lapidus and George F. Pinder. *Numerical Solution of PDEs in Science and Engineering*. A Wiley-interscience Publication, 1999. ISBN: 0471098663.

[38] B. Kilic and E. Madenci. “An adaptive dynamic relaxation method for quasi-static simulations using the peridynamic theory”. In: *Theoretical and Applied Fracture Mechanics* 53.3 (2010), pp. 194–204. ISSN: 01678442. DOI: 10.1016/j.tafmec.2010.08.001.

[39] R. S. Yang et al. “Hole Defects Affect the Dynamic Fracture Behavior of Nearby Running Cracks”. In: *Shock and Vibration* 2018 (2018). ISSN: 10709622. DOI: 10.1155/2018/5894356.

[40] Zhong qiu Fu et al. “Crack stop holes in steel bridge decks: Drilling method and effects”. In: *Journal of Central South University* 24.10 (2017), pp. 2372–2381. ISSN: 22275223. DOI: 10.1007/s11771-017-3649-8.

[41] Rachid Ghfiri et al. “Effects of expanded and non-expanded hole on the delay of arresting crack propagation for aluminum alloys”. In: *Materials Science and Engineering A* 286.2 (2000), pp. 244–249. ISSN: 09215093. DOI: 10.1016/S0921-5093(00)00805-4.

[42] P. S. Song and Y. L. Shieh. “Stop drilling procedure for fatigue life improvement”. In: *International Journal of Fatigue* 26.12 (2004), pp. 1333–1339. ISSN: 01421123. DOI: 10.1016/j.ijfatigue.2004.04.009.

[43] M. R. Ayatollahi, S. M.J. Razavi, and H. R. Chamani. “Fatigue life extension by crack repair using stop-hole technique under pure mode-i and pure mode-ii loading conditions”. In: *Procedia Engineering* 74 (2014), pp. 18–21. ISSN: 18777058. DOI: 10.1016/j.proeng.2014.06.216.

[44] Jenny Carlsson and Per Isaksson. "Crack dynamics and crack tip shielding in a material containing pores analysed by a phase field method". In: *Engineering Fracture Mechanics* 206.November 2018 (2019), pp. 526–540. ISSN: 00137944. DOI: 10.1016/j.engfracmech.2018.11.013.

[45] Hongxiao Wang, Xiaohui Zhang, and Yugang Duan. "Effects of drilling area temperature on drilling of carbon fiber reinforced polymer composites due to temperature-dependent properties". In: *International Journal of Advanced Manufacturing Technology* 96.5-8 (2018), pp. 2943–2951. ISSN: 14333015. DOI: 10.1007/s00170-018-1810-7.

[46] Florin Bobaru and Guanfeng Zhang. "Why do cracks branch? A peridynamic investigation of dynamic brittle fracture". In: *International Journal of Fracture* 196.1-2 (2015), pp. 59–98. ISSN: 15732673. DOI: 10.1007/s10704-015-0056-8.

[47] M. R. Ayatollahi and M. R.M. Aliha. "Analysis of a new specimen for mixed mode fracture tests on brittle materials". In: *Engineering Fracture Mechanics* 76.11 (2009), pp. 1563–1573. ISSN: 00137944. DOI: 10.1016/j.engfracmech.2009.02.016.

[48] Bozo Vazic et al. "Dynamic propagation of a macrocrack interacting with parallel small cracks". In: *AIMS Materials Science* 4.1 (2017), pp. 118–136. ISSN: 23720468. DOI: 10.3934/matersci.2017.1.118.

[49] *Alloy - Wikipedia*. [Online; accessed 2020-06-29]. 0. URL: https://en.wikipedia.org/wiki/Alloy.

[50] Mekonnen Asmare Fentahun and Mahmut Ahsen Savaş. "Materials Used in Automotive Manufacture and Material Selection Using Ashby Charts". In: *International Journal of Materials Engineering* 8.3 (2018), pp. 40–54. DOI: 10.5923/j.ijme.20180803.02.

[51] Rajender Singh. *Introduction to Basic Manufacturing Processes and Workshop Technology*. New Age International Publishers, 2006. ISBN: 9788122423167.

[52] Rasheedat M. Mahamood et al. "Functionally graded material: An overview". In: *Lecture Notes in Engineering and Computer Science* 3 (2012), pp. 1593–1597. ISSN: 20780958.

[53] Eric F. Drake. "Metal Cutting Tools Utilizing Gradient Composites". 4368788 (USA). 1983.

[54] Fumio Nogata and Hideaki Takahashi. "Intelligent functionally graded material: Bamboo". In: *Composites Engineering* 5.7 (1995), pp. 743–751. ISSN: 09619526. DOI: 10.1016/0961-9526(95)00037-N.

[55] K. S. Ravichandran. “Thermal residual stresses in a functionally graded material system”. In: *Materials Science and Engineering A* 201.1-2 (1995), pp. 269–276. ISSN: 09215093. DOI: 10.1016/0921-5093(95)09773-2.

[56] Jaedeok Yoo et al. “Transformation-Toughened Ceramic Multilayers with Compositional Gradients”. In: *Journal of the American Ceramic Society* 81.1 (Jan. 1, 1998). doi: 10.1111/j.1151-2916.1998.tb02291.x, pp. 21–32. ISSN: 0002-7820. DOI: 10.1111/j.1151-2916.1998.tb02291.x.

[57] Alireza Abdollahi et al. “SiC Nanoparticles Toughened-SiC/MoSi2-SiC Multilayer Functionally Graded Oxidation Protective Coating for Carbon Materials at High Temperatures”. In: *Journal of Materials Engineering and Performance* 26.6 (2017), pp. 2878–2889. ISSN: 15441024. DOI: 10.1007/s11665-017-2725-4.

[58] Sabina Beranič Klopčič et al. “The Preparation and Properties of Functionally Graded Alumina/Zirconia-Toughened Alumina (ZTA) Ceramics for Biomedical Applications”. In: *Key Engineering Materials* 290 (2005), pp. 348–352. ISSN: 1662-9795. DOI: 10.4028/www.scientific.net/KEM.290.348.

[59] Eric Schwarzer et al. “Process development for additive manufacturing of functionally graded alumina toughened zirconia components intended for medical implant application”. In: *Journal of the European Ceramic Society* 39.2-3 (2019), pp. 522–530. ISSN: 1873619X. DOI: 10.1016/j.jeurceramsoc.2018.09.003.

[60] Rkp Singh et al. “A Review on Functionally Gradient Materials (FGMs) and Their Applications”. In: *IOP Conference Series: Materials Science and Engineering* 229.1 (2017). ISSN: 1757899X. DOI: 10.1088/1757-899X/229/1/012021.

[61] Alan J. Markworth and James H. Saunders. “A model of structure optimization for a functionally graded material”. In: *Materials Letters* 22.1-2 (1995), pp. 103–107. ISSN: 0167577X. DOI: 10.1016/0167-577X(94)00238-X.

[62] J. S. Lin and Y. Miyamoto. “Notch effect of surface compression and the toughening of graded Al2O3/TiC/Ni materials”. In: *Acta Materialia* 48.3 (2000), pp. 767–775. ISSN: 13596454. DOI: 10.1016/S1359-6454(99)00362-6.

[63] J. Abanto-Bueno and J. Lambros. “An experimental study of mixed mode crack initiation and growth in functionally graded materials”. In: *Experimental Mechanics* 46.2 (2006), pp. 179–196. ISSN: 00144851. DOI: 10.1007/s11340-006-6416-6.

[64] Xin Jin et al. “Experimental investigation of the mixed-mode crack propagation in ZrO2/NiCr functionally graded materials”. In: *Engineering Fracture Mechanics* 76.12 (2009), pp. 1800–1810. ISSN: 00137944. DOI: 10.1016/j.engfracmech.2009.04.003.

[65] Yasuyoshi Fukui and Noboru Yamanaka. “Elastic Analysis for Thick-Walled Tubes of Functionally Graded Material Subjected to Internal Pressure”. In: *JSME International Journal* 35.4 (1992), pp. 379–385.

[66] Arkadi Berezovski, Juri Engelbrecht, and G. A. Maugin. “Numerical simulation of two-dimensional wave propagation in functionally graded materials”. In: *European Journal of Mechanics, A/Solids* 22.2 (2003), pp. 257–265. ISSN: 09977538. DOI: 10.1016/S0997-7538(03)00029-9.

[67] Saeid Hedayatrasa et al. “Numerical modeling of wave propagation in functionally graded materials using time-domain spectral Chebyshev elements”. In: *Journal of Computational Physics* 258 (2014), pp. 381–404. ISSN: 10902716. DOI: 10.1016/j.jcp.2013.10.037.

[68] J. W. Eischen. “Fracture of nonhomogeneous materials”. In: *International Journal of Fracture* 34.1 (1987), pp. 3–22. ISSN: 03769429. DOI: 10.1007/BF00042121.

[69] Feridun Delale and Ferdi Erdogan. “The Crack Problem for a Nonhomogeneous Plane”. In: *Journal of Applied Mechanics, Transactions ASME* 50 (1983). DOI: 10.1115/1.3167098.

[70] M. S. Kirugulige and V. H. Tippur. “Mixed-mode dynamic crack growth in functionally graded glass-filled epoxy”. In: *Experimental Mechanics* 46.2 (2006), pp. 269–281. ISSN: 00144851. DOI: 10.1007/s11340-006-5863-4.

[71] Madhu Kirugulige and V. Hareesh Tippur. “Mixed-mode dynamic crack growth in a functionally graded particulate composite: Experimental measurements and finite element simulations”. In: *Journal of Applied Mechanics, Transactions ASME* 75.5 (2008), pp. 0511021–05110214. ISSN: 00218936. DOI: 10.1115/1.2932095.

[72] Sandeep Abotula et al. “Dynamic curving cracks in functionally graded materials under thermo-mechanical loading”. In: *International Journal of Solids and Structures* 49.13 (2012), pp. 1637–1655. ISSN: 00207683. DOI: 10.1016/j.ijsolstr.2012.03.010.

[73] Hirshikesh et al. “Phase field modelling of crack propagation in functionally graded materials”. In: *Composites Part B: Engineering* 169.January (2019), pp. 239–248. ISSN: 13598368. DOI: 10.1016/j.compositesb.2019.04.003.

[74] Duc Hong Doan et al. “Hybrid phase field simulation of dynamic crack propagation in functionally graded glass-filled epoxy”. In: *Composites Part B: Engineering* 99 (2016), pp. 266–276. ISSN: 13598368. DOI: 10.1016/j.compositesb.2016.06.016.

[75] Mohammad Naqib Rahimi et al. “An ordinary state-based peridynamic model for toughness enhancement of brittle materials through drilling stop-holes”. In: *International Journal of Mechanical Sciences* 182.May (2020). ISSN: 00207403. DOI: 10.1016/j.ijmecsci.2020.105773.

[76] Xiao Kuang et al. “Grayscale digital light processing 3D printing for highly functionally graded materials”. In: *Science Advances* 5.5 (2019), pp. 1–10. ISSN: 23752548. DOI: 10.1126/sciadv.aav5790.

[77] Zhanqi Cheng et al. “Numerical simulation of crack propagation and branching in functionally graded materials using peridynamic modeling”. In: *Engineering Fracture Mechanics* 191.September 2017 (2018), pp. 13–32. ISSN: 00137944. DOI: 10.1016/j.engfracmech.2018.01.016.